PREDICTING A NEW QUATERNARY PHOTOCATALYST SUITABLE FOR PEC PROCESS TO PRODUCE HYDROGEN AND DETERMNATIONOF ITS STRUCTURAL, ELECTRONICS, AND OPTICAL PROPERTIES USING DENSITY FUNCTIONAL THEORY.

by

PRANAB SARKER

Presented to the Faculty of the Graduate School of
The University of Texas at Arlington in Partial Fulfillment
of the Requirements
for the Degree of

MASTER OF SCIENCE IN PHYSICS

THE UNIVERSITY OF TEXAS AT ARLINGTON

May 2013

Acknowledgements

I would like to express my deepest gratitude to my advisor, Prof. Muhammad N. Huda for his guidance through the course of my study and research. I also would like to extend my thanks to my committee members, Prof. A. K. Ray and Prof. Qiming Zhang for their interests in my research work.

I would also like to appreciate the members of our research groups for being very helpful throughout my research work. Their valuable suggestions during our regular research meetings have enriched my research experience. I am very greatful to Cedric Mayfield for being cooperative throughout of my research work.

In addition, a thank you to Dr. Kapil Adhikary who helped me to organize my writing at the very beginning.

I am very grateful to my parents and sibling for providing me an encouraging environment for my academic career. Special thanks go to my wife Baishakhi Biswas for her continuous support and care.

Finally, I would like to acknowledge the support from the National Renewable Energy Laboratory (NREL) and National Science Foundation (NSF).

April 16, 2013

Abstract

PREDICTING A NEW QUATERNARY PHOTOCATALYST SUITABLE FOR PEC PROCESS TO PRODUCE HYDROGEN AND DETERMNATIONOF ITS STRUCTURAL, ELECTRONICS, AND OPTICAL PROPERTIES USING DENSITY FUNCTIONAL THEORY.

Pranab Sarker, MS

The University of Texas at Arlington, 2013

Supervising Professor: Muhammad N. Huda

Our present work represents a comprehensive theoretical and computational research in quest for predicting new photocatalysts suitable for photoelectrochemical process (PEC) to produce hydrogen by splitting water. We predict a new photocatalyst, $CuBiW_2O_8$ that exhibits some promising photocatalytic features seemed elusive to date. It is well known that all physical properties are calculated once ground state structure is known. However, knowing crystal structure is extremely challenging and was considered unpredictable before the material is synthesized. Our density functional theory (DFT) determines the crystal structure of $CuBiW_2O_8$ to be monoclinic which was later found energetically equivalent to its experimental counterpart. In addition to structure determination, we calculate the electronic and optical properties of $CuBiW_2O_8$ for the first time. Our calculated band gap is 1.43 eV that validates the approach to make band engineering successful by forming suitable complex oxides. The band structure calculation also reveals that $CuBiW_2O_8$ possesses indirect band gap. Moreover, density of states (DOS) calculation demonstrates a successful band gap reduction approach with respect to binary and ternary oxides such as TiO_2, WO_3, BiW_2O_9 etc., where $Cu\ 3d$ orbital plays a major role in band gap reduction. In addition, it explains why electron transition from valence band to conduction band is possible although both band edges are mostly dominated by d orbitals and $d-d$ electron transition is forbidden. Finally, our optical calculation determines this material is optically anisotropic and has a high absorption rate that facilitates hydrogen production through photo-excitations.

Table of Contents

List of Illustrations

List of Tables

Chapter 1

Introduction

The advancements of science and technology which govern the world economy, global climate, human life-style, and which enforce new cultures to be flourished in the society have a far-reaching impact on modern civilization. Needless to say, all cultural, scientific and technological advancements so far have been empowered by fossil fuels - oil, coal, and natural gas - directly or indirectly. It is well known that these fossil fuels, while combustion takes place, emit greenhouse gases in the atmosphere, most notably CO_2, and consequently, have put our habitable earth into a vulnerable position. Hence it has been an imperative task and daunting challenge for scientific community to find out the alternates of fossil fuels which is carbon free and cost effective. Jules Verne, a prophetic visionary and often referred to as the "father of science fiction", was one of the earliest people who conjectured water as a fuel of the future [1]. More than hundred years ago, he imagined to clean hydrogen fuels and wrote in his "The Mysterious Island" book:

"Yes, my friends, I believe that water will someday be employed as fuel, that hydrogen and oxygen, which constitute it, used singly or together, will furnish an inexhaustible source of heat and light….I believe, then, that when the deposits of coal are exhausted, we shall heat and warm ourselves with water. Water will be the coal of the future."

Jules Verne might have visualized hydrogen as clean energy convinced only by the abundance perspective of its source of origin, water. However, water as souce is not only inexhaustible but being splitted also can provide clean and renewable energy. Hydrogen which can be produce by water decomposition emits no CO_2 while burning unlike fossil fuels.

However, the paucity of hydrogen by itself in nature, at least terrestrially, limits it from being an alternate primary source of energy like fossil fuel. Therefore, other substances from which hydrogen can be extracted are needed. Water can be a primary of source of hydrogen production since it is abundant on earth. However, water splitting is not a spontaneous process. Energy is needed to provide externally to drive water splitting reaction, which in turn, must be inexhaustible, renewable, and carbon-free to keep hydrogen not only as clean fuel but also economically viable compared to fossil fuels.

The ultimate goal to produce H_2 with little or no green house gas emissions can be done in several ways [1]- H_2 production from i) fossil fuels with CO_2 sequestration, ii) biomass gasification, iii) electrolysis of water using power generated by renewable energy sources such as wind turbines and solar cells, iv) nuclear power plant, and v) photoelectrochemical (PEC) water splitting using sunlight. The first way is still unproven technology whereas the second and third ways are technically viable but cost-prohibitive. Nuclear plants can generate H_2, which is potentially cost-effective, but have same drawbacks as in any option involving nuclear power e.g. disposal problem, proliferation concerns and lack of public acceptance. The final PEC approach, which is both cost effective and eco-friendly, is yet to be successful because of lacking of a suitable photocatalyst. Therefore, producing H_2 cheaply and at larger scale with little or no green house gas emissions still remains an elusive global.

While other approaches have been abandoned due to either higher cost or environmental safety concerns, PEC has been envisioned as the most pragmatic approach and one of the “holy grail” technologies for hydrogen production [1] [2]. A PEC system produces hydrogen through water decomposition using solar energy harnessed by the single semiconductor-based device immersed in a water-based solution. Since a suitable photocatalyst can convert solar energy to electrochemical energy directly for splitting the water, PEC process gives us clean hydrogen plus oxygen. However, it is not so easy as it sounds good. The success of the PEC process solely depends on a suitable photocatalyst which have the following characteristics: [1] [5] - $i)$ moderate band gap $\left(1.23 \leq E_g \leq 2.2\, eV\right)$ for driving water splitting reaction ($H_2O = H_2 + \frac{1}{2}\, O_2, \Delta\mathrm{E}^\circ = -1.23\ \mathrm{V}$), $ii)$ suitable band edge positions with the water-splitting potentials, $iii)$ higher stability in the aqueous solution, $iv)$ higher optical absorptions efficiency, and $v)$ good charge carrier mobility. The latter three properties come into scenario once the first two criteria are satisfied. All of these characteristics alongside with low production cost, collectively, of a photocatalyst ensure the PEC process to be successful. However, it is well known that such a 'magic' material, in a simple or complex form, neither exists in nature nor has been engineered successfully so far. Binary metal oxides, although treated as better photocatalysts [5] [6] [7] [8] [9] [10] due to higher stability in aqueous solution and low production cost, suffer from both larger band gap ($> 3\ eV$) [11] and suitable band edge positions with the water-splitting potentials [15] hindering the PEC process being efficient. Both transition and post transition metal oxides have lower band gap, however, fail to fulfill the promises of PEC due to either poor carrier mobility or unfavorable indirect band gap [12] [13].

It is possible to easily make 50,000 combinations of ternary oxides and almost 2 million quaternary oxides out of all the materials available in the periodic table. Hence, predicting a new photocatalyst suitable for photoelectrochemical process, experimentally or theoretically, is very extremely challenging and arduous task. The way researchers have been developing new materials out of a large number of oxides throughout the millennia is an empirical approach, can be very time consuming and costly, strenuous, requiring a profound intuition of guessing possible chemical combinations, trials and errors, and a stroke of luck [14]. Hence, it has been an imperative challenge in the scientific community to develop a theoretical approach to make a successful prediction of new complex oxide before it is synthesized. Moderate band gap and suitable band edge positions, which are the two primary concerns in predicting a suitable photocatalyst, could be achieved successfully through bang gap engineering forming mutiternary complex oxides [7] [8] [9] [11] [15] [16]. Few successful multications oxides such as $BiVO_4$, Ag_2WO_4, $Bi_2W_2O_9$, and $AgBiW_2O_8$ [17] [18] [19] [20] [21] show a significant improvement both in band gap reduction and band edge position or in either one with compared to binary oxides. $BiVO_4$ $(2.4\,eV)$ shows a little bit improvement of band gap reduction compared to Bi_2O_3 $(2.5\,eV)$ and high activity on O_2 evolution. However, it cannot evolve H_2 since conduction band contributed by $V.3d$ lies beneath the H_2/H_2O redox potential. On the other hand, both Ag_2WO_4 $(3.1eV)$ and $Bi_2W_2O_9$ $(2.95\,eV)$ have suitable band edge positions with respect to water redox potential compared to WO_3 but solar-to-hydrogen conversion is not observed at the satisfactory level due to larger band gaps. Among all, $AgBiW_2O_8$ exhibits most promising features such as reduced band gap (2.75 eV), suitable band edge position, higher stability in aqueous solution, and low production cost [20] [21]. The addition of two cations- Bi^{3+} and Ag^{+}- to WO_3 reduces its band gap keeping the position of conduction band above the H_2/H_2O redox potential level intact The band gap reduction as in $AgBiW_2O_8$ was not successful by adding only one cation either Bi or Ag to WO_3. $Bi\,p$ in $AgBiW_2O_8$ lowers the conduction band minimum through the coupling between $W\ 5d$ and $O\ 2p$ similar to that of in $Bi_2W_2O_9$ [20] [21] It is noted that $Bi\,p$ plays a similar role in band gap reduction in $BiVO_4$ through the coupling between $V\ d$ and $O\,2p$. [11]. On the other hand, $Ag.4d$ in $AgBiW_2O_8$ uplifts the top of the valence band causing reduction in band gap. Moreover, the upward push by $Ag.4d$ relocates the conduction band above H_2/H_2O redox potential level compared to WO_3 Nevertheless the combined effects of Bi^{3+} and Ag^{+} were not enough to reduce the band gap below $2.2\,eV$.

Hence, we aim to predict a new quaternary metal oxide $CuBiW_2O_8$ bearing all the effects caused by Bi^{3+} and Ag^{+} in mind. In $CuBiW_2O_8$, more intense upward push contributed by $3d$ is expected having the previously mentioned $Bi\,p$ coupling with $W\,d$ and $O\,2p$ at the bottom of the conduction band to reduce the band gap further. To our best knowledge, we, as first, design $CuBiW_2O_8$ theoretically and present comprehensive study of structural, electronic, mechanical, and optical properties using DFT including on-site Coulomb correlation term called U parameter.

The calculation of all physical properties requires successful determination of the ground state crystal structure of the material being predicted. However, prediction of crystal structure was believed fundamentally impossible like predicting earthquake until 2003 albeit the chemical composition or stoichiometry are known [22]. With the advent of high efficient computers and advancement of computational physics, it is possible to predict stable atomic arrangement of a new material, without even being synthesized, quantitatively with minimal time and cost [14] [23] in the context of density functional theory (DFT) *ab initio* calculation.

The goal of this paper is twofold: first is to predict the crystal structure of a multi-cation oxide material (in this case a photocatalyst) with desirable properties by means of mineral database search and density functional theory (DFT) based relaxation. Secondly, the electronic properties of this predicted material will then be elaborated.

Crystal structure prediction with desirable electronic properties

A successful determination of stable structure of a new material requires DFT optimization of all possible motif structures. We define these possible phase structures as 'Motif Structures' of the predicted material. Motif structures are the well-known structures of those synthesized materials from which the unit cell of new compounds is possible to make. It is done by replacing ion(s) in the motif crystal structure by the equal number of chemically similar ion(s) of the material to be predicted. The motif structures are selected through a comprehensive mineral database search considering topological symmetry, chemical and ionic radii proximity of atoms, coordination numbers, and oxidation states of the ions. An example of successful prediction of crystal structure through comprehensive mineral database search method is that of $AgBiW_2O_8$ [21] (see Appendix A), which is the better photocatalyst so far. The crystal structure of $AgBiW_2O_8$ was measured monoclinic ($S.G. I2/m$) experimentally. However, our DFT energy optimization followed by a database search determines different monoclinic symmetry ($S.G. P\,2/c$), and this result was verified with the recent experiment. Apart from crystal structure determination, calculated band gap, suitable band edged positions, and optical absorption rate were in good agreement with the recent experiment as well.

Our DFT+U electronic calculation predicts triclinic symmetry for ground state structure of $CuBiW_2O_8$ that is evolved from $CuWO_4$. This ground state structure possesses an indirect band gap (1.43 eV) sufficient enough to drive water decomposition reaction through PEC process. In our work, we also study WO_3 as the parent structure in W based oxides, and $CuWO_4$ as the possible motif structure for $CuBiW_2O_8$ to observe the systematic transformations taken place while evolved from binary metal oxides to quaternary metal oxide. For optical absorption, it is necessary to consider contributions to the absorption properties from various electronic energy band processes such as intraband, interband. However, we restrict ourselves to the interband processes because intraband processes are less important to semiconductors [24]. All the DFT and DFT+U calculations were performed with respect to a GGA functional [25] [26]. It is very important to describe the band gap and the positions of the band edges as precise as possible for the description of the photocatalytic or photo-electrochemical process [27].

Our GGA calculation gives a better band gap for WO_3 over LDA [28] compared with experimentally determined value. Hence, we prefer GGA over LDA in the present calculations, although overestimation of the equilibrium volume enhancing interatomic separations compared with experimentally measured value is a general feature of GGA [29].

The layout of our work is as follows. In chapter 2, we present a brief description of the methodology-Density Functional Theory (DFT) – with little historical background and its computational scheme. We devote chapter 3 to the structural and electronic study of WO_3. Chapter 4 is includes structural, electronic, and optical studies of $CuWO_4$. The ways all the possible phases of $CuBiW_2O_8$ have been modeled alongside with the calculated structural, electronic, and optical properties are described in chapter 5. We leave the chapter 6 to summarize our findings for WO_3, $CuWO_4$, and $CuBiW_2O_8$. Finally, we propose some ideas and directions to make our future works more reliable and consistent with the experimental counterpart in Chapter 6 as well. Appendix A represents the structural, electronic, and optical properties of $AgBiW_2O_8$. A brief study of structural, electronic, and optical aspects of $ZnWO_4$, a wolframite structure in the ABX_4 family, is presented in Appendix B.

Chapter 2

Methodology

Density Functional Theory

One of the basic problems in theoretical physics and chemistry is the description of the structure and dynamics of many-electron systems. Density functional theory (DFT) is an extremely successful quantum mechanical modeling method used in physics and chemistry to investigate the electronic structure (principally the ground state) of many-body systems, in particular atoms, molecules, and the condensed phases. The main idea of DFT is to describe an interacting system of fermions via its density and not via its many-body wave function. For N electrons in a solid, which obey the Pauli principle and repulse each other via the Coulomb potential, the basic variable of the system depends only on three -- the spatial coordinates x, y, and z -- rather than 3N degrees of freedom. With this theory, the ground state properties of a many-electron system can be determined by using functionals, i.e. functions of another function, which in this case is the spatially dependent electron density, $n[\psi(\vec{r})]$. Hence the name density functional theory comes from the use of functionals of the electron density. DFT is among the most popular and versatile methods available in condensed-matter physics, computational physics, and computational chemistry. Its applicability ranges from atoms, molecules and solids to nuclei and quantum and classical fluids.

Historical Background

Thomas and Fermi [30] [31] were the first [32] to contemplate a model for the electron many-body problem based uniquely on the electron density $n(\vec{r})$. The basic idea of the theory is to find the energy of electrons in a spatially uniform potential as a function of density. Then one uses this function of the density locally even when the electrons are in the presence of an external potential. The Thomas-Fermi energy functional is composed of three terms,

$$E^{TF}[n] = T^{TF}[n] + \int n(\vec{r}) v_{ext}(\vec{r}) d\vec{r} + \frac{1}{2} \iint d\vec{r} d\vec{r}' \frac{e^2 n(\vec{r}) n(\vec{r}')}{|\vec{r} - \vec{r}'|} \tag{2.1}$$

The first term in Equation (2.1) is the electronic kinetic energy associated with a system of non-interacting electrons in a homogeneous electron gas. This form is obtained by integrating the kinetic energy density of a homogeneous electron gas [33] [34] $t_0[n]$,

$$T^{TF}[n] = \int t_0[n(\vec{r})] d\vec{r} \tag{2.2}$$

where $t_0[n(\vec{r})]$ is obtained by summing all of the free-electron energy states $\varepsilon = \frac{\hbar^2 k^2}{2m}$ up to the Fermi wave vector $k_F = [3\pi^2 n(\vec{r})]^{1/3}$. Finally,

$$T^{TF}[n] = \int \frac{\hbar^2}{2m} \frac{3}{5} (3\pi^2)^{2/3} \, n(\vec{r})^{5/3} (\vec{r}) \tag{2.3}$$

The second term is the classical electrostatic energy of attraction between the nuclei and the electrons, where $v_{ext}(\vec{r})$ is the static Coulomb potential arising from the nuclei,

$$v_{ext}(\vec{r}) = -\sum_{j=1}^{N} \frac{e^2 Z_j}{|\vec{r} - \vec{R}_j|} \tag{2.4}$$

Finally, the third term represents the electron-electron interactions of the system approximated by the classical Coulomb repulsion between electrons, known as the Hartree energy.

To obtain the ground state density and energy of a system, the Thomas-Fermi energy functional must be minimized subject to the constraint that the number of electrons is conserved. This type of constrained minimization problem, which occurs frequently within many-body methods, can be performed using the technique of Lagrange multipliers. In general terms, the minimization of a functional $F[f]$, subject to the constraint $C[f]$, leads to the following stationary condition,

$$\delta\,(F[f] - \mu C[f]) = 0 \tag{2.5}$$

Where μ is a constant known as the Lagrange multiplier. Minimizing the above equation leads to the solution of the corresponding Euler equation,

$$\delta F[f]/\delta f - \mu\, \delta C[f]/\delta f = 0 \tag{2.6}$$

When Thomas-Fermi energy functional incorporates the exchange term of the following form,

$$\varepsilon_{xc} = -\int \frac{3}{4}\left(\frac{3}{\pi}\right)^{1/3} e^2\, n(\vec{r})^{4/3}(\vec{r}) \tag{2.7}$$

the theory is called Thomas-Fermi-Dirac [35].

Foundation of Density Functional Theory

Due to the severe shortcomings of Thomas-Fermi method [35] such as inability to predict molecular binding, failure to demonstrate the electrons' distribution into different shells, better accuracy only for nearly uniform charge distribution etc., it was hard to be imagined that an exact theory could be based on the density. However, almost forty years later, Hohenberg and Kohn proved in a seminal paper [36] that this was indeed possible. In two remarkably powerful theorems they formally established the electron density as the central quantity describing electron interactions contained in a many-electron wave function, and so devised the formally exact ground state method known as density functional theory (DFT). Hence, the starting point of any discussion of DFT is the Hohenberg-Kohn (HK) theorems.

Hohenberg-Kohn (HK) theorems

The Hohenberg-Kohn theorems relate to any system consisting of electrons moving under the influence of an external potential $v_{ext}(\boldsymbol{r})$. Stated simply they are as follows:

Theorem 1: *The external potential* $v_{ext}(\boldsymbol{r})$ *, and hence the total energy, is a unique functional of the electron density. In other words, the electron density determines the external potential (to within an additive constant) uniquely.*

Proof:

In the original Hohenberg-Kohn paper, this theorem is proven for densities with non-degenerate ground states [8]. This extension of this proof to degenerate ground states is also valid. The proof in both cases is elementary, and by contradiction. Let us first consider non-degenerate case.

Non-degenerate Ground States

Let us define the set of all external potentials $v_{ext}(\boldsymbol{r})$, $\mathbb{V}$ such that

$$\mathbb{V} = \left\{ v_{ext}(\boldsymbol{r}) \middle| \begin{matrix} with{:}\ v_{ext}(\boldsymbol{r})\ multiplicative\,, \\ corresponding\ \mid \Psi_0 > exists\ and \\ is\ non-degenerate, v'_{ext}(\boldsymbol{r}) \neq v_{ext}(\boldsymbol{r}) + const. \end{matrix} \right\} \tag{2.8}$$

for which Schrödinger equation

$$\hat{H} \mid \Psi_k > \; = E_k \mid \Psi_k > \tag{2.9}$$

leads to a non-degenerate eigenstate $\mid \Psi_0 >$.

The set of all external potentials $v_{ext}(\boldsymbol{r})$, $\mathbb{V}$ leads to a set non-degenerate ground eigenstates $\mid \Psi_0 >$, $\mathcal{G}$ such that

$$\mathcal{G} = \left\{ \mid \Psi_0 > \middle| \begin{matrix} with{:}\ \mid \Psi_0 > ground\ state\ corresponding\ to \\ one\ element\ of\ \mathbb{V}\,, \\ \mid \Psi'_0 > \neq e^{i\varphi} \mid \Psi_0 > \\ with\ \varphi\ being\ some\ global\ phase \end{matrix} \right\} \tag{2.10}$$

And the set $\mathcal{N}$ of all ground state densities obtained from some element of $\mathcal{G}$ is defined as

$$\mathcal{N} = \{ \mathrm{n}_0 \mid \mathrm{n}_0(\boldsymbol{r}) =< \Psi_0 \mid \hat{n}(\boldsymbol{r}) \mid \Psi_0 >, \ \mid \Psi_0 > \in G \} \qquad (2.11)$$

Where, $\mathrm{n}_0(\boldsymbol{r}) =< \Psi_0 \mid \hat{n}(\boldsymbol{r}) \mid \Psi_0 >$

$$= N \sum_{\sigma_{1,\dots\dots,}\sigma_N} \int d^3 r_1 \dots\dots d^3 r_N \ \mid (\boldsymbol{r_1 \sigma_1}, \boldsymbol{r_2 \sigma_2}, \dots\dots, \boldsymbol{r_N \sigma_N} \mid \Psi_0 >\mid^2$$

Correspondence between the elements of $\mathbb{V}$, $\mathcal{G}$ and $\mathcal{N}$ can be thought as the following two maps (shown in Figure 2.1)

A: $\mathbb{V} \rightarrow \boldsymbol{\mathcal{G}}$

and **B:** $\boldsymbol{\mathcal{G}} \rightarrow \boldsymbol{\mathcal{N}}$

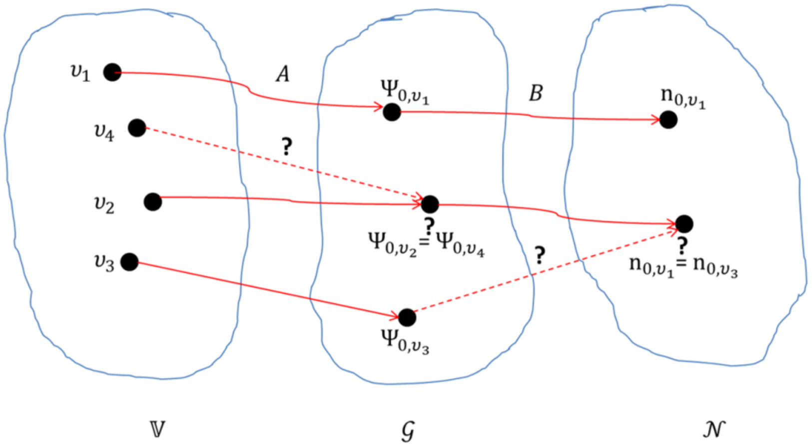

Figure 2.1. Correspondence between external potentials v_i, associated ground states Ψ_{0,v_i} and ground state densities n_{0,v_i}, in the case of non-degenerate ground states [37].

It is sufficient to show that map **A** and map **B** are unique in order to proof first Hohenberg-Kohn theorem in the non-degenerate case.

The proof of uniqueness for map **A** consists in demonstrating the validity of the following two statements:

(i) For given $v_{ext}(\boldsymbol{r})$ there exists only one $| \Psi_0 >$in $\boldsymbol{\mathcal{G}}$, i.e. there is no $v_{ext}(\boldsymbol{r})$ which is mapped onto two elements of $\boldsymbol{\mathcal{G}}$. This statement is trivial due to the restriction to non-degenerate ground states.

(ii) There is no $| \Psi_0 >$ which is simultaneously ground state for two different potentials $v_{ext}(r)$ and $v'_{ext}(r)$ which differ by more than a constant. The standard proof of this statement is based on *a reductio ad absurdum* [37].

Let us assume that $| \Psi_0 >$ is simultaneously ground state for two different potential $v_{ext}(\boldsymbol{r})$ and $v'_{ext}(\boldsymbol{r}) \neq v_{ext}(\boldsymbol{r}) + const$ thus satisfies two Schrödinger equations,

$$\hat{H} \,|\, \Psi_0 >= \left[\hat{T} + \hat{V}_{ext} + \hat{W}\right] |\, \Psi_0 > \; = E_0 \,|\, \Psi_0 > \qquad (2.12)$$

$$\hat{H}' \,|\, \Psi_0 >= \left[\hat{T} + \hat{V}'_{ext} + \hat{W}\right] |\, \Psi_0 > \; = E_0' \,|\, \Psi_0 > \qquad (2.13)$$

$\hat{T}$= kinetic energy operator

$$\hat{T} = \sum_{i=1}^{N} \frac{(-i\hbar\nabla_i)^2}{2m} \qquad (2.14)$$

$\widehat{V_{ext}}$ is the operator that accounts the interaction of the particles with external sources characterized by a given, time independent potential $v_{ext}(\boldsymbol{r})$

$$\widehat{V_{ext}} = \sum_{i=1}^{N} v_{ext}(\boldsymbol{r_i}) = \int d^3r v_{ext}(\boldsymbol{r_i}) \widehat{n}(\boldsymbol{r}) \qquad (2.15)$$

In practical applications $v_{ext}(\boldsymbol{r})$ is given by

$$\hat{V}_{n-e} = -\sum_{\alpha=1}^{k} \sum_{i=1}^{N} \frac{Z_\alpha e^2}{|\boldsymbol{R}_\alpha - \boldsymbol{r}_i|} \qquad (2.16)$$

Where $\boldsymbol{R}_\alpha$ denotes the Cartesian coordinates of nucleus α and $\boldsymbol{r}_i$ denotes the position of electron i

$\hat{W}$= a particle-particle interaction operator

$$=\sum_{i,j=1}^{n} w(\boldsymbol{r_i},\boldsymbol{r_j}) = \frac{1}{2}\sum_{i,j=1;i\neq j}^{n} w(\boldsymbol{r_i},\boldsymbol{r_j}) \qquad (2.17)$$

The basic DFT formalism is independent of the form of w keeping it same throughout discussion.

The subtraction of Equation (2.12) and Equation (2.13) yields

$$[\hat{V}_{ext} - \hat{V'}_{ext}] \mid \Psi_0 > \; = [E_0 - E_0'] \mid \Psi_0 > \qquad (2.18)$$

The wavefunction $\Psi_0(\boldsymbol{r_1\sigma_1}, \ldots\ldots, \boldsymbol{r_N\sigma_N})$ does not vanish for all points $\boldsymbol{r_i}$. Thus, one obtains

$$\sum_{i=1}^{N}[v_{ext}(\boldsymbol{r_i}) - v'_{ext}(\boldsymbol{r_i})] = E_0 - E_0' \qquad (2.19)$$

Keeping N −1 of the $\boldsymbol{r_i}$ fixed, and letting the remaining position vary, Eq. (2.15) leads to a contradiction (as the right-hand side is constant, while $v_{ext}(\boldsymbol{r})$ and $v'_{ext}(\boldsymbol{r})$ are assumed to differ by more than a constant). Consequently, the map **A** is unique: there is a one-to-one correspondence between the potential $v_{ext}(\boldsymbol{r})$ and the resulting ground state$\mid \Psi_0 >$ (up to some additive constant in $v_{ext}(\boldsymbol{r})$).

In order to demonstrate the uniqueness of **B**, one has to show that two different $\mid \Psi_0 > \in G$ cannot lead to the same ground state density n_0. The proof again relies on *reductio ad absurdum*.

Assume that n_0 is obtained from two different elements $\mid \Psi_0 >$ and $\mid \Psi'_0 >$ of . From the Ritz variational principle one then obtains an inequality for the ground state energy,

$$E_0 =< \Psi_0 \mid \hat{H} \mid \Psi_0 > \; < \; < \Psi'_0 \mid \hat{H} \mid \Psi'_0 > \qquad (2.20)$$

$$E_0 < \; < \Psi'_0 \mid \hat{H} \mid \Psi'_0 > \qquad (2.21)$$

Where $\widehat{H}$ is the unique Hamiltonian leading to $|\Psi_0>$ (due to the uniqueness of map A) and the strict inequality originates from the non-degeneracy $|\Psi_0>$ and $|\Psi'_0>$. After manipulation

$$E_0 < \ <\Psi'_0 | \widehat{H}' | \Psi'_0> + <\Psi'_0 | \widehat{H} - \widehat{H}' | \Psi'_0> \tag{2.22}$$

Or,
$$E_0 < \ E'_0 + <\Psi'_0 | \left(\hat{T} + \hat{V}_{ext}\right) - \left(\hat{T} + \hat{V}'_{ext}\right) | \Psi'_0> \tag{2.23}$$

Or,
$$E_0 < \ E'_0 + <\Psi'_0 | \ \widehat{V}_{ext} - \hat{V}'_{ext} | \Psi'_0> \tag{2.24}$$

Or,
$$E_0 < \ E'_0 + <\Psi'_0 | \ \widehat{V}_{ext} - \hat{V}'_{ext} | \Psi'_0> \tag{2.25}$$

Or,
$$E_0 < \ E'_0 + <\Psi'_0 | \ \int d^3r v_{ext}(r_i) \widehat{n}(r) - \int d^3r \, v'_{ext}(r_i) \, \hat{n}'(r) | \Psi'_0> \tag{2.26}$$

Or,
$$E_0 < E'_0 + \int d^3r \, [v_{ext}(r_i) <\Psi'_0 | \ \hat{n}(r) \ | \Psi'_0> - v'_{ext}(r_i) <\Psi'_0 | \ \hat{n}'(r) | \Psi'_0>] \tag{2.27}$$

Using the multiplicative form of $\widehat{V}_{ext}$ Equation (2.15) and the assumption that both states lead to the same density n_0, one obtains

Or,
$$E_0 < \ E'_0 + \int d^3r \, [v_{ext}(r_i)\mathrm{n}_0(r) - v'_{ext}(r_i)\mathrm{n}_0(r)] \tag{2.28}$$

Or,
$$E_0 < \ E'_0 + \int d^3r \, \mathrm{n}_0(r)[v_{ext}(r_i) - v'_{ext}(r_i)] \tag{2.29}$$

Interchanging primed and unprimed quantities,

$$E'_0 < \ E_0 + \int d^3r \, \mathrm{n}_0(r)[v'_{ext}(r_i) - v_{ext}(r_i)] \tag{2.30}$$

Upon addition of Eqs. (2.29) and (2.30), one ends up with a contradiction,

$$E_0 + E_0' < \quad E_0' + E_0 \tag{2.31}$$

One therefore concludes that the map B is also unique: there is a one-to-one correspondence between $\mid \Psi_0 >$ and n_0.

Hence, v_{ext}, $\mid \Psi_0 >$ and n_0 determine each other uniquely.

$$v_{ext}(\boldsymbol{r}) \Leftrightarrow \underset{\uparrow}{\mid \Psi_0 >} \underset{\uparrow}{\Leftrightarrow} \mathrm{n}_0(\boldsymbol{r}) = \ < \Psi_0 \mid \hat{n}(\boldsymbol{r}) \mid \Psi_0 > \tag{2.32}$$

unique (up to some constant in v_{ext})

*Theorem 2***:** *The density that minimizes the total energy functional is the exact ground state density. If one find the functional* $E[n]$*, then the true ground state density* $n(\boldsymbol{r})$ *minimizes it being subjected only to the constraint that*

$$\int d^3r\, n(\boldsymbol{r}) = N$$

For any positive definite trial density,

$n_0'(r) \neq n_0(r)$ such that $\int d^3r\, n'(\boldsymbol{r}) = N$

$$E[n_0] < E[n_0'] \ \Leftrightarrow \ E_0 = \min_{n \in \mathcal{N}} E[n]$$

i.e., the ground state energy can be obtained variationally.

Proof:

Let Ψ_0 be the wavefunction associated with the correct ground state. The variational principle asserts,

$$< \Psi_0[n(\boldsymbol{r})] \mid \hat{T} + \widehat{W} + \widehat{V}_{ext} \mid < \Psi_0[n(\boldsymbol{r})] \ < \tag{2.33}$$

$$< \Psi'_0[n'(\boldsymbol{r})] \mid \hat{T} + \widehat{W} + \widehat{V}_{ext} \mid \Psi'_0[n'(\boldsymbol{r})] >$$

Define the functional

$$F[n] \coloneqq \ < \Psi[n] \mid \hat{T} + \widehat{W} \mid \Psi[n] > \tag{2.34}$$

The energy functional $E[n(\boldsymbol{r})]$ alluded to in the first Hohenberg-Kohn theorem can be written in terms of the external potential $v_{ext}(\boldsymbol{r})$ in the following way,

$$E[n(\boldsymbol{r})] = F[n] + \int d^3r\, v_{ext}(\boldsymbol{r})n(\boldsymbol{r}) \tag{2.35}$$

These lead to

$$F[n_0(\boldsymbol{r})] + \int d^3r\, v_{ext}(\boldsymbol{r})n_0(\boldsymbol{r}) < F[n_0'(\boldsymbol{r})] + \int d^3r\, v_{ext}(\boldsymbol{r})n_0'(\boldsymbol{r}) \tag{2.36}$$

$$E[n_0(\boldsymbol{r})] < E[n_0'(\boldsymbol{r})] \tag{2.37}$$

Where,

$$E[n_0(\boldsymbol{r})] = \min_{\mathrm{n}} E[n(\boldsymbol{r})] \tag{2.38}$$

Hence, the variational principle of the second Hohenberg-Kohn theorem is obtained.

The most intriguing feature of this proof is that the functional $F[n]$ is universal for all system of N particles and does not depend upon the external potential $v_{ext}(\boldsymbol{r})$ i.e., if one could minmizes this functional with respect to ground state density, it would solve all many-body problems for all external potentials $v_{ext}(\boldsymbol{r})$. The possibility to determine the ground state density of a many-particle system is given by a variational equation

$$\frac{\delta}{\delta n}\left\{E[n] - \mu\left(\int d^3r\, n(\boldsymbol{r}) - N\right)\right\} |_{n(r)=n_0(r)} = 0 \tag{2.39}$$

$$\frac{\delta}{\delta n}\left\{F[n] + \int d^3r v_{ext}(\boldsymbol{r})n(\boldsymbol{r}) - \mu\left(\int d^3r\, n(\boldsymbol{r}) - N\right)\right\} |_{n(r)=n_0(r)} = 0 \tag{2.40}$$

$$\frac{\delta F[n]}{\delta n} |_{n(r)=n_0(r)} + v_{ext}(\boldsymbol{r}) = \mu \tag{2.41}$$

Where, $F[n] := \; < \Psi[n] \mid \hat{T} + \hat{W} \mid \Psi[n] > \; = Universal\, part$

We can identify the constant μ as the chemical potential of the system, since $\mu = \frac{\delta E[n]}{\delta n}$. One adds to it any particular set of nuclei, in the form of the external potential $v_{ext}(\boldsymbol{r})$, and then has only to find the function $n(\boldsymbol{r})$ that minimizes it in order to solve the full complexities of Schrodinger's equation. The exact density is such that it makes the functional derivative of F exactly equal to the negative of the external potential (up to a constant). If we had an adequate approximation to $F[n]$ for our purposes, it would be possible to solve the equation for $E[n]$ directly. Unfortuntely, no adequate approximation is available for $F[n]$

Computational Techniques

For many body system the Hohenberg-Kohn theorems states that knowledge of the ground state density is sufficient to determine all ground state observables. In addition, the ground state energy functional $E[n]$ allows the determination of the ground state density itself via the variational equation discussed in the previous section. Although the Hohenberg-Kohn theorems are extremely powerful, do not give any hint concerning the explicit form of $E[n]$ (or $F[n]$) and therefore, do not offer a way of computing the ground-state density of a system in practice. About one year after the seminal DFT paper Hohenberg and Kohn devised a simple method for carrying-out DFT calculations that retains the exact nature of DFT and replaces the many-body problem by an exactly equivalent set of self-consistent one-electron equations. This method is described next.

The Kohn-Sham (KS) Energy Functional

Unfortunately, the Hohenberg-Kohn theorem provides no guidance as to the form of $E[n]$, and therefore the utility of DFT depends on the discovery of sufficiently accurate approximations. In order to do this, the unknown functional, $E[n]$, is rewritten as the Hartree total energy plus another, but presumably smaller, unknown functional, called the exchange-correlation (XC) functional, $E_{XC}[n]$. The Kohn-Sham (KS) total-energy functional for a set of doubly occupied electronic states ψ_i can be written as

$$E[n(\boldsymbol{r})] = T_s[n] + E_{ei}[n] + E_H[n] + E_{ii}[n] + E_{XC}[n] \tag{2.42}$$

Here $T_s[n]$ denotes the single particle kinetic energy, $E_{ei}[n]$ is the Coulomb interaction energy between electrons and nuclei, $E_{ii}[n]$ arises from the interaction of the nuclei with each other, and $E_H[n]$ is Hartee component of the electron-electron energy with density ,

$$E_H[n] = \frac{e^2}{2}\int \frac{n(\boldsymbol{r})n(\boldsymbol{r}')}{|\boldsymbol{r}-\boldsymbol{r}'|}\, d^3\boldsymbol{r}\, d^3\boldsymbol{r}' \tag{2.43}$$

including self-interaction energy of the electrons. Where $n(\boldsymbol{r})$ is the electron density given by

$$n(\boldsymbol{r}) = 2\sum_i |\psi_i(\boldsymbol{r})|^2 \tag{2.44}$$

As mentioned, $E_{XC}[n]$ is an unknown functional.

Only the minimum value of Kohn-Sham (KS) energy functional has physical meaning. At the minimum, Kohn-Sham (KS) energy functional is equal to the ground-state energy of the system of electrons with the ions in positions $\{\mathbf{R}_I\}$.

Kohn-Sham (KS) Equations

It is necessary to determine the set of wave functions ψ_i that minimize the Kohn-Sham (KS) energy functional. These are given [10] by self-consistent solutions to the

Kohn-Sham (KS) equations [38] which represent a mapping of the interacting many-electron system onto a system of non-interacting moving in an effective potential due to all other electrons. Kohn-Sham system is simply a fictitious system of non-interacting electrons, chosen to have the same density as the physical system. Then its wave functions are given by

$$\left[\frac{\hbar^2}{2m}\nabla^2 + V_{eff}\right]\psi_i(\boldsymbol{r}) = \varepsilon_i\psi_i \tag{2.45}$$

This is a single-electron equations where ψ_i is the wave function of electronic state i, ε_i is the Kohn-Sham eigenvalue, and V_{eff} is the effective potential due to $N-1$ electrons in the Kohn-Sham system,

$$V_{eff} = V_{ion}(\boldsymbol{r}) + V_H(\boldsymbol{r}) + V_{XC}(\boldsymbol{r}) \tag{2.46}$$

The celebrated Kohn-Sham (KS) equations resulting from insertion of

$$\left[\frac{\hbar^2}{2m}\nabla^2 + V_{ion}(\boldsymbol{r}) + V_H(\boldsymbol{r}) + V_{XC}(\boldsymbol{r})\right]\psi_i(\boldsymbol{r}) = \varepsilon_i\psi_i \tag{2.47}$$

$$H_{KS}\psi_i(\boldsymbol{r}) = \varepsilon_i\psi_i \tag{2.48}$$

have to be solved in a s elf-consistent fashion. Where H_{KS} is the Hamiltonian for a Kohn-Sham system,

$$H_{KS} = \frac{\hbar^2}{2m}\nabla^2 + V_{ion}(\boldsymbol{r}) + V_H(\boldsymbol{r}) + V_{XC}(\boldsymbol{r}) \tag{2.49}$$

Here, $V_{ion}(\boldsymbol{r})$ is the total electron-ion potential, $V_H(\boldsymbol{r})$ is the Hartee potential of electrons given by

$$V_H(\boldsymbol{r}) = e^2\int\frac{n(\boldsymbol{r}')}{|\boldsymbol{r}-\boldsymbol{r}'|}\ d^3\boldsymbol{r}' \tag{2.50}$$

and the exchange-correlation potential, $V_{XC}(\boldsymbol{r})$, is given formally by the functional derivative

$$V_{XC}(\boldsymbol{r}) = \frac{\delta E_{XC}(\boldsymbol{r})}{\delta n(\boldsymbol{r})} \tag{2.51}$$

The Kohn-Sham (KS) equations must be solved self-consistently i.e., a density must be found such that it yields an effective potential that when inserted into the Schrodinger-like equations yields wavefunctions that reproduce it . A flow chart that depicts the self-consistent solutions of KS equations is shown in Figure 2.2. Thus, instead of having to solve a many-body Schrodinger equation, using DFT we have the far easier problem of determining the solution to a series of single particle equations, along with a self-consistency requirement . The sum of the single-particle Kohn-Sham eigenvalues does not give the total electronic energy because this overcounts the effect of electron-electron interaction in the Hartee energy and in the exchange-correlation energy.

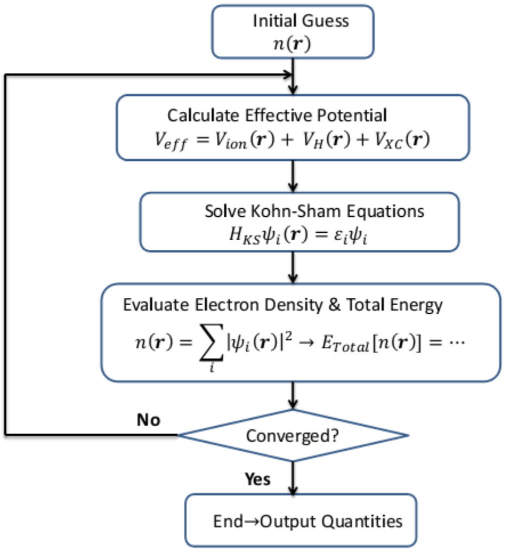

Figure 2.2 Flow-chart depicting a generic Kohn-Sham calculation.

The Exchange Correlation Energy-LDA and GGA

If the exchange-correlation energy functional were known exactly, taking the functional derivative with respect to the density would produce an exchange-correlation potential that included the effects of exchange and correlation exactly. No analytical form has yet been identified and therefore, an approximation must be used. The Hohenberg-Khon theorem provides some motivation for using approximate methods to describe the exchange-correlation energy as a function of electron density. The simplest method of describing the exchange-correlation energy of an electronic system is to use the local-density approximation [28].

Local Density Approximation (LDA)

In the local-density approximation the exchange-correlation energy of an electronic system is constructed by assuming that the exchange-correlation energy per electron at a point $\boldsymbol{r}$ in the electron gas, $\varepsilon_{XC}(\boldsymbol{r})$, is equal to the exchange-correlation energy per electron in a homogeneous electron gas that has the same density as the electron gas at point $\boldsymbol{r}$. In the LDA, $E_{XC}(\boldsymbol{r})$ is written as

$$E_{XC}[n(\boldsymbol{r})] = \int \varepsilon_{XC}(n(\boldsymbol{r}))\, n(\boldsymbol{r}) d^3\boldsymbol{r} \tag{2.52}$$

and

$$\frac{\delta E_{XC}(\boldsymbol{r})}{\delta n(\boldsymbol{r})} = \frac{\partial[\varepsilon_{XC}(n(\boldsymbol{r}))n(\boldsymbol{r})]}{\partial n(\boldsymbol{r})} \tag{2.53}$$

with $\varepsilon_{XC}(\boldsymbol{r}) = \varepsilon_{XC}^{hom}[n(\boldsymbol{r})]$.

where $\varepsilon_{XC}^{hom}[n(\boldsymbol{r})]$ is approximated by a local function of the density, usually that which reproduces the known energy of the uniform electron gas. The local-density approximation assumes that the exchange-correlation energy functional is purely local and, in principle, ignores corrections to the exchange-correlation energy at a point $\boldsymbol{r}$ due to nearby inhomogeneities in the electron density.

A straightforward generalization of the LDA to include electron spin is local spin-density approximation (LSDA)

$$E_{XC}[n_{\uparrow}, n_{\downarrow}] = \int \varepsilon_{XC}(n_{\uparrow}, n_{\downarrow})\, n(\boldsymbol{r}) d^3\boldsymbol{r} \tag{2.54}$$

Generalized Gradient Approximation (GGA)

Generalized gradient approximations (GGAs), where the local gradient as well as the density is used in order to incorporate more information about the electron gas in question, favor density inhomogeneity more than LSDA does. In GGA, $\varepsilon_{XC}(n(\boldsymbol{r}))$ is replaced by $\varepsilon_{XC}(n(\boldsymbol{r}), |\nabla n(\boldsymbol{r})|)$ to take the account of inhomogeneity for a slowly varying density. Generalized gradient approximations (GGA) [25] [26] has the following form:\

$$E_{XC}[n_{\uparrow}, n_{\downarrow}] = \int \varepsilon_{XC}(n_{\uparrow}, n_{\downarrow}, \nabla n_{\uparrow}, \nabla \boldsymbol{n}_{\downarrow})\, n(\boldsymbol{r}) d^3\boldsymbol{r} \tag{2.55}$$

In comparison with LDA and LSDA, GGAs have many advantages [25] [39] [40] [41] [42] [43] [44] [45]. For example, GGAs significantly improve the ground state properties of light atoms and molecules, clusters and solids composed of them. Unlike the LSDA the correct bcc ground state of Fe is obtained through GGAs. Structural properties are generally improved, although GGAs sometimes lead to overcorrection of the LDA errors in lattice parameters.

DFT+U

In solid, both d – and f -states have tendency to retain their atomic character while the valence s - and p-states tend to form bands. Both LDA and GGA descriptions for s - and p-states are well agreement with the experimental observations. However, it has been a common practice that both LDA and GGA can not predict the behavior of highly localized and atomic-like d – and f – states accurately in many compounds especially which contain rare-earth or late transition metal elements [37]. For many transition metal oxides, where a sizeable band gap is observed experimentally, both LDA and GGA predict metallic ground states and itinerant d –states or underestimate the band gap significantly. These descrepencies are inherited in the calculation primarily due to the lack of proper treatment of the self-interaction correction (SIC) of the electrons [47]. The improper treatments of band gap and d or f –states can be improved by a decomposition of the complete Hilbert space into two subsystems, following the Anderson model [46]: (i) the localized d -or f -states for which a more explicit, orbital-dependent treatment of all Coulomb effects is required, and (ii) the s - and p-states which are well described by the LDA (or GGA). The technical implementation of this concept in DFT is the LDA (or GGA)+ U method where U is known as Hubbard parameter [47] [48] [49] [50] . For its derivation the only assumption required is that the d -or f -states are localized within well-separated atomic spheres, so that the bulk states are well represented by a superposition of the corresponding atomic states only. The Hubbard parameter U is defined as [51]

$$U = E(d^{n+1}) + E(d^{n-1}) - 2E(d^{n}) \tag{2.56}$$

i.e., the Coulomb energy cost to place the two electrons at the same site. In all model Hamiltonians the U parameter is treated as a constant which only depends on the type of atom and its environment in the crystal through the screening (or renormalization) effects but not on the configuration of the localized electrons. The new functional [48] is [51] [52]:

$$E^{DFT+U} = E^{DFT}\,[n(\boldsymbol{r})] + E^{U}[\{n_{m}^{I\sigma}\}] - E^{dc}[\{n^{I\sigma}\}] \tag{2.57}$$

where $n_{m}^{I\sigma}$ are the atomic-orbital occupations for the atom I experiencing the “Hubbard correction” term, $E^{DFT}\,[n]$ is a standard approximate DFT functional, $E^{U}[n_{m}^{I\sigma}]$ is Hubbard correction term, and the last term in the above equation $E^{dc}[\{n^{I\sigma}\}]$ is called the “double counting” term subtracted explicitly to avoid the double counting of energy contribution of these orbitals included in $E^{U}[\{n_{m}^{I\sigma}\}]$ and, in some average way, in $E^{DFT}[n(\boldsymbol{r})]$ (LDA or GGA functionals). The DFT + U functional introduced in the above eqution contains only a minimal set of on-site interaction parameters that takes account the effect only associated to on-site Coulomb repulsion and therefore, neglect the proper treatment of magnetic (exchange) interaction. These effects can be compensated, or alternatively can be mimicked redefining the U parameter as $U^{eff} = U - J$ [53] where J denotes the Stoner exchange parameter. Taking both on-site Coulomb and proper magnetic (exchange) interactions into the consideration the total energy functional of DFT+ U can be written as [54]

$$E^{DFT+U} = E^{DFT}[n(\boldsymbol{r})] + E^{U}\left[\{n_{mm'}^{I\sigma}\}\right] \tag{2.58}$$

Where $E^{U}\left[\{n_{mm'}^{I\sigma}\}\right]$ is the simplified form of the Hubbard correction to the energy functional [27] [54]

$$\begin{aligned} E^{U}\left[\{n_{mm'}^{I\sigma}\}\right] &= E^{U}\left[\{n_{mm'}^{I}\}\right] - E^{dc}[\{n^{I\sigma}\}] \\ &= \frac{U^{I}}{2}\sum_{I,\sigma}\sum_{i}\lambda_{i}^{I\sigma}(1-\lambda_{i}^{I\sigma}) \\ &\qquad with\, 0 \le \lambda_{i}^{I\sigma} \le 1 \end{aligned} \tag{2.59}$$

In the above equation, U^{I} is the Coulomb repulsion parameter on atomic site I. This is how the new functional $E^{U}\left[\{n_{mm'}^{I\sigma}\}\right]$ compensates the known deficiencies of LDA or GGA for atomic systems. However, the price is paid appeared obvious in the above equation that $E^{U}\left[\{n_{mm'}^{I\sigma}\}\right]$ favors only partial occupation of the localized orbitals and vanishes for fully occupied ($\lambda \approx 1$) or completely empty ($\lambda \approx 0$) orbitals. This is the basic physical effect built in the DFT + U functional.

Projector Augmented Wave (PAW) Method

In order to solve the electronic structure problem within the DFT formalism, the Kohn-Sham equations are to be solved in some efficient numerical way. The key problem is to expand electron orbitals used to express the single particle density in K-S equation in terms of any converged basis set that accounts different behavior of wave functions of real materials in different regions of space. Atomic wave functions of real materials, which are the eigenstates of the atomic Hamiltonian and are all mutually orthogonal to each other, are fairly smooth in the bonding region, however, oscillates rapidly close to the nucleus owing to the large attractive potential of the nucleus. In order to maintain the orthogonal property of atomic wave functions, which is required by the exclusion principle, the valence wave functions oscillate rapidly in the core region since the core wave functions are well localized around the nucleus. This arises difficulty in solving K-S equations within the DFT formalism numerically to describe the bonding region to a high degree of accuracy while accounting for the large variations in the atom center requiring a very large basis set, or a very fine mesh. Numerous methods have been developed to solve the resulting single particle K-S equation treating core and valence electrons in a different way, possibly obtaining numerical advantages.

One common approach is to use frozen-core approximation that treats core states are invariant in the different chemical environments. Pseudopotential, which exploits frozen-core approximation, replaces the strong ionic potential experienced by core electrons with an effective, smooth and weaker potential. This pseudopotential acts on a set of pseudo wave functions rather true valence wave functions in such a way to reproduce the true effect on the valence electrons outside the core region. This approximation allows one to solve Kohn-Sham equations only for the valence electrons reducing computational cost, however, makes harder to calculate properties that rely on the core region e.g., electric field gradients, hyperfine parameters, etc. Another major drawback is that the procedure to generate good pseudopotentials is not well controlled.

Another approach is the so called class of “all-electron” methods (AE), in which the strong ionic potential in core region is no longer replaced with an effective, smooth and weaker potential. Hence, full information about real wave functions in the core region is available compared to pseudopotential approach. One of the most important of such methods is the Augmented-Plane-Wave method (APW) [55] [56], in which the space is partitioned in two regions: a spherical one around each atom in which the wavefunction is expanded onto a local basis in order to reproduce the great variations, and an interstitial region in which another basis is chosen (plane waves for instance) and connected to the first local basis. A modification of APW which provides a flexible and accurate band structure method is known as Liner-APW (LAPW) [37].

The projector augmented wave method (PAW) [57] is a technique used in ab initio electronic structure calculations. It is a generalization of the pseudopotential and linear augmented-plane-wave methods, and allows for density functional theory calculations to be performed with greater computational efficiency. It is an all electrons (AE) method for ab-initio molecular dynamics that provides the full wave functions that are not directly accessible with the pseudopotential approach, and the potential is determined properly from the full charge densities. PAW avoids transferability problems of pseudopotentials and provides theoretical basis for pseudopotentials. Like APW (or LAPW), PAW method transforms the rapidly oscillating wavefunctions in the core region into smooth wavefunctions which are more computationally convenient.

The historical context of electronic structure method is shown in Figure 2.3 (Augmented-plane-wave (APW) method [55] [56], Korringa-Kohn-Rostocker method (KKR) [58] [59] norm-conserving pseudopotential [60], LMTO [61] [62] LAPW [63]).

scattered Waves (KKR, APW)	**empirical pseudopotentials**
energy independent basisfunctions (LMTO,LAPW)	**ab-initio pseudopotentials**
energy- and potential independent augmented waves (PAW)	

Figure 2.3 Historical context of electronic structure method [57].

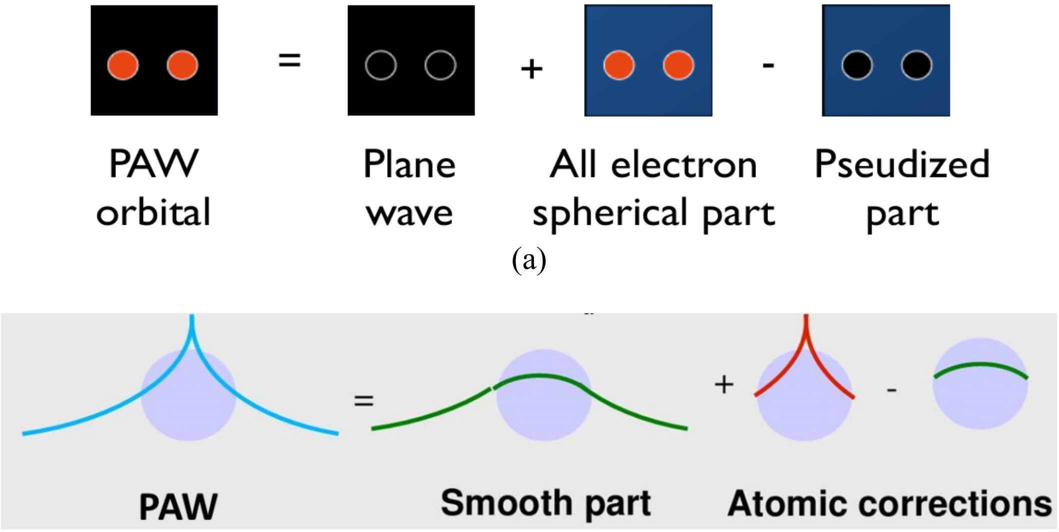

(a)

(b)

Figure 2.4 Schematic representation of Projector Augmented Wave (PAW) method.

Formalism

The trick in PAW method is to divide the wave functions into two parts: i) a partial-wave expansion within an atom-centered sphere and ii) envelope functions outside the spheres. The partial waves are the solution of radial Schrödinger equation times spherical harmonics for the isolated atom and exhibits orthogonally to the core states if needed. On other hand, the envelope function is expanded into plane waves or some other convenient basis set. However, both envelope function and partial-wave expansions are continuous at boundary of the sphere.

In PAW method, a linear transformation operator $\hat{T}$ maps the physically relevant AE wave functions, which are orthogonal to the core states, onto the computationally convenient Pseudo (PS) wave functions or vice versa. The PS wave functions will be identified with the envelop functions of the linear method [63] or the Pseudopotential approach. This approach is somewhat reminiscent of a change from the Schrödinger picture to the Heisenberg picture.

Linear transformation from pseudo wave functions to AE wave functions

$$|\Psi\rangle = \hat{T}|\Psi_l^{ps}\rangle \tag{2.60}$$

where l is a quantum state label, consisting of a band index and possibly a spin and k-vector index. The linear transformation operator

$$\hat{T} = 1 + \hat{T}_R \tag{2.61}$$

where $\hat{T}_R$ is non-zero only within some spherical augmentation region Ω_R enclosing atom R and unity outside this region where AE and PS wave functions coincide with each other. The augmentation spherical regions are chosen such a way that there is no overlap between the spheres. Around each atom, it is useful to expand the pseudo wave function into pseudo partial waves:

$$|\Psi_l^{ps}\rangle = \sum_{iR} c_{li}{}^{R}|\phi_{li}^{ps\,R}\rangle \text{ within } \Omega_R \tag{2.62}$$

The corresponding AE wave function is of the form

$$|\Psi\rangle = \hat{T}|\Psi_l^{ps}\rangle \tag{2.63}$$

$$|\Psi\rangle = \hat{T}\sum_{iR} c_{li}{}^{R}|\phi_{li}^{ps\,R}\rangle \tag{2.64}$$

$$|\Psi\rangle = \sum_{iR} {c_{li}}^{R} |\phi_{li}^{R}\rangle \text{ within } \Omega_R \tag{2.65}$$

with ${c_{li}}^{R}$ same as in pseudo partial wave expansions. Hence, we can express the AE wave function as

$$\begin{aligned} |\Psi\rangle &= \left(1 + \hat{T}_R\right) \left|\Psi_l^{ps}\right\rangle = \left|\Psi_l^{ps}\right\rangle + \hat{T}_R \left|\Psi_l^{ps}\right\rangle \\ &= \left|\Psi_l^{ps}\right\rangle + \left(\hat{T} - 1\right) \Big| \sum_{iR} {c_{li}}^{R} |\phi_{li}^{ps\,R}\rangle \\ &= |\Psi_l^{ps}\rangle + \sum_{iR} {c_{li}}^{R} |\phi_{li}^{R}\rangle - \sum_{iR} {c_{li}}^{R} |\phi_{li}^{ps\,R}\rangle \end{aligned} \tag{2.66}$$

where the expansion coefficients for the partial wave expansions have to be determined. Because the operator $\hat{T}$ is linear, the coefficients ${c_{ni}}^{R}$ are linear functions of pseudo wave functions and thus, can be written as an inner product with a set of so-called projector functions, $|p_i^{ps}\rangle$

$${c_{li}}^{R} = \left\langle p_i^{ps} \middle| \, \Psi_{li}^{ps\,R} \right\rangle \tag{2.67}$$

where $\left\langle p_i^{ps} \middle| \phi_{lj}^{ps\,R} \right\rangle = \delta_{ij}$ and $\sum_i \left|\phi_{li}^{ps\,R}\right\rangle \left\langle p_i^{ps}\right| = 1$

The most general form for the projector functions is

$$|p_i^{ps}\rangle = \sum_j \left(\left\{\left\langle f_k \middle| \phi_{lm}^{ps\,R} \right\rangle\right\}\right)_{ij}^{\;-1} \langle f_j| \tag{2.68}$$

where $|f_j\rangle$ form an arbitrary, linearly independent set of functions. The projector functions are localized within Ω_R if the functions $|f_j\rangle$ are localized. The final form of the linear transformation operator can be written as

$$\hat{T} = 1 + \sum_{iR} \left(|\phi_{li}^{R}\rangle - |\phi_{li}^{ps\,R}\rangle\right) \langle p_i^{ps}| \tag{2.69}$$

which allows one to obtain AE Kohn-Sham wave function as

$$|\Psi\rangle = |\Psi_l^{ps}\rangle + \sum_{iR} \left(|\phi_{li}^{R}\rangle - |\phi_{li}^{ps\,R}\rangle\right) \langle p_i^{ps} | \Psi_l^{ps}\rangle \tag{2.70}$$

explicitly separating the extended-space and the atom-centered contributions. A schematic representation of PAW method is shown in Figure 2.4. The first term can be evaluated on a plane wav or any convenient basis set, while the last two terms are evaluated on fine radial grids.

In summary, PAW transformation has three properties:

i) Projector functions are localized inside the augmentation spheres i.e., $p_i^{ps\,R}(r) = 0\, for\, r > R_a$

ii) AE orbitals and pseudo orbitals are equal outside the augmentation spheres

$$\phi_{li}^{R} = \phi_{li}^{ps\,R}, r > R_a \tag{2.71}$$

iii) Projector functions are orthogonal to pseudo orbitals, i.e., $\langle p_i^{ps} | \phi_{lj}^{ps\,R} \rangle = \delta_{ij}$

The partial waves ϕ_{li}^{R}, which are used as an atomic basis for the all-electron wavefunctions within the augmentation sphere, are constructed as radial solutions of the Schrodinger equation for the isolated atom.

Approximations

Like other electronic structure methods some approximations are needed to make PAW method a practical scheme within the DFT formalism. These approximations are:

- Frozen Core

  The frozen core approximation assumes that the core states are invariant under the different chemical environments and localized in the augmentation spheres. No projector functions are needed to define for the core states.

- Finite number of projectors

  The number of projector functions is obviously finite. Typically two projectors per angular momentum are used.

- Truncated angular momentum expansions

- Overlapping augmentation spheres

Expectation Values in PAW

we can obtain physical quantities, represented as the expectation value (A) of some operator A, from the PS wave functions $|\Psi_l^{ps}\rangle$ either directly as $\langle\Psi|A|\Psi\rangle$ after transformation to the true AE wave functions $|\Psi\rangle = \hat{T}|\Psi_l^{ps}\rangle$ or as the expectation value $\langle A\rangle = \langle\Psi_l^{ps}|A^{ps}|\Psi_l^{ps}\rangle$ of PS operator $A^{ps} = \hat{T}^{\dagger} A\,\hat{T}$ in the Hilbert space of the PS wave functions. Similarly we can evaluate the total energy directly as a functional of the PS wave functions. The ground-state PS wave functions can be obtained from

$$\frac{\partial E[\hat{T}|\Psi_l^{ps}\rangle]}{\partial\langle\Psi_l^{ps}|} = \epsilon\,\hat{T}^{\dagger}\,\hat{T}|\Psi_l^{ps}\rangle \qquad (2.72)$$

Expectation values in PAW

Total energy:

$$E = E_l^{ps} + \sum_a (E_l^{R\,a} - E_l^{ps\,a}) \qquad (2.73)$$

Electron density:

$$n(\boldsymbol{r}) = n_l^{ps}(r) + \sum[n_l^{R\,a}(\boldsymbol{r}-\boldsymbol{R}^a) - n_l^{ps\,a}(\boldsymbol{r}-\boldsymbol{R}^a)] \qquad (2.74)$$

Periodic Supercell Approximation

Although Kohn-Sham equations reduce the interacting many-electron Schrödinger equation into an effective single-problem, however, solving infinite number of non-interacting Schrödinger equation with infinite basis set computationally is formidable task. This cumbersome task can be simplified performing calculation on the periodic supercell approximation and applying Bloch's theorem to the electronic wave functions.

Bloch's Theorem

Bloch's theorem states that in a periodic solid each electronic wave function can be written as the product of a periodic unit cell part and a wave like part,

$$\psi_i(\boldsymbol{r}) = f_i(\boldsymbol{r})e^{i\boldsymbol{k}.\boldsymbol{r}} \tag{2.75}$$

where $f_i(\boldsymbol{r})$ periodic unit cell part i.e., $f_i(\boldsymbol{r}) = f_i(\boldsymbol{r}+\boldsymbol{l})$. $f_i(\boldsymbol{r})$ can be expanded using a discrete basis set of plane waves such as

$$f_i(\boldsymbol{r}) = \sum_{\boldsymbol{G}} c_{i,\boldsymbol{G}}\, e^{i\boldsymbol{G}.\boldsymbol{r}} \tag{2.76}$$

where $\boldsymbol{G}$ are the reciprocal lattice vectors defined by $\boldsymbol{G}.\boldsymbol{l} = 2\pi m$ for all $\boldsymbol{l}$ where $\boldsymbol{l}$ is a lattice vector of the crystal and m is an integer.

Hence, each electronic wave function can be written as

$$\psi_i(\boldsymbol{r}) = \sum_{\boldsymbol{G}} c_{i,\boldsymbol{K}+\boldsymbol{G}}\, e^{i(\boldsymbol{G}+\boldsymbol{k}).\boldsymbol{r}} \tag{2.77}$$

or equivalently

$$\psi_i(\boldsymbol{r}+\boldsymbol{l}) = \sum_{\boldsymbol{G}} c_{i,\boldsymbol{K}+\boldsymbol{G}}\, e^{i(\boldsymbol{G}+\boldsymbol{k}).(\boldsymbol{r}+\boldsymbol{l})} \tag{2.78}$$

$$\psi_i(\boldsymbol{r}+\boldsymbol{l}) = e^{i\boldsymbol{k}.\boldsymbol{l}} \sum_{\boldsymbol{G}} c_{i,\boldsymbol{K}+\boldsymbol{G}}\, e^{i\boldsymbol{k}.\boldsymbol{r}}\, e^{i\boldsymbol{G}.(\boldsymbol{r}+\boldsymbol{l})} \tag{2.79}$$

$$\psi_i(\boldsymbol{r}+\boldsymbol{l}) = e^{i\boldsymbol{k}.\boldsymbol{l}} f_i(\boldsymbol{r}+\boldsymbol{l})\, e^{i\boldsymbol{k}.\boldsymbol{r}} = e^{i\boldsymbol{k}.\boldsymbol{l}} f_i(\boldsymbol{r})\, e^{i\boldsymbol{k}.\boldsymbol{r}} \tag{2.80}$$

$$\psi_i(\boldsymbol{r}+\boldsymbol{l}) = e^{i\boldsymbol{k}.\boldsymbol{l}}\, \psi_i(\boldsymbol{r}) \tag{2.81}$$

Imposing periodic boundary condition envisioning the lattice (Figure 2.5) to be in the form of a closed N-atom ring, one must have

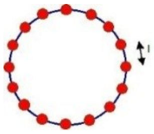

Figure 2.5 A closed N-atom ring.

$$\psi_i(\boldsymbol{r}+\boldsymbol{Nl}) = \psi_i(\boldsymbol{r}) \tag{2.82}$$

which in turn requires

$$e^{i\boldsymbol{k}.\boldsymbol{Nl}} = 1 \tag{2.83}$$

Or, $$k = \frac{2\pi n}{Nl} \ldots\ldots\ldots\ldots. n = 0, \pm 1, \pm 2, \pm 3, \ldots\ldots, \pm \frac{N}{2} \tag{2.84}$$

Bloch’s representation with periodic boundary condition points out that the number of occupied electronic states is finite, at each k-point, even for infinite periodic systems. This advantage turns out the problem of computing an infinite number of wave functions to one of computing finite number wave functions at infinite number of k-points. Moreover, states with similar k vector are identical which allows one to replace electronic wave functions over a region of k space by the wave functions at a single k point. In that case, only finite number of appropriate sampled set of k-points is required inside the first

Brilluoin zone to calculate the electronic potential and therefore determine the total energy of the solid. This advantage reduces computational cost significantly.

Plane Wave Basis Sets

According Bloch's theorem it is possible to expand an electronic wave function at each k point interms of a discrete plane wave basis set. In quantum mechanics, an electronic wave function belongs to an infinite-dimensional Hilbert space. Thus in principle, given an electronic wave function $\psi_i(\boldsymbol{r})$, an infinite number of basis plane waves is required in order to reproduce it. However, the infinite number of plane wave basis set can be reduced considering only the plane waves which have kinetic energies less than a particular cutoff energy i.e., $\frac{\hbar^2}{2m}|\boldsymbol{K}+\boldsymbol{G}|^2 \leq E_{cut}$. This choice of a particular cutoff energy E_{cut}, which produces a finite basis set, is reasonable since the coefficients $c_{i,\boldsymbol{G}+\boldsymbol{K}}$ in Bloch's theorem (equation) with smaller kinetic energies are typically more important than those with higher kinetic energies. With plane wave basis set KS equations take following simpler form

$$\sum_{G'}[\frac{\hbar^2}{2m}|\boldsymbol{K}+\boldsymbol{G}|^2\delta_{GG'} + V^{eff}(G-G')]\,c_{i,\boldsymbol{K}+\boldsymbol{G}'} = \varepsilon_i c_{i,\boldsymbol{K}+\boldsymbol{G}'} \qquad (2.85)$$

In this form, kinetic energy is diagonal, and effective potential is expressed in Fourier space. The number of elements in Hamiltonian matrix is limited by the choice of E_{cut}.

The salient features of a plane-wave basis are:

1. Only E_{cut} is needed to control the convergence of the result.

2. Orthonormality and no dependence on atomic positions, i.e. no basis-set superposition error and Pulay forces.

3. Very efficient to compute integrals and derivatives in reciprocal space which makes the calculation of the matrix elements of the Hamiltonian easier and faster.

Despite these computational friendly features, plane wave basis sets have some drawbacks, especially for isolated systems, where the large number of plane waves is required. A large number of plane waves for a well-converged calculation increases computational cost. Plane waves, in fact, cannot take advantage of the vacuum to reduce the size of the basis. In order to conveniently reduce E_{cut}, smooth pseudopotentials must be employed. Furthermore efficient parallelization is problematic due to the mathematics of delocalized plane waves. The required Fourier transforms are actually very difficult to parallelize.

Computational Details

The present calculations were performed within the framework of the standard frozen-core projector augmented-wave (PAW) [57] method using DFT as implemented in Vienna *ab initio* simulation package (VASP 4.6) [64] [65] code. In the PAW method, a non-linear core-correction is not necessary because it is an all-electron-like method. Exchange and correlation potential were treated in the generalized gradient approximation (GGA) as parameterized by Perdew-Burke-Ernzerhof (PBE) [25] [66]. The PBE functional does not contain any empirically optimized parameters, and hence works better on a wide range of elements. It is well known that underestimation of electron localization is a major failure of both DFT-LDA and DFT-GGA calculations, in particular, for systems with localized d and f electrons [67] [68] [69]. This failure manifests the general trend of DFT to underestimate the band gap and to produce incorrect metallic solutions for some $3d$ based metal oxides. In order to correct this shortcoming, we employ an on-site Coulomb correlation through the Hubbard-based U correction parameter [67] [48] [52] in the calculations. In the present work, we have used U=7eV that externally provides Coulomb correlation of 7eV to $Cu\,3d$ orbital. To compensate extra magnetic effect caused by U parameter Stoner exchange parameter $j = 1\ eV$ was used The basis sets were expanded with plane-waves with a kinetic energy cut-off of 400 eV, and the BZ integrations were performed using the second-order Methfessel-Paxton method [70]. However, density-of-states (DOS) plots were generated with the tetrahedron method [71]. The ion positions and volumes were always relaxed without any symmetry constraint to allow the internal geometry and the shape of the lattice to change freely and until the force on each of the ion was 0.01 eV/Å or less.

In the present work, we have studied the optical absorption as one of the most important optical property in PEC hydrogen production. In treating a solid, it is necessary to consider contributions to the absorption from various electronic energy band processes such as intraband, interband. However, we restrict ourselves to the interband processes because intraband processes are less important to semiconductors [24].

Optical absorption

All the semiconductors have a fundamental absorption edge in the near-infrared, visible or ultraviolet spectral region. The absorption edge is caused while electrons absorbing photon make an interband transition from an occupied state in the valence band to an unoccupied state in the conduction band. The probability of interband transition across the band gap in semiconductor is governed by a parameter called absorption coefficient, which is given by [24] [72] [73]

$$\alpha(\omega) = \frac{2\omega k_{ii}(\omega)}{c}$$

Where ω is the frequency of absorbed light, c be the speed of light, and $k_{ii}(\omega)$ is the extinction coefficients which are directly related to the diagonal components of frequency dependent complex dielectric tensors, ϵ_{ii} and have the following expression [72] [73] [74]:

$$k_{ii}(\omega) = \frac{1}{\sqrt{2}}\left[\{(Re\ \epsilon_{ii})^2 + (Im\ \epsilon_{ii})^2\}^{1/2} - Re\ \epsilon_{ii}\right]^{1/2}$$

Once the ground state was determined, frequency dependent dielectric matrix had been evaluated using VASP 5.2. which calculates directly [75] imaginary part using the equation :

$$Im\ \epsilon_{ij}(\omega) = \frac{4\pi^2 e^2}{\Omega} \lim_{q\to 0} \frac{1}{q^2} \sum_{c,v,\boldsymbol{k}} 2\omega_{\boldsymbol{k}} \delta(\epsilon_{c\boldsymbol{k}} - \epsilon_{v,\boldsymbol{k}} - \omega)$$

$$\times \langle u_{c\boldsymbol{k}+\boldsymbol{e}_i\boldsymbol{q}} | u_{v\boldsymbol{k}} \rangle \left\langle u_{c\boldsymbol{k}+\boldsymbol{e}_j\boldsymbol{q}} \middle| u_{v\boldsymbol{k}} \right\rangle^*$$

and real part with the usual Kramers-Kronig transformation:

$$Re\ \epsilon_{ij}(\omega) = 1 + \frac{2}{\pi} P \int_0^\infty \frac{[Im\ \epsilon_{ij}(\omega')]\omega'}{\omega'^2 - \omega^2 + i\eta} d\omega'$$

where P denotes the principle value and η is the complex shift.

It is necessary to have enough k-points to have all the distinct peaks in absorption curve at different energies while absorption takes place beyond the threshold energy. Moreover, enough empty conduction bands and a large number of grid points in DOS are required in the optical properties calculations. We have used different Monkhorst–Pack k-point samplings and different number of empty conduction bands for different structure which were enough to utilize the maximum efficiency of our available computing facility. The number of empty conduction bands were taken for $CuWO_4$ and $CuBiW_2O_8$. However, 2000 grid points in DOS were used to obtain more accurate results in all cases. The value of small complex shift η was taken 0.1 in the Kramers-Kronig transformation.

All computations were performed using the High Performance Computing Facility (HPCF) at the University of Texas at Arlington. For visualization and the X-ray diffraction (XRD) of the crystal structures, VESTA (Visualization for Electronic and Structural Analysis) [76] [77] was used.

Chapter 3

Tungsten Oxide (WO_3)

Introduction

Tungsten (VI) oxide, also known as tungsten trioxide or tungstic anhydride, WO_3, is obtained as an intermediate in the recovery of tungsten from its minerals [78]. WO_3 is one of the most important, highly pure intermediates for the production of other tungsten compounds and tungsten metal powder. It is one of the photocatalysts that is sensitive to visible light [79] [80] and shows high O_2 activity. However, it does not show any activity for H_2 evolution under any light irradiation because of the lower position of $W\ 5d$ conduction bands in WO_3 with respect to the $H^+/\ H_2$ potential level [20].

The structure of WO_3 is best described as a three dimensional network of corner sharing WO_6 octahedra. The connectivity of this network is identical to the cubic ReO_3 structure (Figure 3.1a) and the ABO_3 perovskite structure where A cations are missing and B is replaced by W (Figure 3.1b). However, the symmetry of WO_3 is lowered from the ideal ReO_3 structure by two distortions: tilting of WO_6 octahedra and displacement of tungsten from the center of its octahedron. Variations of these distortions at different temperatures give rise to several phase transitions. Hence, the structure of pure WO_3 crystal is temperature dependent and belongs to five different phases between absolute zero and its melting point at 1700 K [22] [81] [82] [83]. These are tetragonal or $\alpha-$phase, orthorhombic or $\beta-$phase, monoclinic room-temperature (RT) or $\gamma-$phase, triclinic or $\delta-$phase, and monoclinic low-temperature (LT) or $\varepsilon-$phase. When the temperature is decreased from the melting point, the hierarchy of polymorphism of WO_3 adopts the

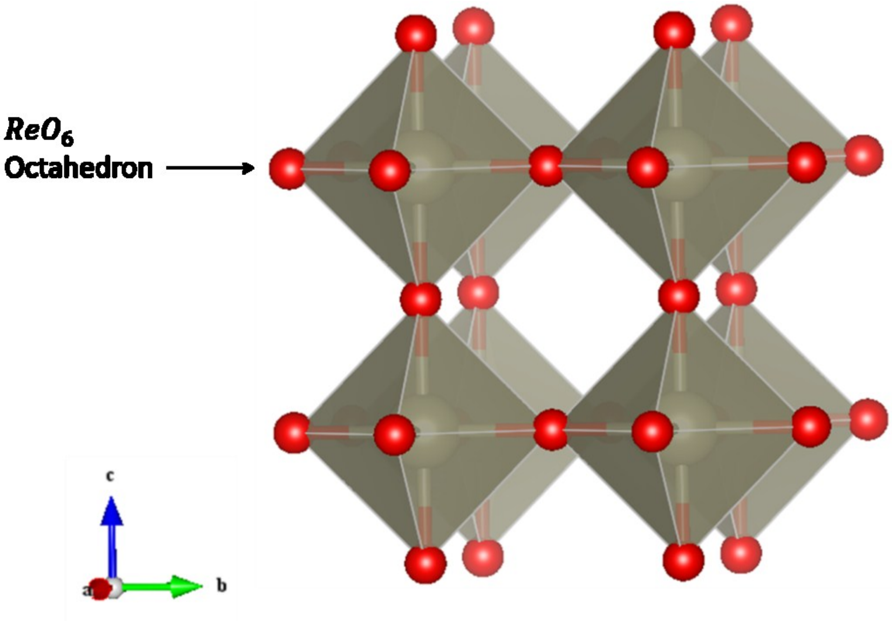

(a)

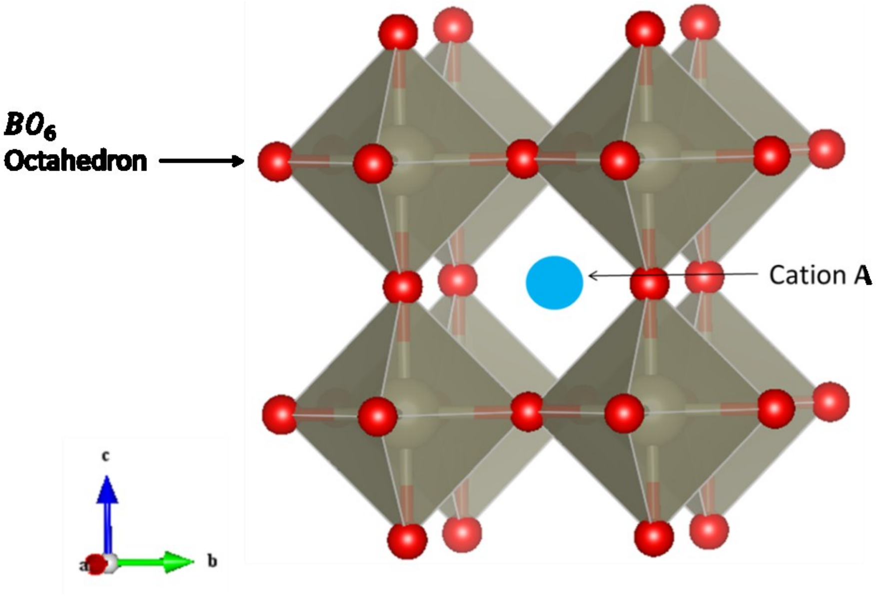

(b)

Figure 3.1 (a) Perspective view of the cubic structure of ReO_3, drawn as corner-linked ReO_6 octahedra; (b) the idealized cubic ABO_3 perovskite structure [84].

following sequence: $\alpha-$phase → $\beta-$phase → $\gamma-$phase → $\delta-$phase $\varepsilon-$phase. Tetragonal ($\alpha-$phase) WO_3 itself exists in three different phases at three different temperatures [85]. The different phases and symmetry possessed by WO_3 at different temperatures are presented in Table 3.1. The simplified cubic structure of ideal WO_3 is shown in Figure 3.2. Tetragonal phases $P4/ncc$ and $P\bar{4}2_1m$ at high temperatures are the subgroups of another tetragonal phase $P4/nmm$;. $P4/nmm$ corresponds with $P\bar{4}2_1m$ via an M-point transition [85]. Although $P4/ncc$ and $P\bar{4}2_1m$ have different unit cell formula, but the cell volumes are same in both cases [88] [87]. Apart from temperature dependence WO_3 also adopts monoclinic structure ($P2_1/c$) at high pressure from 1.2 kbar to 47 kbar [93]. However, monoclinic room-temperature (RT) or $\gamma-WO_3$ represents the thermodynamically most stable phase among all. Hence, we choose $\gamma-WO_3$ for our present work and following subsections in this chapter belong to only this phase.

Table 3.1 Known Polymorphs of Tungsten Trioxide.

Crystal Phase	Crystal System	Space Group	Z	Temperature Range (°K)	
$\alpha-WO_3$	Tetragonal	$P4/nmm$	2	1170-1700	[86]
		$P4/ncc$	2	1100-1170	[85]
		$P\bar{4}2_1m$	4	730-1100	[87]
$\beta-WO_3$	Orthorhombic	$Pnmb$	8	600-730	[88]
$\gamma-WO_3$	Monoclinic	$P2_1/n$	8	290-600	[89]
$\delta-WO_3$	Triclinic	$P\bar{1}$	8	230-290	[90] [91]
$\varepsilon-WO_3$	Monoclinic	Pc	4	0-230	[92]

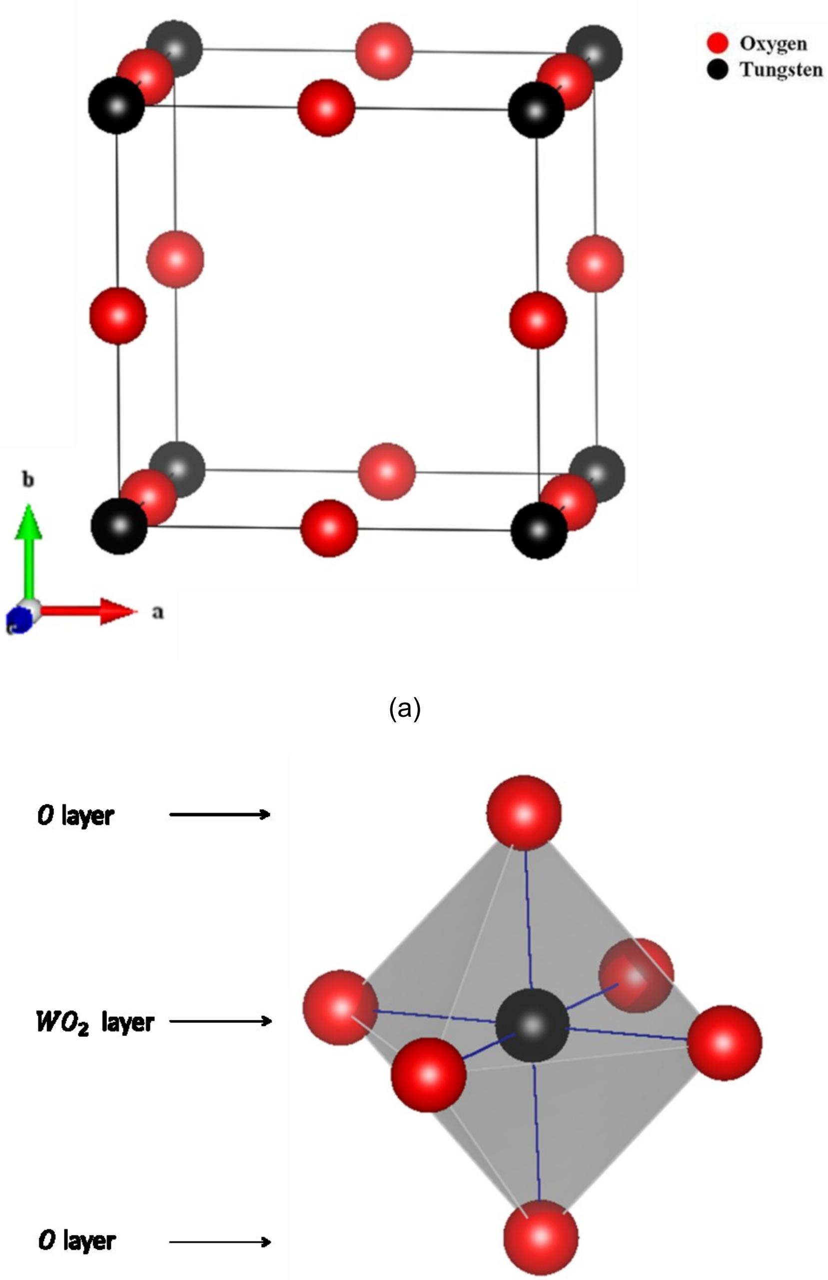

(a)

(b)

Figure 3.2 The structure of WO_3. (a) The ideal cubic structure of WO_3 and (b) The WO_6 octahedra. The alternating WO_2 and O layers are also indicated.

Monoclinic Room-Temperature (RT) or $\gamma - WO_3$

Monoclinic room-temperature (RT) or $\gamma - WO_3$ exists from 17℃ to 300℃ [81] and possess $P2_1/n$ $(S.G.14, Z = 2)$ symmetry a with direct band gap 2.7 eV [27] . It exhibits the basic structural characteristics, i.e., W forms corner-sharing WO_6 octahedra with corner-sharing six O atoms. It can be viewed as a distorted cubic WO_3 structure-three-dimensional array of slightly distorted corner-shared WO_6 in a nearly cubic arrangement. This structure can also be considered as consisting of $W - O - W$ like chains, where the chains are connected across the W atoms, as seen in Figure 3.1. The smallest monoclinic unit cell of WO_3 consists of 8 W atoms and 24 O atoms and contains eight tilted WO_6 octahedra.

Computational Details

The optimization of monoclinic room-temperature (RT) or $\gamma - WO_3$ was done using $2 \times 2 \times 2$ Monkhorst–Pack [94] k-point sampling; however, a more refined $7x7x7$ k-point sampling was used for density-of-states (DOS) calculation. For optical absorption calculation, we have used $9x9x9$ k-point sampling. The number of empty bands taken in the conduction band was 400. All the calculations of WO_3 were performed in the context of DFT-GGA.

Results

a.Structural Properties

Figure 3.3 represents the optimized unit cell of monoclinic room-temperature (RT) or $\gamma - WO_3$. The octahedra shown in Figure 3.3a are more tilted than experimental [90], LDA [95], or previous GGA [81] results, however, the size of each octahedron is almost identical in all cases. Unlike the general tendency of GGA, our calculation produces a lower equilibrium volume compared to LDA and experimentally measured value, even smaller than the previous GGA calculations. The difference in previous GGA and our GGA can be attributed to the different parameterizations and implementation of different potential methods. In the previous GGA case [81], which was parameterized by Perdew and Zunger, incorporated ultrasoft pseudopotential whereas our GGA was parameterized by Perdew-Burke-Ernzerhof (PBE) incorporating projector augmented method (PAW). The difference in equilibrium volumes merely corresponds to the difference in the interactions between the octahedra, i.e., the different "angular potentials" [81]. The comparison between experimental value, LDA, and GGA is shown in Table 3.2. As in the literature [81], a splitting into long and short bonds with different magnitude along a, b, and c directions is also evident in our case (Table 3.3). Few $W - O$ bonds along b $(or\ b^*)$ and $(\ or\ c^*)$ directions are strongly elongated than that of along a $(or\ a^*)$ direction. The X-ray diffraction (XRD) pattern of our optimized monoclinic RT WO_3 is shown in Figure. 3.4, and is in good agreement with experimental XRD [96].

Table 3.2 A comparison between experimental and DFT results for $\gamma - WO_3$.

Crystal		Lattice Constants (Å)			Lattice Angles (°)			Volume (Å^3)	Band Gap (eV)
		a	b	c	α	β	γ		
$\gamma - WO_3$	Exp. [90]	7.306	7.540	7.692	90	90.88	90	423.69	2.7
	DFT+LDA [95]	7.381	7.472	7.633	90	90.6	90	420.94	1.31
	DFT+GGA [81]	7.55	7.62	7.83	90	90.2	90	450.46	0.90
	DFT+GGA	7.265	7.472	7.492	90	91.99	90	406.45	1.845

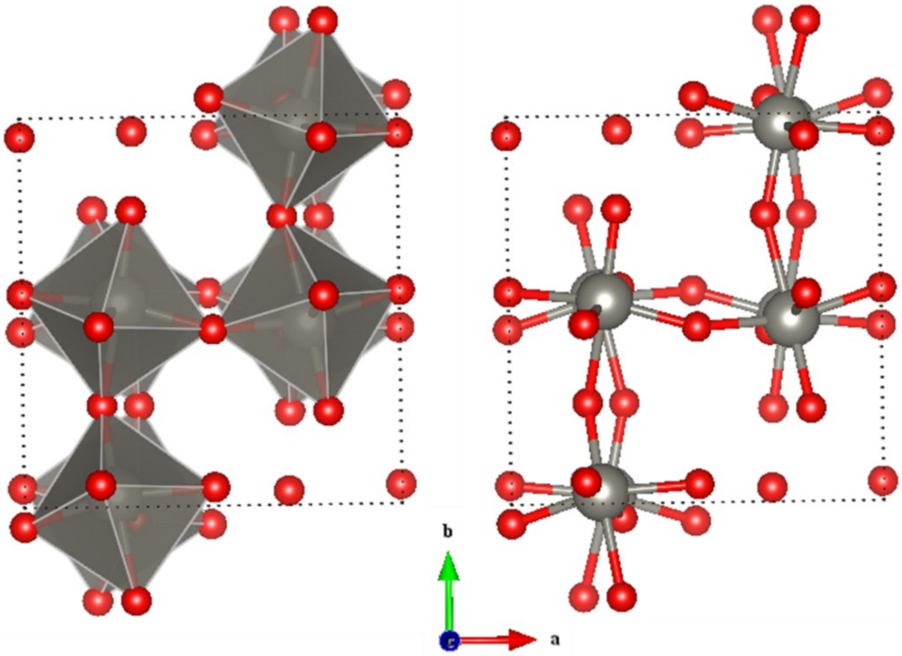

(a) (b)

Figure 3.3 Optimized unit cell of monoclinic RT WO_3 viewed in two different styles: (a) Polyhedral and (b) ball and stick.

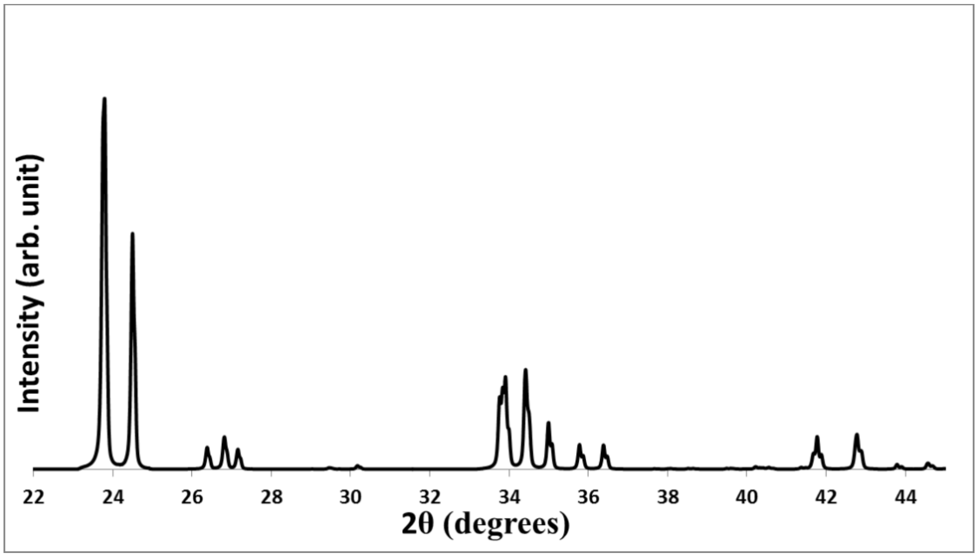

Figure 3.4 X-diffraction (XRD) pattern of monoclinic RT or $\gamma - WO_3$.

Table 3.3 Different $W-O$ bond lengths for $\gamma-WO_3$. (*) indicates negative direction.

Bonds		Distances (Å)	Bonds		Distances (Å)
$W1-$	$O1$	1.89739 (a)	$W2-$	$O2$	1.95053 (a)
	$O6$	1.91727 (a^*)		$O5$	1.86965 (a^*)
	$O9$	1.79975 (b)		$O10$	1.79931(b^*)
	$O16$	2.07592 (b^*)		$O15$	2.07401(b)
	$O17$	2.08550 (c^*)		$O18$	2.08770 (c)
	$O24$	1.80244 (c)		$O23$	1.80089 (c^*)
$W3-$	$O3$	1.89703 (a^*)	$W4-$	$O4$	1.95049 (a^*)
	$O8$	1.91737 (a)		$O7$	1.86957 (a)
	$O11$	1.79956 (b^*)		$O12$	1.79942 (b)
	$O14$	2.07609 (b)		$O13$	2.07399 (b^*)
	$O19$	2.08543 (c)		$O20$	2.08773 (c^*)
	$O22$	1.80258 (c^*)		$O21$	1.80089 (c)
$W5-$	$O3$	1.91919 (a)	$W6-$	$O4$	1.86914 (a)
	$O8$	1.89756 (a^*)		$O7$	1.94807 (a^*)
	$O12$	2.07729 (b^*)		$O11$	2.07515 (b)
	$O13$	1.80604 (b)		$O14$	1.80557 (b^*)
	$O17$	1.79558 (c)		$O18$	1.79543 (c^*)
	$O24$	2.08257 (c^*)		$O23$	2.08860 (c)
$W7-$	$O1$	1.91881 (a^*)	$W8-$	$O2$	1.86911 (a^*)
	$O6$	1.89776 (a)		$O5$	1.94797 (a)
	$O10$	2.07739 (b)		$O9$	2.07509 (b^*)
	$O15$	1.80588 (b^*)		$O16$	1.80578 (b)
	$O19$	1.79575 (c^*)		$O20$	1.79521 (c)
	$O22$	2.08216 (c)		$O21$	2.8905 (c^*)

b. Electronic Properties

The electronic band structure for $\gamma-WO_3$ is presented in Figure 3.5. which shows that $\gamma-WO_3$ is a direct semiconductor with band gap 1.845 eV along $\Gamma \rightarrow B$. This band gap is smaller than the experimental band gap by an amount 0.855 eV although had a better agreement compared to any previous DFT formalism. Our calculated band gap is most consistent with the recent literature [97] where 1.74 eV indirect band gap was found for $\gamma - WO_3$ using FP-LAPW in DFT-GGA. Our DFT–GGA band structure possesses almost same features like LDA [95], however, the marked difference is higher band gap than LDA, even higher than the previous GGA calculation [81]. The significant increment of band gap can be attributed to use of PAW method in GGA parameterized by PBE that might have demonstrated extra push caused by valence band towards the conduction band. The top of the valance band is more dispersive than that of LDA. Valence bands are less closely packed compared to LDA.

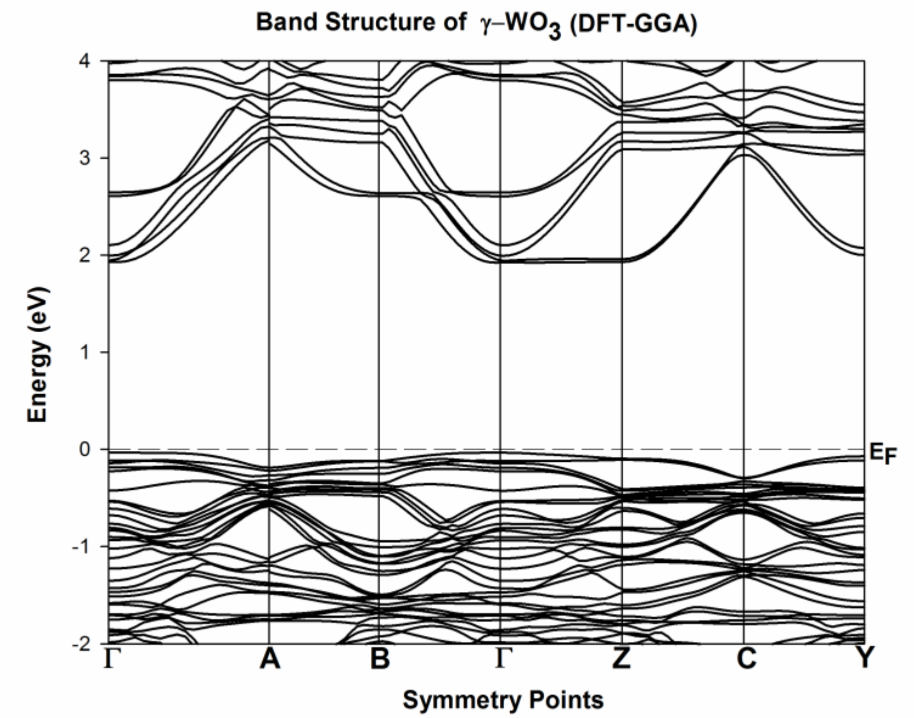

Figure 3.5 DFT-GGA electronic band structure of $\gamma - WO_3$.

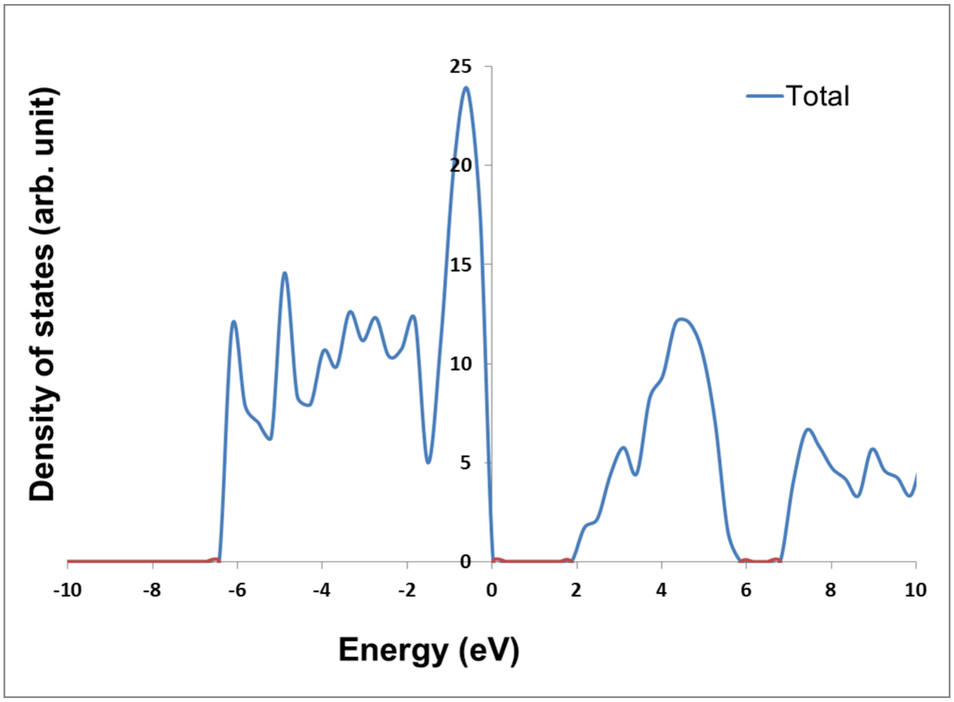

(a)

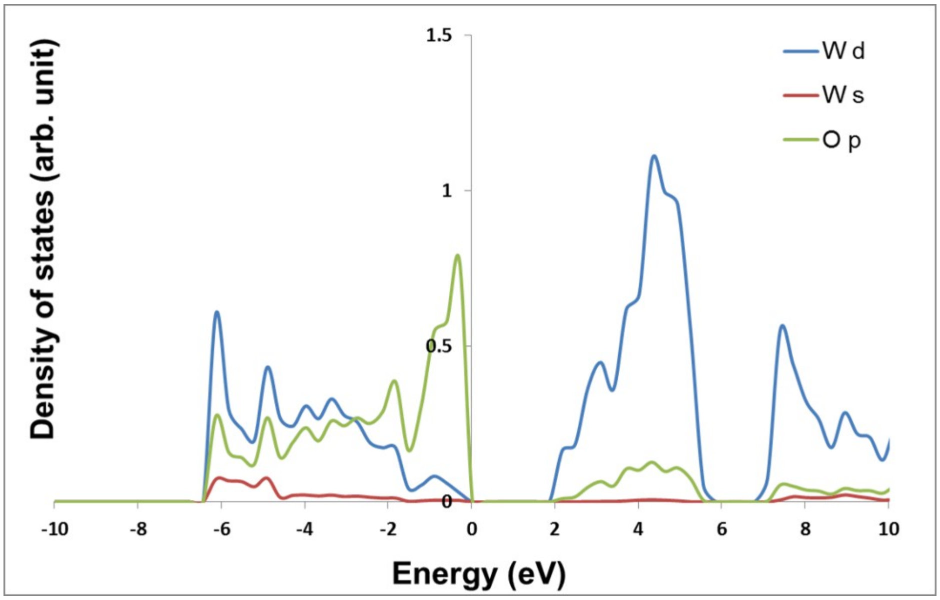

(b)

Figure 3.6 DFT- GGA a) Total and b) Partial density of states (DOS) of $\gamma - WO_3$.

Figure 3.6 shows the total and local DOS for $\gamma - WO_3$ which have same overall feature as LDA [95] except a valley around at -0.5 eV is missing in GGA. Like LDA Figure 3.6(b) also shows that, the valence band of WO_3 is dominated by $O\ 2p$ bands, while its conduction band consists of $W\ 5d$ character as one would as expected for a metal-oxide semiconductor. This typical feature in metal oxide facilitate favorable $p - d$ optical transition in WO_3.

c. Optical Absorption

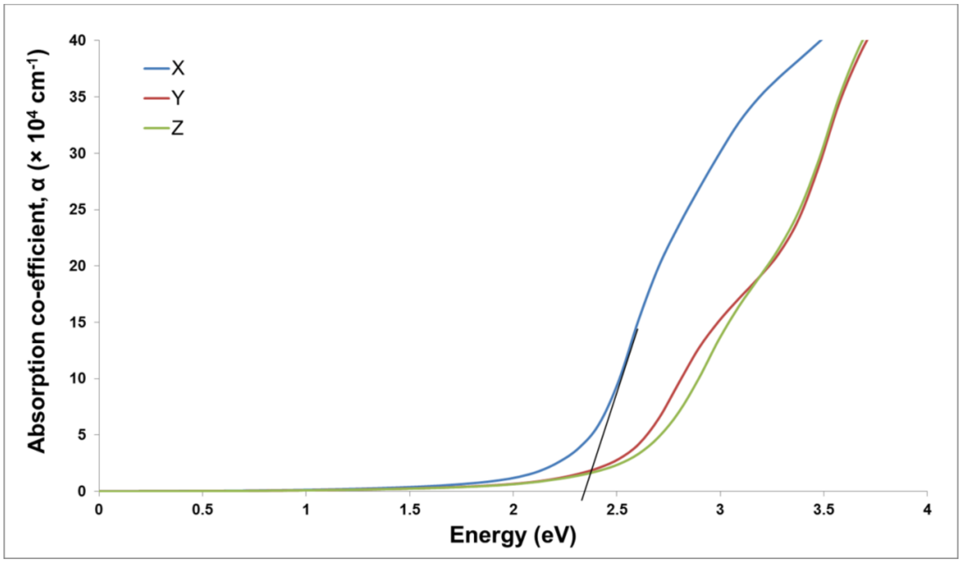

Figure 3.7 Optical absorption spectrum for DFT-GGA optimized WO_3.

Figure 3.7 represents optical absorption spectrum monoclinic RT WO_3 optimized by DFT-GGA. The optical band gap is found $\sim 2.4\ eV$ which is higher than calculated band gap. This absorption spectrum tells that the shortest distance transition i.e., transition between the top of the valence band and the bottom of the conduction band is forbidden. This DFT-GGA absorption is very much consistent with DFT-LDA

Chapter 4

Copper Tungsten ($CuWO_4$)

Introduction

Coppor tungstate, $CuWO_4$ or cuproscheelite [98], a n-type semiconductor with an indirect band gap 2.3 eV [99], crystallizes in a triclinic structure with symmetry $P\bar{1}$ [100]. Crystalline $CuWO_4$ results from the reactions [101]:

$$Cu_2O\ (s) + 2WO_3(s) + {}^{1}/_{2}\ O_2(g) \rightarrow 2CuWO_4(s)$$

$$CuO\ (s) + WO_3(s) \rightarrow CuWO_4(s)$$

In the structure of $CuWO_4$, both Cu and W surrounded by six oxygen atoms form CuO_6 and WO_6 octahedra [100] [102]. These two different octahedra connected by edge sharing form infinite zigzag chains. The CuO_6 octahedra possess two different kinds of connections between them in the structure of $CuWO_4$, which lead to alternating antiferromagnetic interactions along the chains [33]. Copper tungstate becomes antiferromagnetically ordered below 23.0 K [103]. The magnetic unit cell is the double of the unit (a,b,c) along 'a' direction and identical to that of $FeWO_4$ [104]. Although $CuWO_4$ is triclinic, its structure is topologically related to that of monoclinic wolframite ($P\,2/c$) [99] [103]. CuO_6 octahedra present a Jahn-Teller (JT) distortion to remove the degeneracy of $Cu^{2+}\ 3d$ orbitals. This distortion elongate the octahedron causing reduction in the symmetry from monoclinic to triclinic [99] [101]. WO_6 octahedra are more tilted compared to wolframite. The deviation of γ from $90°$ reflects the symmetry lowering and hence, the Jahn-Teller (JT) distortion. In the triclinic structure of $CuWO_4$, there are four distinct oxygen atoms (refer here as $O1, O2, O3,$ and $O4$) which occupy four different sites whereas monoclinic wolframite has only two distinct oxygen atoms (refer here as $O1$, and $O2$) occupying two different sites. The structural, electronic, and optical properties of $ZnWO_4$, which is a wolfarmite structure in AWO_4 family, are presented in Appendix B to compare with $CuWO_4$.

Computational Details

The optimization of $CuWO_4$ was done using $5 \times 9 \times 9$ Monkhorst–Pack [94] k-point sampling in both DFT and DFT+U cases, however, a more refined $9x13x13$ K-point sampling was used for density-of-states (DOS) calculation. We have used $5 \times 9 \times 9$ Monkhorst–Pack k-point sampling for optical calculations of the ground state $CuWO_4$ in both DFT and DFT+U that was the maximum efficiency of our current computing facility at the University of Texas at Arlington. The number of empty bands used in both DFT-GGA and DFT+U-GGA case was 300.

Results

a. Structural Properties

For our present work, we optimize four possible magnetic configurations: $i)$ spin-unrestricted, $ii)$ spin-restricted, and $iii)$ two possible antiferromagnetic (AFM) arrangements- for triclinic ($P\bar{1}$) and wolfarmite ($P\ 2/c$) $CuWO_4$. We choose the wolfarmite structure to optimize because of its topological proximity with triclinic ($P\bar{1}$) $CuWO_4$. The two possible antiferromagnetic (AFM) arrangements considered here are: $i)$ Cu with different spins along ‘a’ direction referred as AFM1 and $ii)$ electrons with the same spins along ‘a’ direction referred as AFM2 from now. Our optimization process determines that $CuWO_4$ adopts AFM2 triclinic phase as ground state in both DFT- GGA and DFT-GGA +U cases. The optimized energy and volume comparison between different structures are presented Table 4.1. In each magnetic phase, wolfarmite had the higher energy than that of triclinic one. On other hand, spin restricted configuration had the highest energy

($\Delta E = 0.15715\ eV$) compared to gound state among all triclinic magnetic phases. For this reason, DFT-GGA +U optimization was restricted to only three triclinic magnetic phases: spin-unrestricted, AFM1 and AFM2. The DFT-GGA +U optimizes AFM2 triclinic $CuWO_4$ with lattice parameters $a = 4.653685$ Å, $b = 5.80990$ Å, $c = 4.88819$ Å, $\alpha =$ 91.4936°, $\beta = 91.7646°$, and $\gamma =$ 84.3218°. These values are in good agreement with the literatures [50] [51] [102] [100] [105] [98] [106]. A comparison of energies, volumes, and lattice parameters between DFT-GGA, DFT+U-GGA and experimental results for triclinic $CuWO_4$ are shown in Table 4.2.

Table 4.1 DFT-GGA optimized energies and volumes of different structures for. $CuWO_4$.

Magnetic phase	Structure	DFT	
		Energy (eV)	Volume (Å^3)
Spin-Unrestricted	Triclinic	-92.406	131.29
	Wolframite	-92.298	128.56
Spin-Restricted	Triclinic	-92.324	131.07
	Wolframite	-92.171	127.93
AFM1	Triclinic	-92.428	131.39
	Wolframite	-92.178	128.06
AFM2	Triclinic	-92.481	131.47
	Wolframite	-92.262	128.22

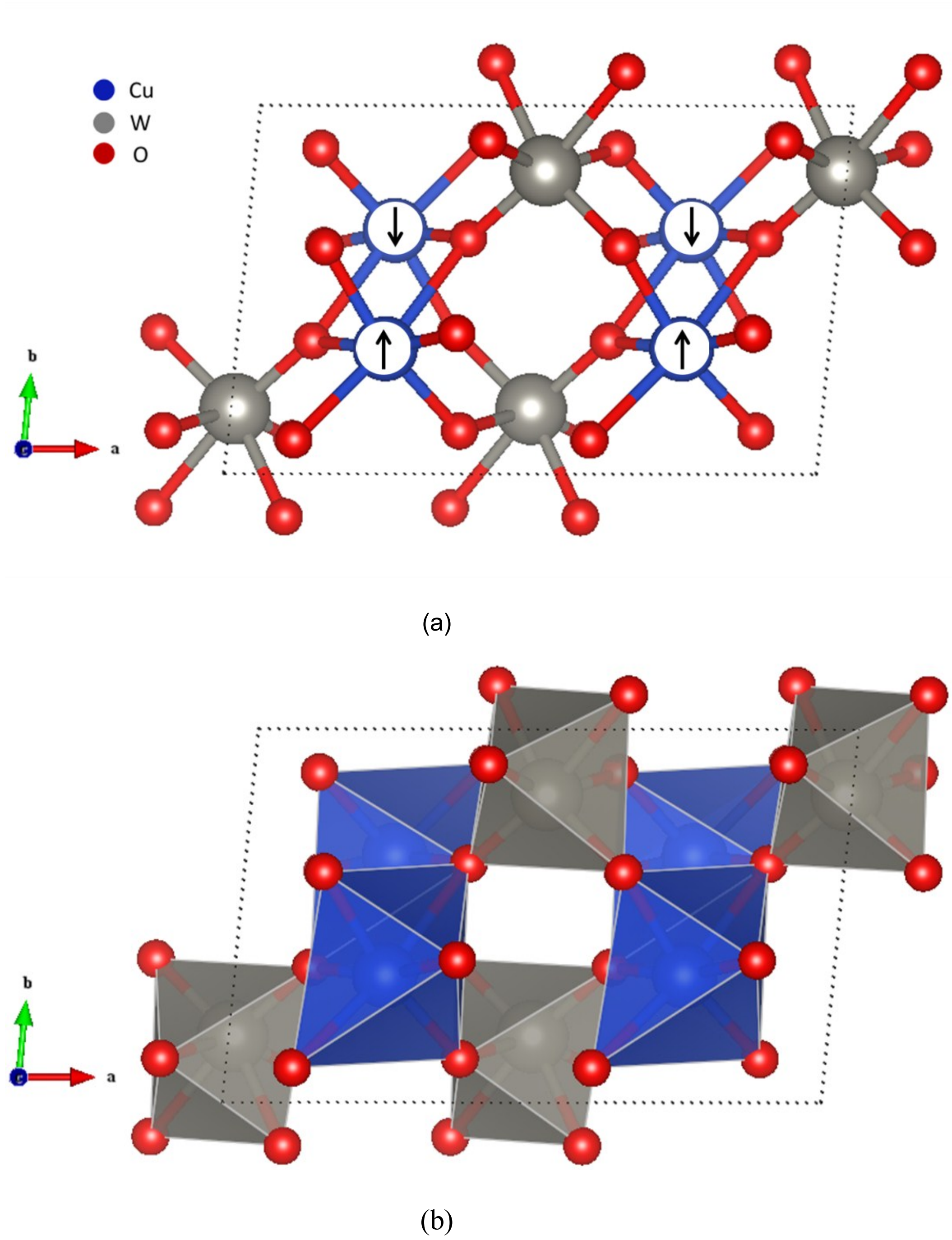

(a)

(b)

Figure 4.1 The two different models of DFT+U-GGA optimized structures for AFM2-$CuWO_4$ are shown in a) ball-and-stick and b) polyhedral, respectively '↑ ′ and '↓ ′ refer here spin up and spin down, respectively.

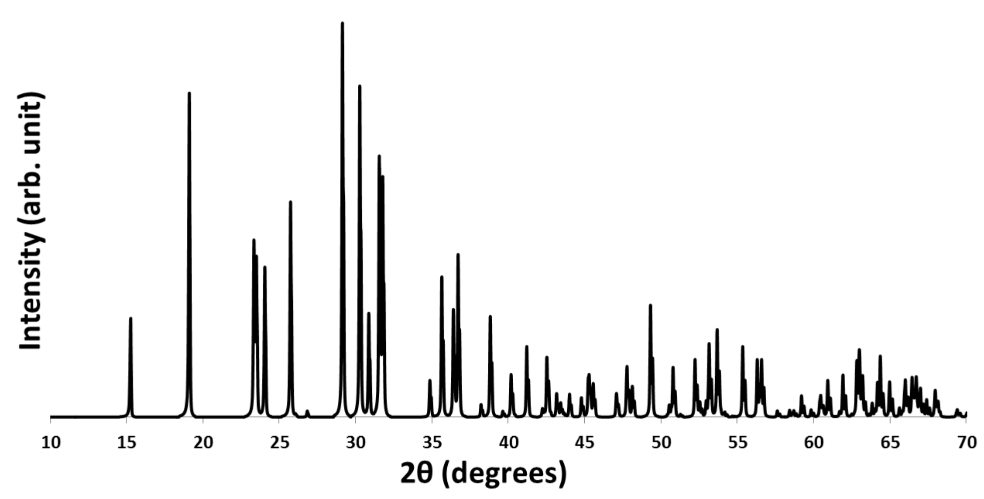

Figure 4.2 X-ray diffraction pattern for DFT+U-GGA optimized AFM2-$CuWO_4$.

Table 4.2 A comparison of energies, volumes, and lattice parameters between DFT-GGA, DFT+U-GGA and experimental results for triclinic $CuWO_4$.

	Magnetic Phase	Energy (eV)	Volume (Å^3)	Lattice Constants (Å)			Lattice Angles (°)		
				a	b	c	α	β	γ
DFT	Spin-unrestricted	-92.406	131.29	4.642	5.822	4.888	91.79	92.06	-92.41
	AFM1	-92.428	131.40	4.641	5.832	4.886	91.76	92.11	-92.43
	AFM2	-92.481	131.47	4.639	5.832	4.892	92.02	92.06	-92.48
DFT+U	Spin-unrestricted	-88.367	131.37	4.652	5.809	4.888	91.53	91.83	84.36
	AFM1	-88.366	131.41	4.650	5.815	4.887	91.51	91.84	84.33
	AFM2	-88.378	131.42	4.653	5.809	4.888	91.49	91.77	84.33
Exp.	AFM1			4.703	5.839	4.878	91.67	92.45	82.81

In AFM2 configuration, as shown in Figure 4.1a, all the Cu atoms in a single layer along 'a'-axis have same spins and produce local magnetic moment along that layer which differ with the literatures [103] [106]. However, four planar $Cu - O$ have shorter distances (~2 Å) than two axial $Cu - O$ distances (2.26-2.36 Å)- is an excellent agreement with the experimental result [99]. The rest of the structural features remain same in both DFT+U-GGA and experimental cases. The XRD, as shown in Figure 4.2, shows a good agreement with the experimental XRD [99] as well.

b. Electronic Properties

Our DFT-GGA electronic band structure calculation produces a very narrow but finite gap $(0.26\, eV)$ for AFM2- $CuWO_4$. This finite band gap was also observed with almost twice as of our value inm the literature [106], however, was unnoticed in literatures [99] [107] [108]. Two empty bands which are seen right after Fermi level for AFM $CuWO_4$ shown in Figure 4.3a, were also unperceived in the literatures [99] [107] [108]. These empty bands next to Fermi level often raise an issue of the credibility of conventional DFT calculation giving an incorrect band gap for highly localized $3d$ states cotaining metal oxides. DFT+U-GGA calculation, as shown in Figure 4.3b, opens up a gap (0.707 eV), however, too small to be compared with experimental band gap. The overall feature of band structure in DFT+U-GGA calculation remains same compared to DFT-GGA. M. V. Lalić et al. [109] in their recent work showed that band gap problem could be successfully tackled with the use of a modified Becke-Johnson (mBJ) exchange potential. Although their result had a better agreement with the experiment but could not present the rationales of $Cu\, 3d$ shift by an amount 1.5 eV towards $W\ 5d$ which is highly unlikely for strongly localized orbital like Cu 3d. We leave this band gap issue for future work since $CuWO_4$ is not the primary focus for the present

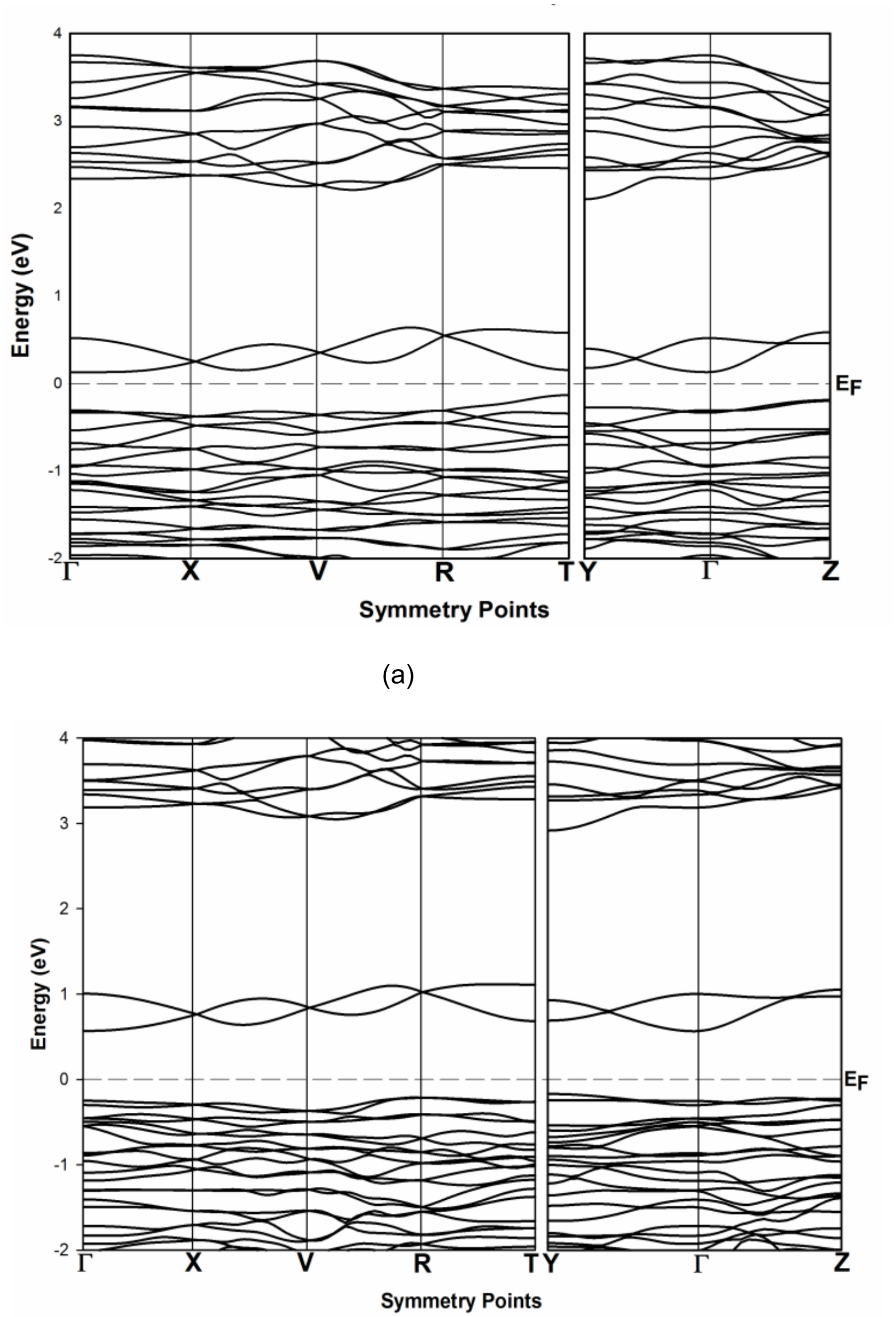

(a)

(b)

Figure 4.3 Electronic band structure calculation of triclinic AFM2-$CuWO_4$. (a) with DFT-GGA and (b) with DFT+U-GGA.

work. In Figure 4.3b, we see that indirect band gap (eV) located along $\Gamma \rightarrow Y$. The valence band along $\Gamma \rightarrow X$ is very flat suggesting higher effective mass of holes, along other symmetry points bands are more or less dispersive. The conduction band is divided into two regions. The first region contains only two bands which are dispersive throughout the all symmetry points. On the other hand, conduction bands of the second region are flat along $\Gamma \rightarrow X$, and $\mathrm{R} \rightarrow T$, however, dispersive along the other symmetry points.

DFT+U-GGA total and partial DOS plot of AFM1 triclinic $CuWO_4$ are presented in Figure 4.4a and Figure 4.4b, respectively. Figure 4.4b depicts the contribution of one atom from each species. From Figure 4.4b, the contribution at the top of valence band (VB) comes from the hybridization of $O\ 2p$ with $Cu\ 3d$. Both $Cu\ 3d$ and $O\ 2p$ dominant almost equally in DFT+U-GGA case. Since the no of O atoms are four times than that of Cu atoms per unit cell, the top of the valence band in total DOS plot (Figure 4.4a) is likely to be p orbital dominated. In contrary, $Cu\ 3d$ dominance is a way prominent than $O\ 2p$ in DFT-GGA (Figure 4.5b). Both $W\ 5d$ and $W\ 5p$ contributions around the valence band edge are very small like WO_3. On the other hand, bottom of the conduction band of first region is composed of $O\ 2p$, $W\ 5d$, and $Cu\ 3d$ orbitals (with the dominance of the latter). The next higher unoccupied conduction band which is shifted by almost 0.9 eV with respect of DFT+-GGA calculation (Figure 4.5b) are mostly $W\ 5d$ and $O\ 2p$ dominated. This $W\ 5d$ dominated higher conduction band resembles with the bottom of conduction band for insulating solution in the literature [59]. All of our DFT+U-GGA findings for AFM2 triclinic $CuWO_4$ are in agreement with the literature [106]. DFT-GGA

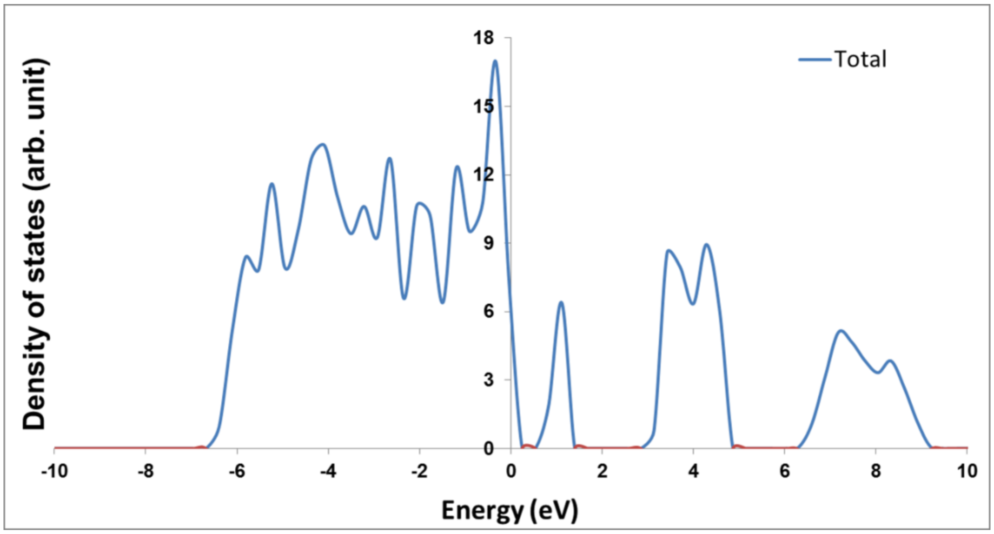

(a)

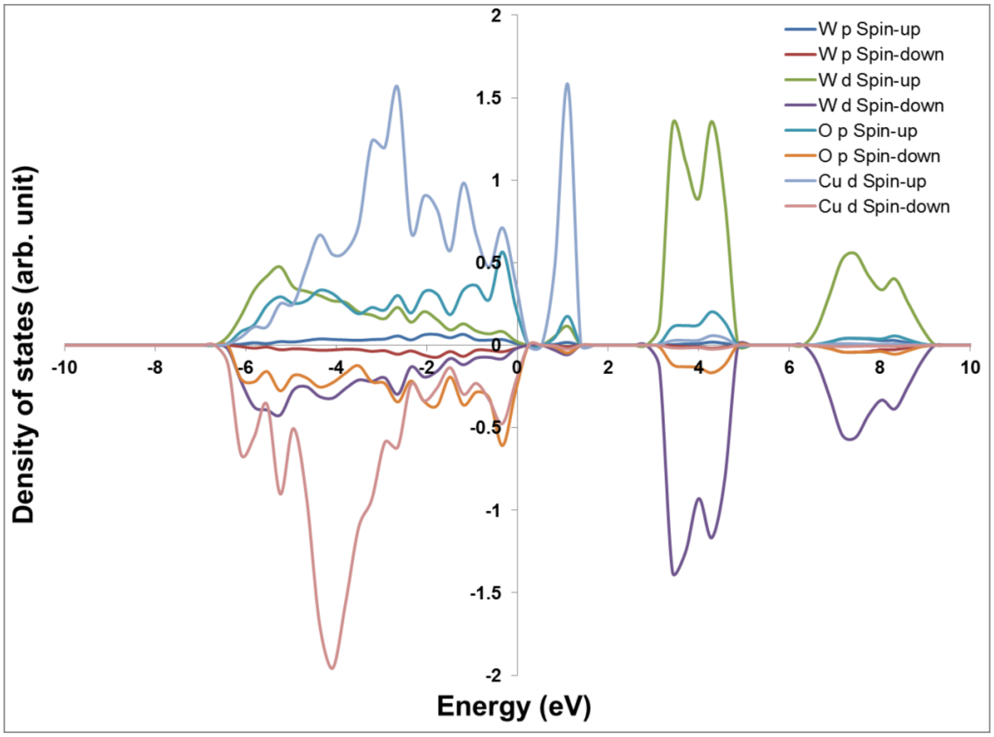

(b)

Figure 4.4 (a) Total and (b) partial density of states (DOS) of DFT+U-GGA AFM2-$CuWO_4$.

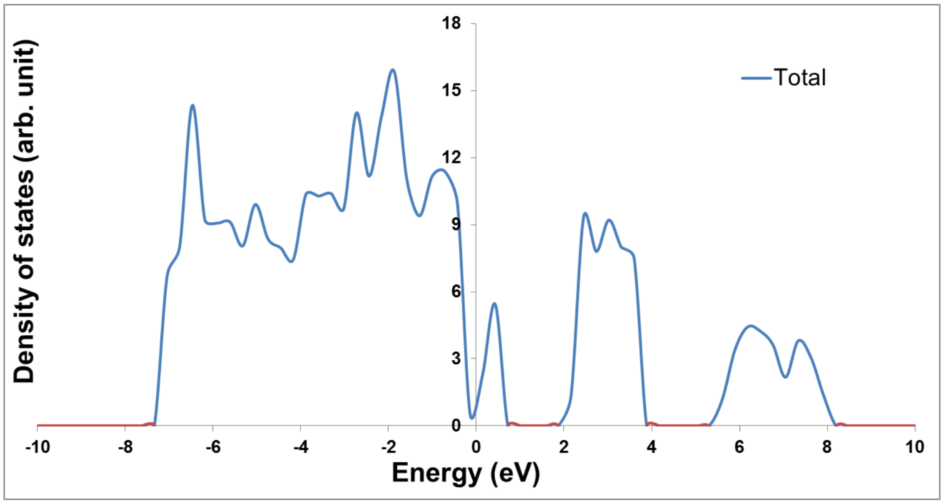

(a)

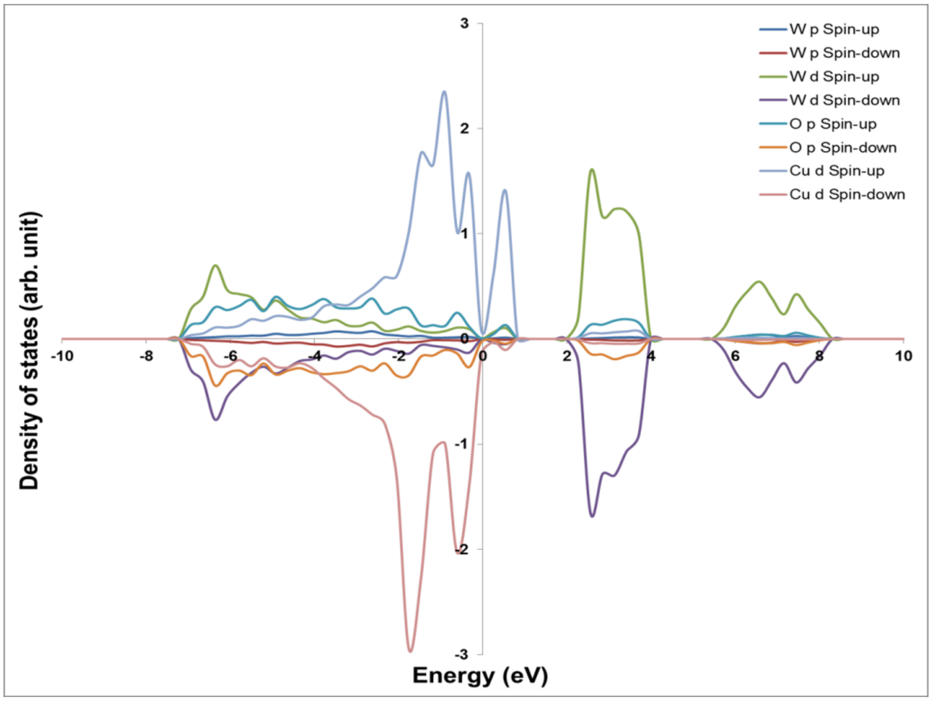

(b)

Figure 4.5 (a) Total and (b) Partial density of states (DOS) of DFT-GGA AFM1-$CuWO_4$.

c. Optical Absorption

Figure 4.6a and 4.6b portray the optical absorption spectrum of AFM $CuWO_4$ optimized in DFT-GGA and DFT+U-GGA schemes, respectively. Two absorption peaks , one is smaller than the other, in both cases. The DFT-GGA absorption spectrum exhibits the first peak at around 0.5 eV and the onset of the absorption is found at around $0\ eV$. On the other hand, the first peak in DFT+U-GGA absorption spectrum is observed at 3 eV shifted by 2.5 eV with respect to DFT-GGA counterpart. The onset of absorption takes place at around 2.1 eV which does not correspond to electronic band gap in DFT+U-GGA. Both these shifts compared to DFT-GGA happen due to U=7 eV parameter employed to $Cu\ 3d$ which splits bands (mostly $Cu\ 3d$) populated around Fermi level and pushes the empty $Cu\ 3d$ bands up. Since top of the valence band and bottom of the conduction band are dominated by $Cu\ 3d$ and $W\ 5d$, respectively and $d - d$ transition is forbidden, the origin of the both peaks in both DFT-GGA and DFT+U-GGA cases can be attributed to the electron transfer from occupied p stats to empty d or states occupied d stats to empty p states. In DFT-GGA (Figure 4.5b), $O\ 2p$ contributions are observed just below the top of the valence band. Hence, the small peak observed at 0.5 eV in DFT-GGA corresponds to transition from occupied $O\ 2p$ bands to unoccupied $Cu\ 3d$ bands. On the contrary, top of the valence band in DFT+U-GGA (Figure 4.4b) is contributed singnificantly by $O\ 2p$ The smaller peak observed at around $3\ eV$ in DFT+U-GGA corresponds the transition from top of the valence band to the bottom of higher unoccupied conduction band dominated by $W\ 5d$. Another peak is observed at 4.5(4) eV in DFT+U-GGA (DFT-GGA) absorption spectrum is attributed to the electron transfer from occupied $O\ 2p$ states below the top of the valence band to unoccupied conduction $W\ 5d$ states or from the top the valence band to higher unoccupied

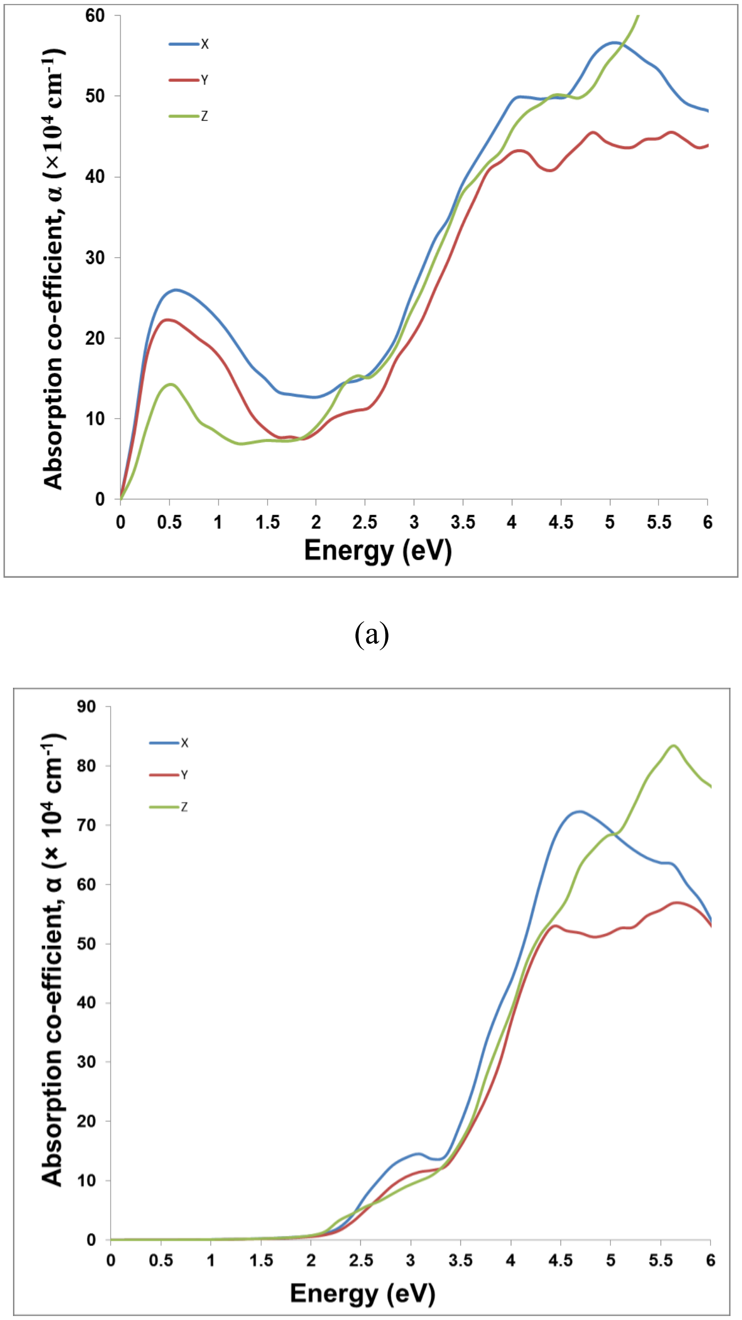

(a)

(b)

Figure 4.6 Optical absorption sepectrum for AFM2-$CuWO_4$: a) DFT-GGA and b) DFT+U-GGA optimizations., respectively.

$O\ 2p$ states in the conduction band This absorption peak observed almost at the same location in both DFT-GGA and DFT+U-GGA cases since neither $O\ 2p$ nor $W\ 5d$ are affected substaintially by U parameter.

Chapter 5

Copper Bismuth Double Tungstate ($CuBiW_2O_8$)

Introduction

Copper Bismuth Double Tungstate or $CuBiW_2O_8$ is the least known and investigated compound in the double-tungstate family. The crystal structure was determined to be triclinic [100]. Moreover, it was claimed that the crystal structure of this material was related to both the triclinic $\beta - CuNdW_2O_8$ and the monoclinic $\beta - LiYbW_2O_8$ and took a middle position between the $CuNdW_2O_8$ and $LiYbW_2O_8$ type. Our DFT+U optimization determines that the crystal structure of this material resembles most with $\beta - LiYbW_2O_8$. The determination of crystal structure using DFT+U-GGA was convincing enough that led us to calculate photocatalytic physical properties such as band gap, density of states, absorption, and cohesive energy with respect to optimized theoretical structure rather than experimental counterpart. It is noted that these physical properties were calculated for the first time which are yet to be measured . In the beging of our work, we are completely unaware of the pre-existence of this material. Our work was started off with a theoretical perspective to predict a suitable photocatalyst and had been evolved through a completely different pathway than experimental approach. We didn't use any experimental precursors to model the unit cells of $CuBiW_2O_8$. Our DFT+U optimized structure was evolved from $CuWO_4$ with Bi addition whereas Cu_2WO_4, WO_3, and Bi_2O_3 precursors were accommodated to synthesize it.

Crystal Structure Modeling

In our present work, the evolution of $CuBiW_2O_8$ crystal structure was done by comprehensive database searching to find suitable motif structures. Motif structures are the well-known structures of those synthesized materials from which the unit cell of new compounds is possible to make. It is done by replacing ion(s) in the motif crystal structure by the equal number of chemically similar ion(s) of the material to predict. The first outcome of our database search was $CuWO_4$. In our case, the first $CuBiW_2O_8$ unit cell was formed by substituting two Cu atoms in AFM-$CuWO_4$ unit cell $(2a, b, c)$ by two Bi atoms, so that we had equal number of Cu and Bi per unit cell, making $CuBiW_2O_8$ an alloy rather than Bi doped $CuWO_4$. The possible different arrangements of Cu and Bi were also taken. The second outcome was AWO_4 structures in ABX_4 $(A = Ca, Cd, Fe, Pb, Y,\ B = W, Mo, Li,\ and\ X = O, F)$ family. We replace $2\,A$ atoms in AWO_4 by one Cu and one Bi, respectively to form $CuBiW_2O_8$. Then, the unit cells were made double, to have all possible arrangements of Cu and Bi. The final outcome was to replace both A and B in ABW_2O_8 by Cu and Bi or only A in $ABiW_2O_8$ by Cu. Each of our unit cells of $CuBiW_2O_8$ contains 24 atoms.

To determine the ground state structure of $CuBiW_2O_8$, we optimize both spin-unrestricted and antiferromagnetic electronic configurations of different possible crystal structures and configurations as mentioned above. The choices were made on several rationales rather than random. Since $CuBiW_2O_8$ is evolved from triclinic $(P\bar{1})$ $CuWO_4$, we, first of all, optimize triclinic $(P\bar{1})$ structure for $CuBiW_2O_8$. We choose three different triclinic $(P\bar{1})$ unit cells differed by only lattice angles. In first case, we keep the optimized atomic coordinates and lattice parameters of ground state $CuWO_4$ intact to form the unit cell of $CuBiW_2O_8$. Hence we name it as pristine-triclinic-$CuBiW_2O_8$. In second case, $CuBiW_2O_8$ unit cell was formed using the same $P\bar{1}$ symmetric atomic coordinates and lattice constants of ground state $CuWO_4$ with $\alpha = \beta = \gamma = 90°$. This structure is longer possesses pure triclinic symmetry and is exposed to orthorhombic modification. Hence, we name it ortho-triclinic-$CuBiW_2O_8$. Like the second one, the third triclinic unit cell differed only in $\alpha, \beta,$ and γ which were chosen arbitrarily. The different sets of (α, β, γ) are

$(80°, 120°, 130°)$, $(130°, 93°, 90°)$, and $(90°, 93°, 130°)$, respectively. The reason to choose three different triclinic unit cells is to optimize $CuWO_4$ with presence of Bi under more degrees of freedom. We could have extended degrees of freedom including arbitrariness of lattice constants, however, restricted ourselves to that of lattice angles only.

Next, we optimize monoclinic wolframite $(P\ 2/c)$, as it is topologically related to that of triclinic $CuWO_4$ [99]. It is well known that compounds in AWO_4 family crystallize in different structures according to the cationic radii and belong to tetragonal scheelite structure $(I4_{1/a})$ for $r_A > 0.90$ Å [110]. As atom A in AWO_4 is replaced by both Cu and Bi, which have cationic radii $r_{Cu^+} = 0.91$ Å, and $r_{Bi^{3+}} = 1.17$ Å, respectively, to form $CuBiW_2O_8$, the scheelite structure was also optimized. Since the cationic radii r_{Cu^+} and $r_{Bi^{3+}}$ are different for the same position 'A', it is likely for $CuBiW_2O_8$ would belong to any of the distorted scheelite structure. Hence, we optimize all possible phase structures from scheelite $(S.G. 12-15, 57, 60)$ [111] [112] [113] [114] [115] as well. Although $S.G. 61-63$ structures are distorted from scheelite, we eliminate those due to the lack of required W coordinations in the structure. We optimize $CuBiW_2O_8$ structures those are derived from ABW_2O_8 family such as $AgBiW_2O_8$, $NaInW_2O_8$, $AgInW_2O_8$, $CuNdW_2O_8$, $\beta-LiYbW_2O_8$, $LiPrW_2O_8$, and $LiHoW_2O_8$ because of similar stoichiometry. The optimization process also encompasses all possible combinations of Cu and Bi in the $CuBiW_2O_8$ unit cells. In addition to mineral database structures' optimization, we optimize a possible structure for $CuBiW_2O_8$ generated by StructurePredictor [14] [116] as well.

Computational Details

$5 \times 9 \times 11$ k-point samplings were used to relax the ions in DFT-GGA and DFT+U-GGA optimizations for $CuBiW_2O_8$. All DOS calculations for DFT-GGA and

DFT+U-GGA were done with maximum possible higher k-points which are $5 \times 9 \times 11$ and $7 \times 13 \times 15$, respectively. The $5 \times 9 \times 9$ k-point sampling was used in optical absorption calculation. This sampling was the maximum efficiency of our available computing facility for optical absorption calculation. The number of empty conduction bands taken for $CuBiW_2O_8$ were 350.

Results

Our DFT+U-GGA calculation optimizes spin-unrestricted ortho-triclinic configuration as the possible ground state structure for $CuBiW_2O_8$. Although theoretical structure have the lowest energy, the energy difference $(\Delta E = 0.002\,\mathrm{eV})$ with the experimental counterpart is so minimal that it could be the possible to have degenerate ground state structures of $CuBiW_2O_8$. Therefore, we proceed our work with respect to our predicted structure and following discussions are based on that. Both DFT-GGA and DFT+U-GGA optimized energies and volumes, respectively for all possible structures of $CuBiW_2O_8$ are shown in Table 5.1. U parameter was applied to only those structures which had energies -94 eV per primitive cell or lower than that in DFT-GGA optimization.

a. Structural properties

DFT+U-GGA calculation optimizes ortho-triclinic structure as possible ground state structure with lattice parameters $= 10.128$ Å, $b = 5.972$ Å, $c = 5.017$ Å, $\alpha = 90.00°$, $\beta = 92.92°$, and $\gamma = 89.99°$. The lattice constants agree well with the experimental counterpart, however, lattice angles differ significantly. Hence, the shapes of unit cells of two structures turn out to be different shown in Figure 5.1. The unit cell of our predicted structure has almost rectangular shape while the unit cell of experimental adopts parallelogram shape. However, the cross-sections of atomic arrangements of both

Table 5.1 Optimized engeries and volumes for diffent motif structures of $CuBiW_2O_8$

	Motif Structures		Energy (DFT-GGA) eV	Volume (DFT-GGA) Å^3	Energy (DFT+U-GGA) eV	Volume (DFT+U-GGA) Å^3
$CuBiW_2O_8$	$CuWO_4$		-94.441	151.07	-92.063	151.56
	AWO_4	Wolframite	-94.437	150.90	-92.059	151.40
		Scheelite	-93.848	152.12		
		Fergusonite	-93.730	151.17		
		Raspite	-94.105	162.21	-91.642	162.56
		Alumotantite	-93.393	147.29		
	ABW_2O_8	$AgBiW_2O_8$	-94.438	150.99	-92.059	151.43
		$NaInW_2O_8$	-94.432	150.80	-92.060	151.48
		$AgInW_2O_8$	-94.433	150.84	-92.060	151.46
		$CuNdW_2O_8$	-94.486	156.80	-91.702	156.44
		$\beta - LiYbW_2O_8$	-94.426	150.64	-92.056	151.32
		$LiPrW_2O_8$	-94.388	154.33	-91.972	154.09
		$LiHoW_2O_8$	-94.428	150.68	-92.055	151.30
	StructurePredictor		-94.126	146.02	-91.699	147.07

structures look similar. Although our predicted structure is derived from orthorhombic modification of triclinic structure, adopts triclinic symmetry. The lattice angles α and γ vary by fraction of a degree, and this fractional difference can be neglected in all practical aspects; the optimized structure then reduces to monoclinic structure. The possible ground state structure for $CuBiW_2O_8$ is shown in Figure 5.2. In Figure 5.2, both Bi and W form BiO_6 and WO_6 octahedra, respectively similar to experimental structure. Unlike Bi and W, each Cu atom form CuO_4 tetrahedra rather than CuO_6 as in $CuWO_4$. Like predicted structure each Cu atom has also four nearest neighbors, however, does not enclose any volume rather it forms a plane (see Figure 5.1) spanned by four Os. This discrepancy can be attributed to the tilt of the unit cell of the experimental structure which forces four Os surrounding each Cu atom to be laid symmetrically on the same plane. All the polyhedra formed by Bi, W, and Cu being connected with each other by corner sharing oxygens form a zigzag layered structure. $Cu-O$ distances, which are on the average ~2.09 Å, almost remain same in different directions contrary to that in $CuWO_4$. Four different $O-Cu-O$ angles are observed in each CuO_4 tetrahedra which are on the average 95.17°, 100.77°, 118°, and 148.8°. Hence, like CuO_6 octahedra in $CuWO_4$, CuO_4 tetrahedra in $CuBiW_2O_8$. The interatomic distances between Cu, W, and O are presented in Table 5.2

Table 5.2 Interatomic distances for DFT+U-GGA optimized $CuBiW_2O_8$

Bonds		Distances (Å)	Bonds		Distances (Å)
$W(1)$	$O(1)$	1.81391	$W(2)$	$O(2)$	1.81386
	$O(5)$	2.09108		$O(5)$	1.97477
	$O(6)$	1.97479		$O(6)$	2.09102
	$O(11)$	1.81000		$O(12)$	1.81014
	$O(15)$	2.21356		$O(15)$	1.87995
	$O(16)$	1.87995		$O(16)$	2.21360
$W(3)$	$O(3)$	1.81020	$W(4)$	$O(4)$	1.81006
	$O(7)$	2.21363		$O(7)$	1.87998
	$O(8)$	1.87994		$O(8)$	2.21360
	$O(9)$	1.81380		$O(10)$	1.81388
	$O(13)$	2.09098		$O(13)$	1.97480
	$O(14)$	1.97478		$O(14)$	2.09111
$Bi(1)$	$O(1)$	2.39061	$Bi(2)$	$O(2)$	2.39080
	$O(4)$	2.31704		$O(3)$	2.31655
	$O(5)$	2.29844		$O(6)$	2.29876
	$O(9)$	2.39076		$O(10)$	2.39045
	$O(12)$	2.31679		$O(11)$	2.31726
	$O(13)$	2.29872		$O(14)$	2.29841
$Cu(1)$	$O(2)$	2.06841	$Cu(2)$	$O(1)$	2.06843
	$O(7)$	2.09160		$O(8)$	2.09167
	$O(10)$	2.06840		$O(9)$	2.06846
	$O(15)$	2.09167		$O(16)$	2.09158

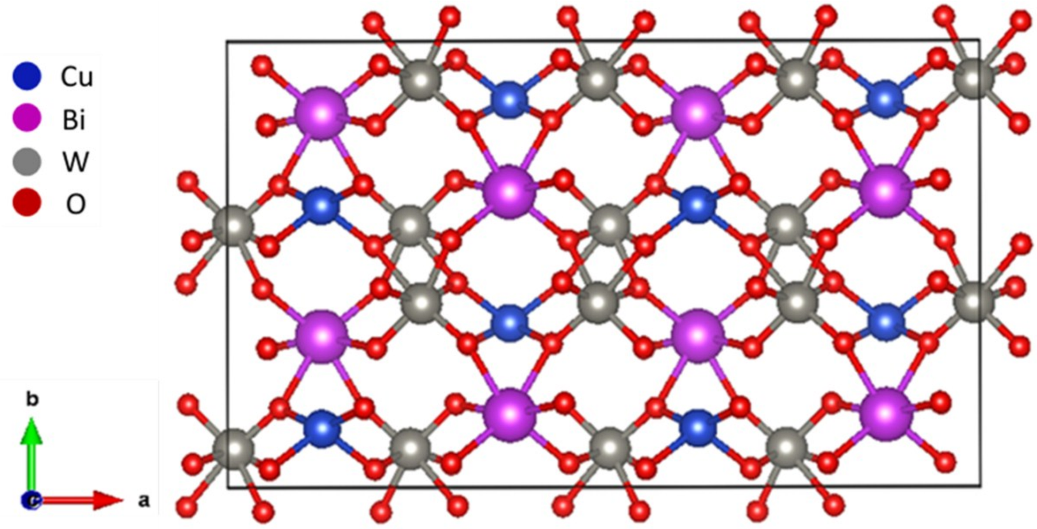

(a)

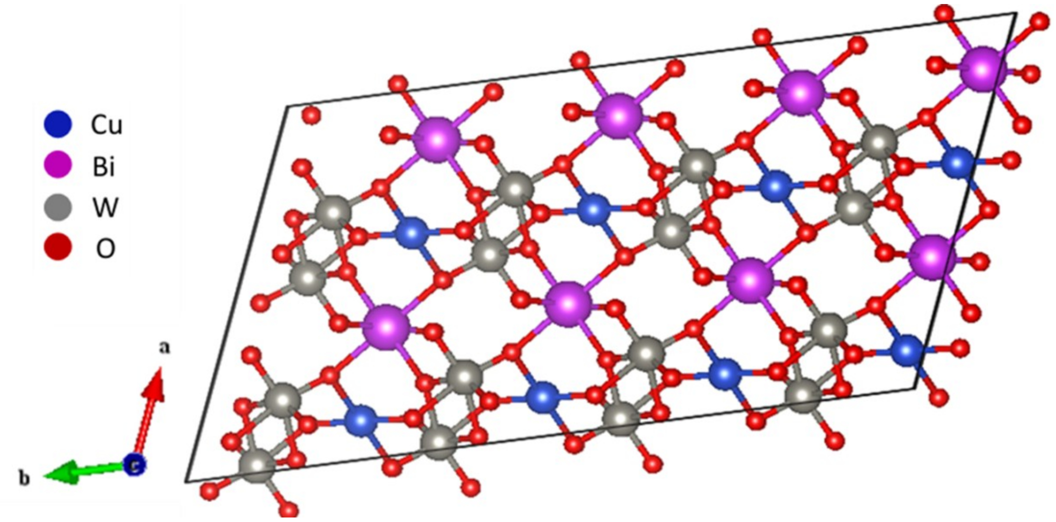

(b)

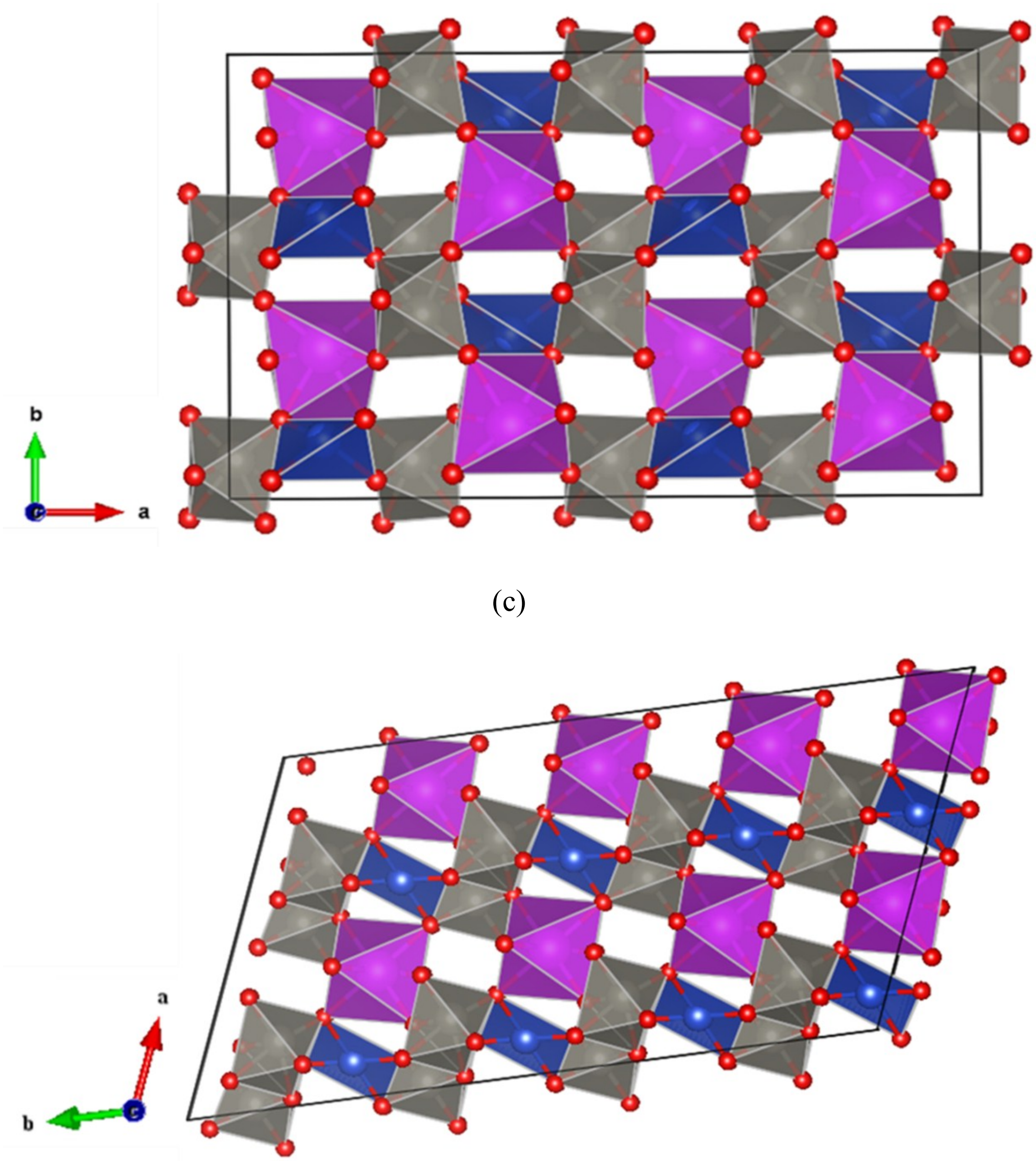

(c)

(d)

Figure 5.1 Crystal structures of $CuBiW_2O_8$ supercell (192 atoms). Figure (a) and (b) show ball-and-stick models for DFT+U-GGA optimized and experimental structures, respectively. Polyhedral models for DFT+U-GGA optimized and experimental structures are shown in Figure (c) and (d), respectively.

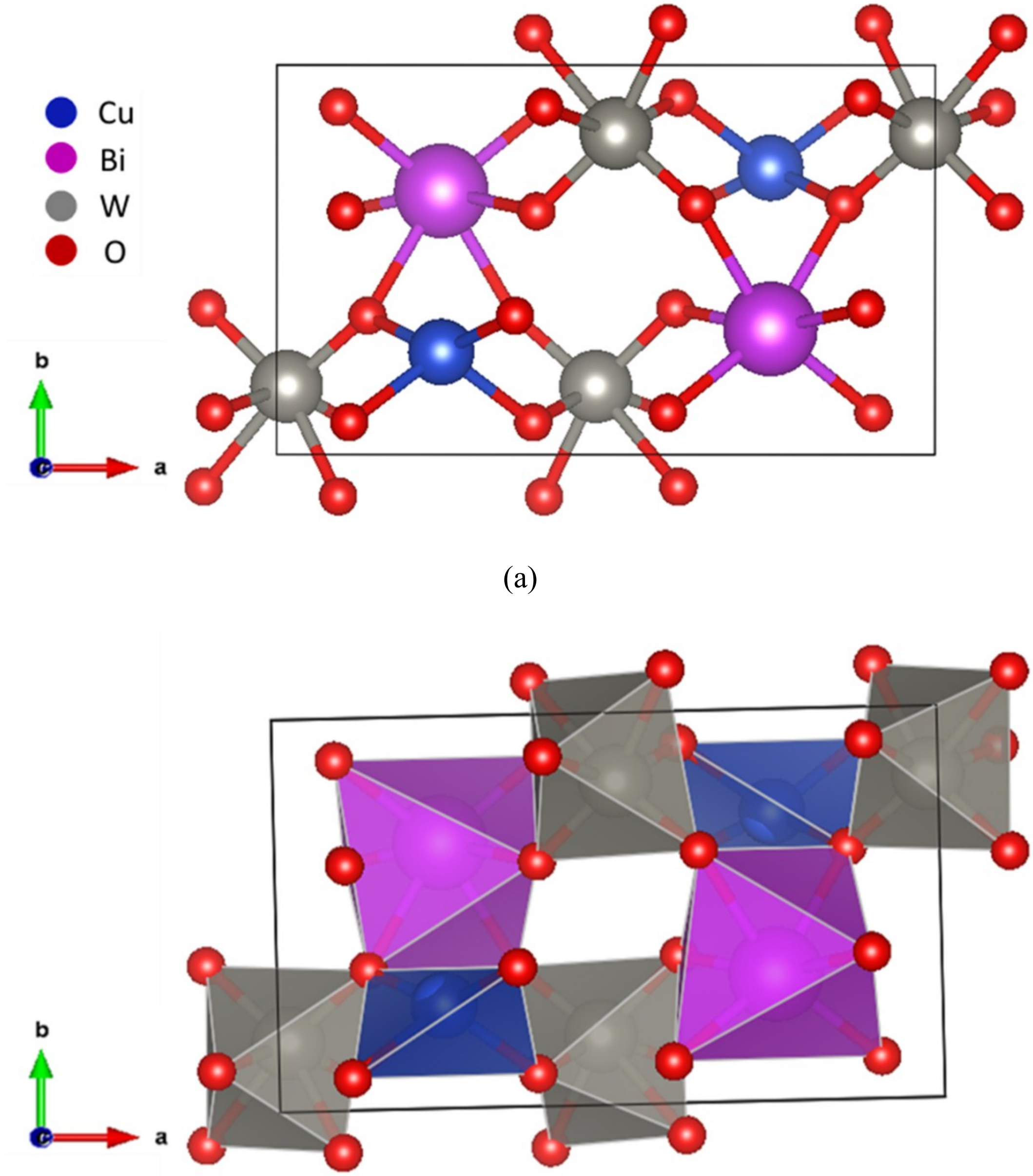

(a)

Figure 5.2 DFT+U-GGA optimized crystal structure of $CuBiW_2O_8$ (24 atoms) is shown in ball-and-stick model (left) and polyhedral model (right).

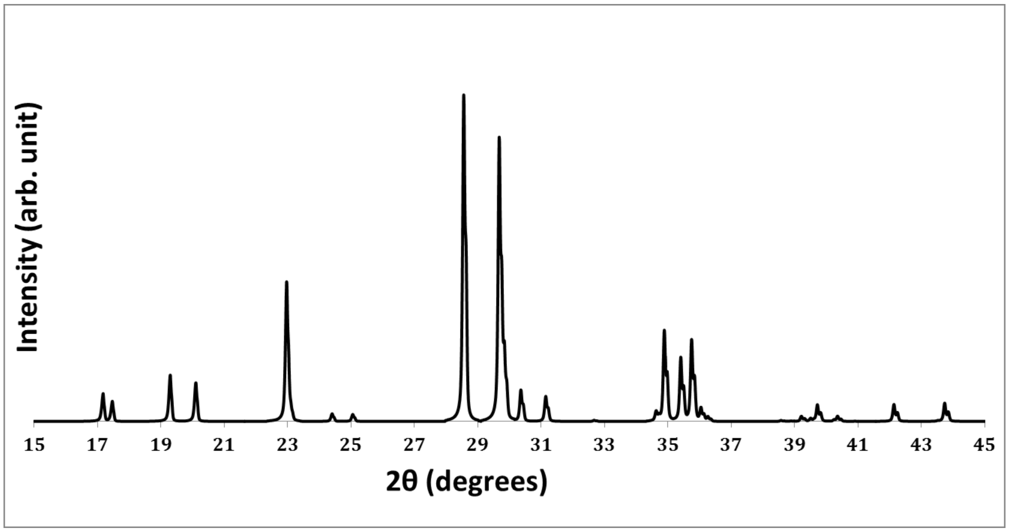

$\Delta E = 0.000$ eV

(a)

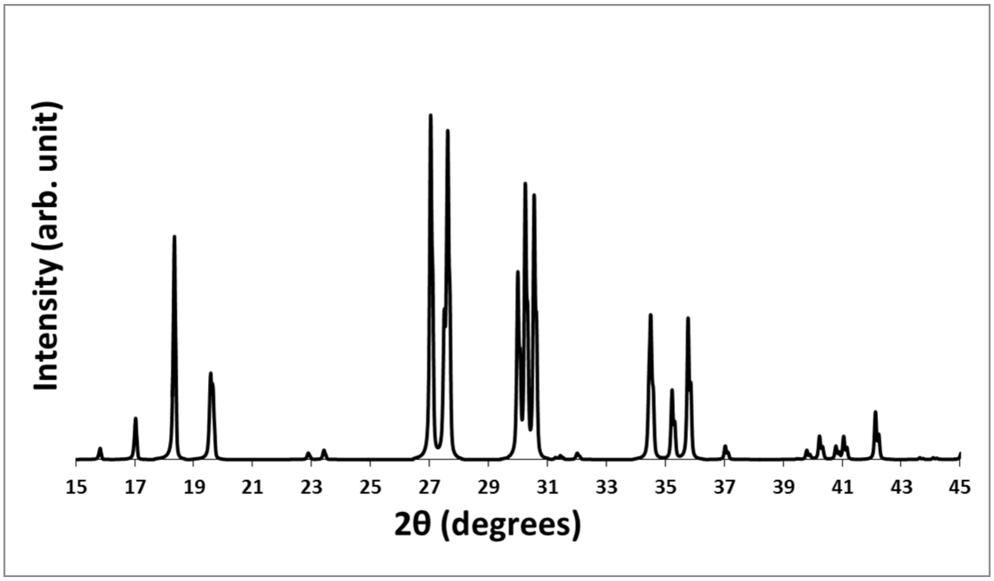

$\Delta E = 0.002$ eV

(b)

Figure 5.3 X-Ray diffraction (XRD) patterns for $CuBiW_2O_8$: DFT+U-GGA optimized structure (a) and experimental structure (b). The total enegry differences are shown bellow the XRD plots of corresponding structures are taken with respect to lowest energy structure.

Figure 5.3 shows X-Ray diffraction (XRD) patterns for both DFT+U-GGA optimized and experimental structures for $CuBiW_2O_8$ The engery differences with respect to lowest energy are shown under the XRD patterns of corresponding structures. Both theoretical and experimental XRDs have many features in common. Like experimental XRD, the large peaks in theoretical XRD are also observed, however, are less in number, seemed two or more peaks being merged with each other form a single peak, and shifted by few angles on the right side. This shifting trend is even higher for the peaks at smaller angles. The peaks between $34°$ to $36°$ are similar to experimental counterpart, and shifting trend is very minimal. All the dissimilarities observed between two structures reftlect differences in the shape of unit cells and CuO_4.

Cohesive energy

The cohesive energy is a measure of cohesion of atoms in solid aggregates manifesting the thermal stability of solids. Hence, the cohesive energy is the solid state analog of the atomization energy or the energy needed to break a solid apart into isolated atoms i.e.,

$$E_{cohesive} = E_{solid} - \sum_{a_i} E_{a_i}^{isolated}$$

where a_i represents the different atoms that constitute the solid. It is well known, all stable arrangements of atoms in solids are such that the potential energy is minimum. The cohesive energy, which corresponds to the attractive part of the potential energy, tells that lower the cohesive energy, more the cohesion of atoms, and higher the thermal stability of the solids.

Our calculated cohesive energy per atom for DFT+U-GGA optimized $CuBiW_2O_8$ was $-2.547\,eV$ which is lower than that of $AgBiW_2O_8$ $(-2.476\,eV)$. This indicates that

$CuBiW_2O_8$ has even higer stability than $AgBiW_2O_8$. The calculated cohesive energies of $\gamma - WO_3$, $Cu\,WO_4$, $AgBiW_2O_8$, and $CuBiW_2O_8$ are shown in Table. 5.3

Table 5.3 Cohesive energies of few different metal oxides.

Compound	Cohesive Energy per atom (eV)	Compound	Cohesive Energy per atom (eV)
$\gamma - WO_3$	-4.367	$AgBiW_2O_8$	-2.476
AFM-$Cu\,WO_4$	-2.721	$CuBiW_2O_8$	-2.547

b. Electronic properties

Figure 5.4 shows the DFT+U-GGA optimized band structure of ortho-triclinic $CuBiW_2O_8$ calculated along the special symmetry points in the Brillouin zone. Several aspects of this band structure are noted. Firstly, the band structure calculation predicts that $CuBiW_2O_8$ has an indirect band gap 1.43 eV between V and R symmetry points. Due to the lack of symmetry about the Brillouin zone center, the Γ-point does not contribute either to the valence band maximum or to the conduction band minimum. The conductions bands along Γ to X are less dispersive indicating higher effective mass of electrons. However, the conduction bands along other symmetry points are dispersive. The valence bands along all symmetry points except along V to R are less dispersive suggesting higher effective mass of holes in these regions. The valence bands around -1 ev contributed mostly by Cu 3d orbitals, which are very localized.

Figure 5.5 represents density of states (DOS) calculations for for DFT+U-GGA optimized $CuBiW_2O_8$. In Figure 5.5b, $Cu\ 3d$ being hybridized with $O\ 2p$ dominates the top of valence band. This hybridization causes an uplift of VB that reduces band gap compared to WO_3. The $Bi\ 6s$, which was found as an anti-bonding contribution at the top of the valence band for $BiVO_4$ [11] does not contribute here at all in the upper region of the valence band. The contributions of $O\ 2p$ and $W\ 5d$ around the band edges are similar to that of the monoclinic WO_3 parent structure. The most contribution at bottom of the conduction band comes from $W\ 5d$. Like $BiVO_4$, $Bi_2W_2O_9$, and $AgBiW_2O_8$ [11] [20] [21] $Bi\ 6p$ lowers the conduction minima through the coupling between $O\ 2p$, $Cu\ 3d$,and $W\ 5d$. Moreover, $Bi\ 6p$ pushes $Cu\ 3d$ mid gap states downward which are found in $CuWO_4$. Those $Cu\ 3d$ mid gap states are hybridized at Fermi level and hence, no longer observed in $CuBiW_2O_8$. Even though the $O\ 2p$ and $Bi\ 6p$ orbital contributions are small around both the band edges, their presence would facilitate favorable $p-d$ optical transitions.

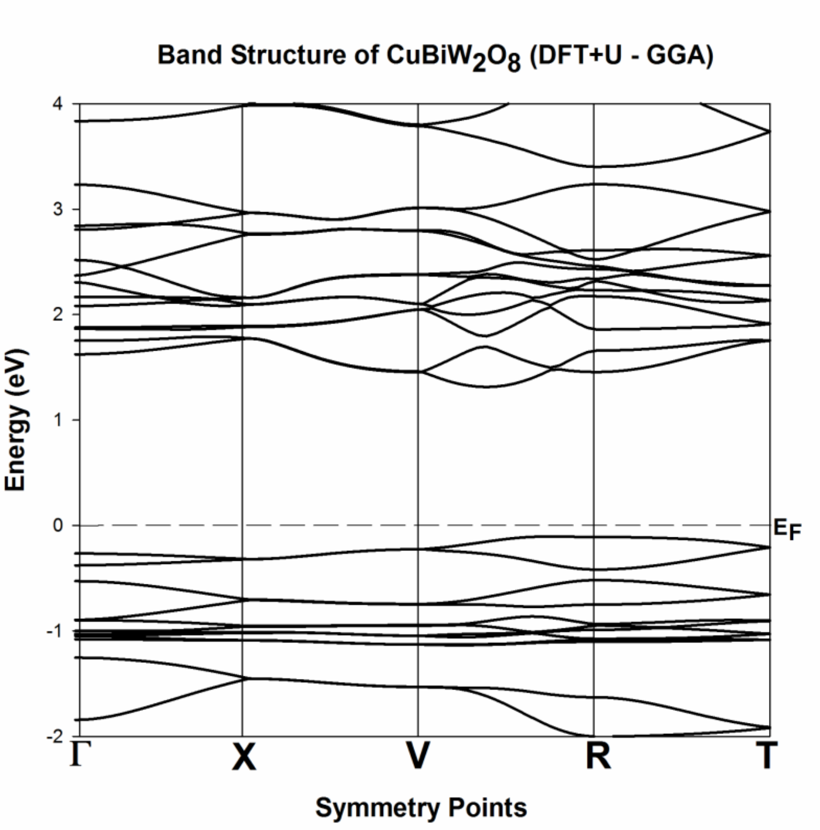

Figure 5.4 Electronic band structure of DFT+U-GGA optimized $CuBiW_2O_8$

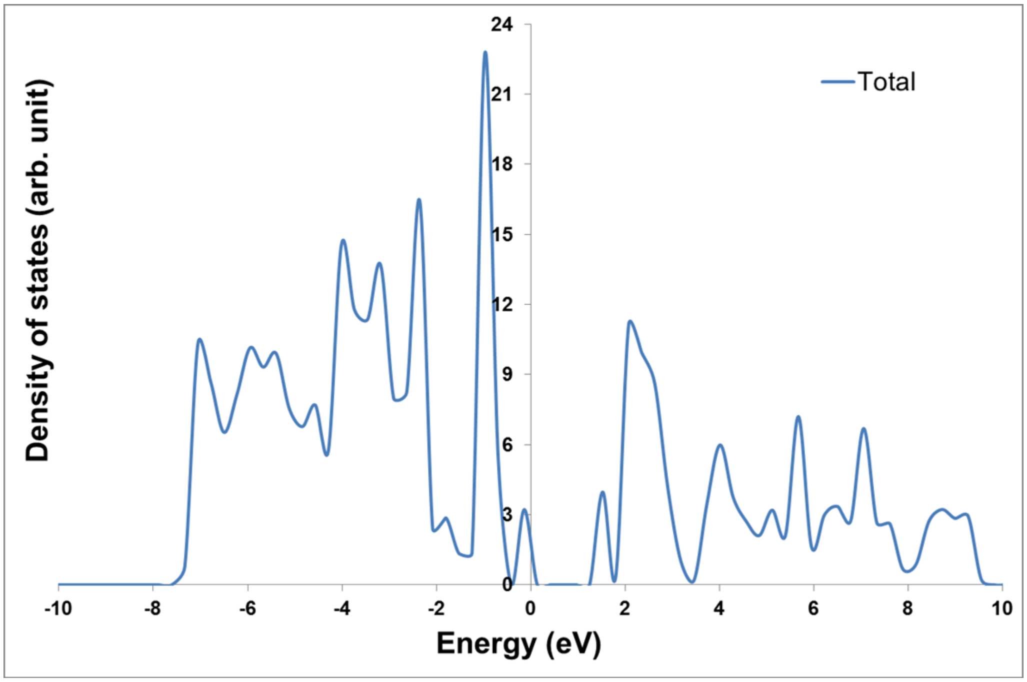

(a)

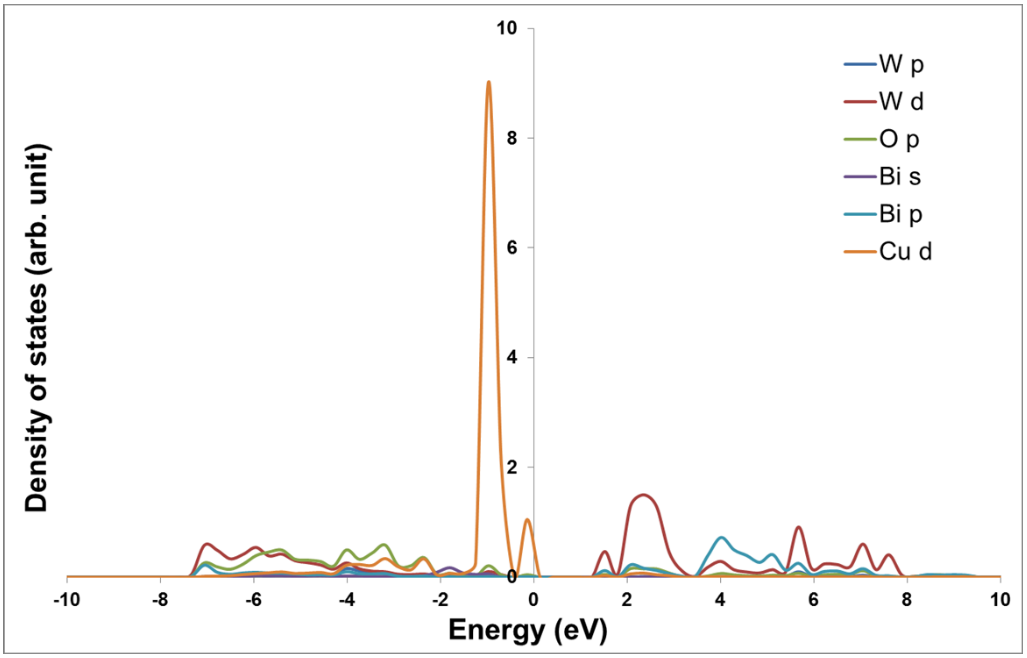

(b)

Figure 5.5 Density of states (DOS) plot for DFT+U-GGA optimized $CuBiW_2O_8$: total (a) and partial (b).

c. Optical absorption

Figure 5.6 represents the optical absorption spectrum for DFT+U-GGA optimized structure for $CuBiW_2O_8$. The absorption is not isotropic. The optical band gap is ~1.5 eV which corresponds to band gap in the electronic band structure calculation. Hence, the contribution to the first peak in absorption curve comes due to the electron transition from the occupied topmost valence band to unoccupied conduction bands. Since $d-d$ transition is forbidden and $Bi\ 6p$ contribution is very small at the top of the valence band, optical absorption can be attributed to the transition of $O\ 2p$ electrons from the top of the valence band to the conduction band. The steep absorption curve indicates that electron transition starts immediately and at a higher rate once electrons absorb energy around 1.5 ev. The long tail of the absorption curve verifies the indirect nature of calculated band gap.

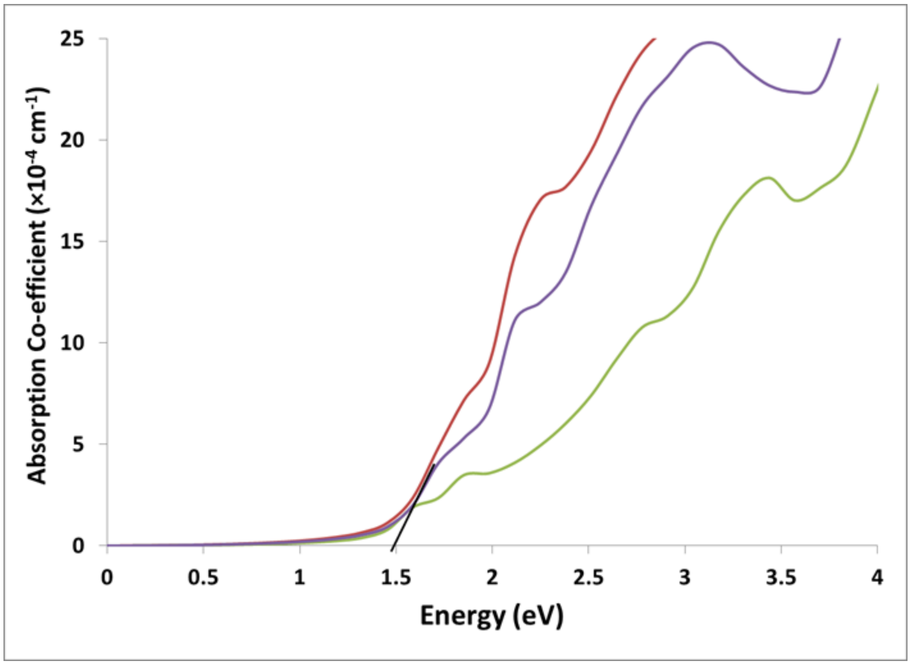

Figure 5.6 Absorption spectrum for DFT+U-GGA optimized $CuBiW_2O_8$.

Chapter 6

Conclusion and Future Directions

Conclusion

In our work, we have been successful to predict a photocatalyst with moderate band gap and improved photocatalytic properties compared to $AgBiW_2O_8$. Although two different precursors in theoretical and experimental procedures, respectively were used to form $CuBiW_2O_8$, had negligible amount of energy difference ($\Delta E = 0.002\ \mathrm{eV}$) which is quite exceptional in the history of predicting the crystal structure of a new material. This result validates and bolsters the credibility, necessity, and methodology of predicting crystal structure using DFT with the help of mineral database search. To our best knowledge, no other crystal structure prediction done through solely the theoretical pathway was so convincing as our work. This negligible amount of energy difference indicates that DFT+U-GGA optimized structure is a strong candidate to be the possible ground state structure of $CuBiW_2O_8$. The structure is found to have triclinic symmetry. In our optimized structure, W was found to form WO_6 octahedra layer like WO_3. On the other hand, Cu was found to form CuO_4 rather than CuO_6 as in $CuwO_4$.

Our calculated band gap was 1.43 eV- a significant amount of band gap reduction compared to $AgBiW_2O_8$ (1.96 eV). The dispersive conduction bands predict higher mobility of electrons, even than $AgBiW_2O_8$. The DOS calculations confirmed the top of VB is dominated by $Cu\ 3d$ like $CuWO_4$ while the bottom of CB is dominated by both $W\ 5d$ and $Bi\ 6p$, similar to $Bi-W$ based oxides. These combined effects reduced the band gap significantly compared to $AgBiW_2O_8$. Hence, our work provides another successful example of band gap reduction forming multications based metal-oxides. Bi addition to $CuWO_4$ removes the $Cu\ 3d$ mid gap states found in $CuWO_4$. Hence, we find absorption is one step process and the curve is very steep similar to $AgBiW_2O_8$. Little contributions from p orbitals around the band edges facilitate this absorption through favoerable $p - d$ optical transition. Hence, it is expected to have similar higher absorption rate like $AgBiW_2O_8$. The cohesive energy of $CuBiW_2O_8$ was found lower than that of $AgBiW_2O_8$ which manifests higher stability of $CuBiW_2O_8$ than that of $AgBiW_2O_8$. We could not verify all our findings because the sole literature available for $CuBiW_2O_8$ encompasses only structural aspect.

The band edge positions with respect to water splitting potentials were not calculated in our work. As $Ag\ 4d$ in $AgBiW_2O_8$ secures suitable band edge positions with respect to redox/oxidation potentials uplifting the conduction band, the similar or even more upward push by $Cu\ 3d$ in $CuBiW_2O_8$ is expected. And this expectation would not be metaphysical at all since $Cu\ 3d$ has higher energy than $Ag\ 4d$.

If our predicted material can be synthesized at low production cost like $AgBiW_2O_8$, 15% or above solar-to-hydrogen conversion efficiency through PEC process will be no longer an elusive goal. If the measured band gap is found higher than 2.2 eV in future, the targeted 15% solar-to-hydrogen conversion the efficiency will be retarded. In that situation, we need to predict another better photocatalyst. This can be done using the similar pathway- addition of multications to binary metal oxides- that has been followed to reduce band gap in $CuBiW_2O_8$. Our successful prediction for $CuBiW_2O_8$ portrays that Cu based double tungstates may be suitable candidates for PEC process if nd orbital based materials are selected to replace B in $CuBW_2O_8$. Moreover, it is necessary to select those elements in periodic table which are not rare on the earth and have low price value on the market while predicting a suitable photocatalyst.

In conclusion, if our prediction becomes successful, commercialization of hydrogen as fuel will be a matter of time. The whole world will be able to reduce CO_2 emission significantly and stop global warming in short period of time. If it is not, our present work still provides a useful information for designing and synthesizing a new material for PEC in the solar-to-hydrogen production technology to be efficient in the near future.

Future Directions

Both GGA and LDA including Hubbard corrections (U parameter) predict the bottom of conduction band is $Cu\,3d$ contributed which is inconsistent with the experimental result. Furthermore, calculated band is very narrow in both GGA and LDA schemes, even with U parameter. However, both higher band gap (2.3 eV) and $W\,5d$ dominated conduction band edge were measured experimentally for AFM $CuWO_4$. The lower band gap problem has been resolved partially using modified Becke-Johnson (mBJ) exchange potential in [109] but $Cu\,3d$ contributed conduction band edge persists. The contradiction between theory and experiment should be resolved. In future, we intend to solve band gap and band edge contribution issue for AFM $CuWO_4$. Furthermore, performance of a photocatalyst highly depends on its band gap. Hence, it is extremely essential to calculate the band gap as accurate as possible. However, underestimation of band gap is a typical feature in standard DFT. Although U parameter employed to highly localized orbitals improves DFT result, does not guarantee the band gap to be consistent with experimental counterpart. Since the electronic description is more accurate while DFT incorporates hybrid functionals, all our future DFT calculations can accomplished using hybrid functionals. In addition, we have allowed only one motif structures of $CuBiW_2O_8$ to have three angular degrees of freedom in the optimization process. To enhance the probability of crystal structure prediction more accurate, more crystalline degrees of freedom (lattice parameters and atomic positions) for all possible motif structures can be incorporated in our future optimizations.

.

Appendix A

Silver Bismuth Dobule Tungstate ($AgBiW_2O_8$)

$AgBiW_2O_8$ belongs to wolframite (S. G. No. 13, Z=2) structure. In this structure, each W atom is coordinated to six O atoms, forming octahedral WO_6 structural units (Figure A.1). Two distinct oxygen atoms (referred to as $O1$ and $O2$) occupy two different sites in this structure: type $O1$ is connected to one tungsten atom with a shorter bond length and to two $'A'$ atoms with larger bond lengths. On the other hand, Type $O2$ is bonded to two different W atoms and to one $'A'$ atom. Thus, the overall structure is made up of hexagonally close-packed oxygens with certain octahedral sites occupied by $'A'$ and W cations. The X-ray diffraction pattern for DFT-GGA optimized $AgBiW_2O_8$ is shown in Figure A.2.

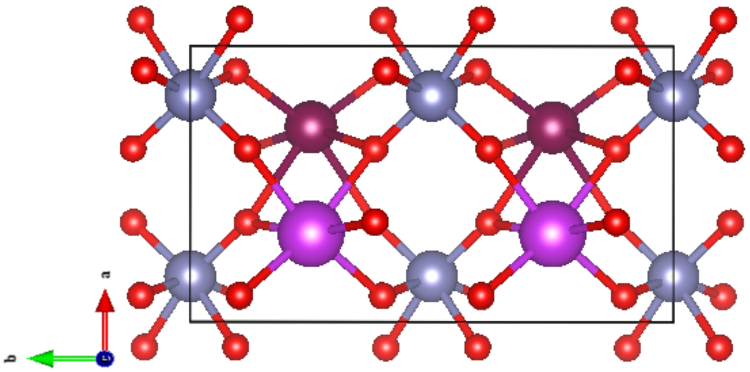

Figure A.1 Crystal Structure of DFT optimized $AgBiW_2O_8$.

Figure A.3 shows the band structure of the wolframite $AgBiW_2O_8$ structure calculated along the special symmetry points in the Brillouin zone. The fundamental band gap of $AgBiW_2O_8$ was found to be an indirect gap of 1.96 eV, where the conduction band minimum occurs between the D and Z points. The minimum direct gap of 2.02 eV occurs in between the Y and E points. Both of these gaps are smaller than the experimentally measured band gaps of~2.75 eV . However, this underestimation of energy band gaps is generally a typical feature of DFT calculations.

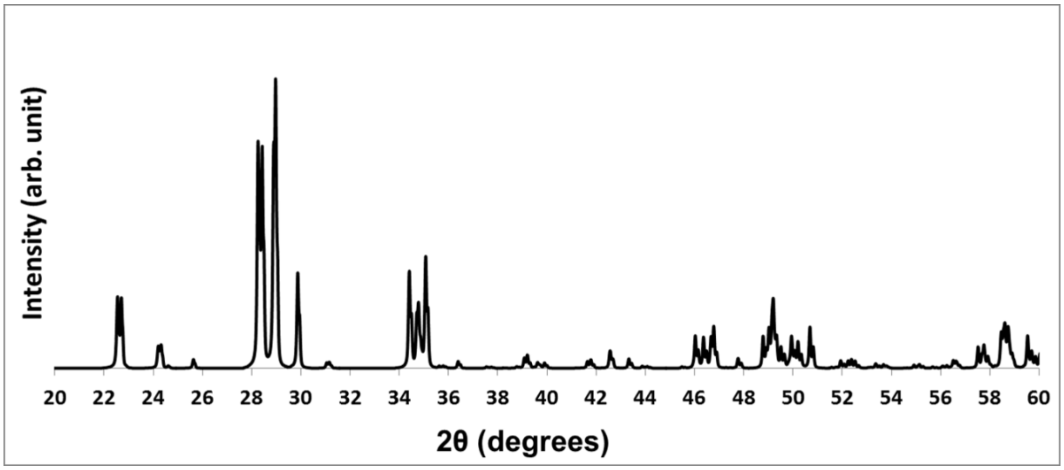

Figure A.2 X-ray diffraction (XRD) pattern for DFT-GGA optimized $AgBiW_2O_8$.

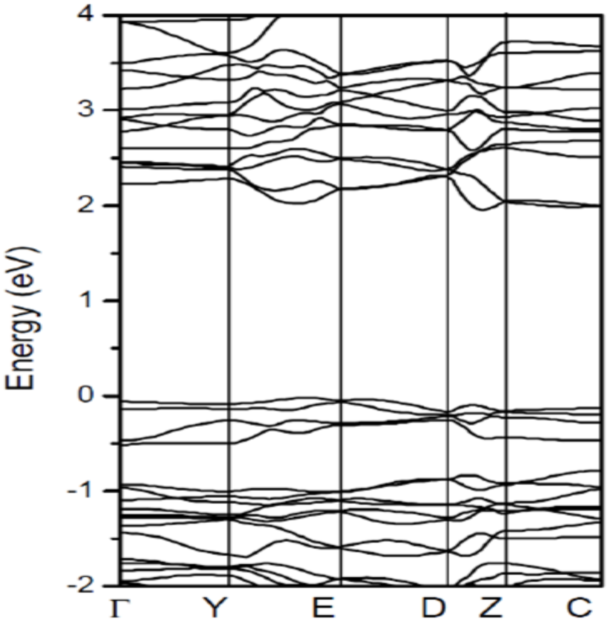

Figure A.3 Electronic band structure of DFT optimized $AgBiW_2O_8$.

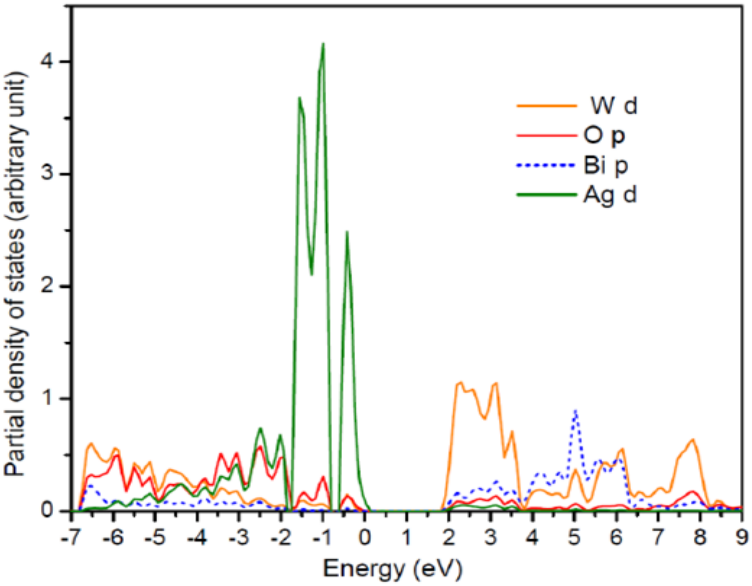

Figure A.4 Partial density of states (p-DOS) plot of DFT optimized $AgBiW_2O_8$.

Figure A.4 shows the partial density-of-states (p-DOS) plot for $AgBiW_2O_8$. From this plot, it is clearly seen that the upper part of the valence band is dominated by contribution from $Ag\ 4d$. In $AgBiW_2O_8$, the valence band is "modulated" by presence of the $Ag - 4d$ level. This is also responsible for the uplift of the valence band edge compared to the WO_3 case. As for the conduction band, $Bi - p$ was found at the conduction band minimum, though the lower part of the conduction band is dominated by $W - d$ levels. Even though the $O\ 2p$ and $Bi\ 6p$ orbital contributions are small around both the band edges, their presence would facilitate favorable $p - d$ optical transitions. The optical absorption spectrum of $AgBiW_2O_8$ is shown in Figure A.5.

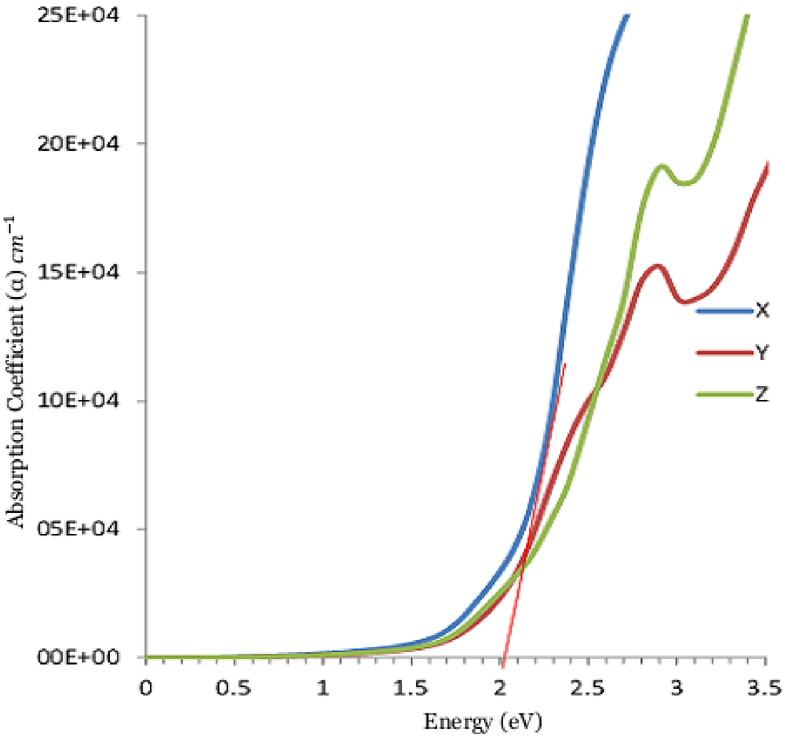

Figure A.5 Absorption spectrum for DFT optimized $AgBiW_2O_8$.

In Figure A.5 the optical band gap is found 2.02 eV which corresponds to the calculated direct electronic band gap. The long tail of the absoption curve verifies that the fundamental band gap is indirect.

Appendix B

Zinc Tungstate ($ZnWO_4$)

Zinc Tungstate ($ZnWO_4$) crystallizes to wolframite structure ($P\ 2/c$).with direct band gap (3.3 eV) [117]. The lattice parameters are: $a = 4.699$ Å, $b = 5.729$ Å, $c = 4.937$ Å, and $\beta = 90.62°$. In $ZnWO_4$, both Zn.and W form ZnO_6 and .WO_6 octahedra, respectively. These octahedra are connected by edge sharing. There are two O atoms that occupy two different sites. The DFT-GGA optimized structures and the corresponding XRD, electronic band structure, partial DOS plot and optical absorption spectrum are shown in B.1, B.2, B.3, B.4, and B.5, respectively.

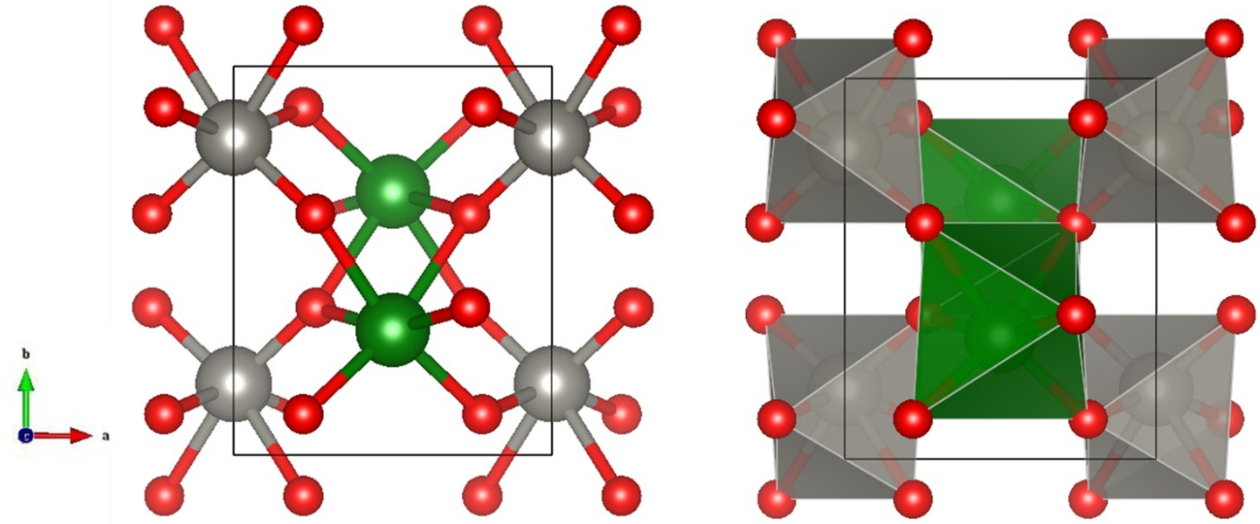

(a) (b)

Figure B.1 Crystal structure of DFT-GGA optimized $ZnWO_4$: (a) ball-and-stick model and (b) polyhedral Model

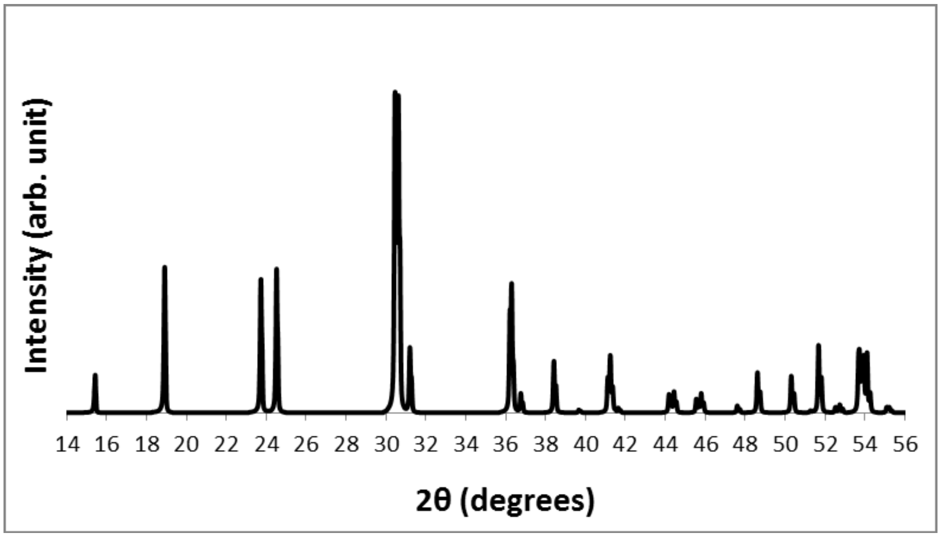

Figure B.2 X-Ray diffraction (XRD) pattern of DFT optimized $ZnWO_4$.

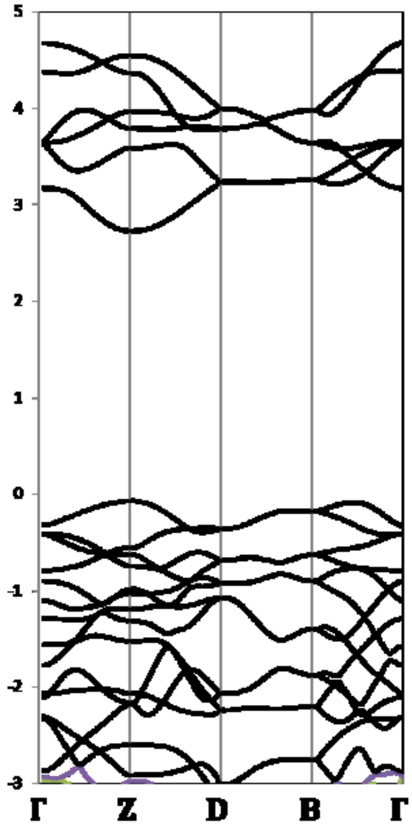

Figure B.3 Electronic band strucutre of DFT optimized $ZnWO_4$.

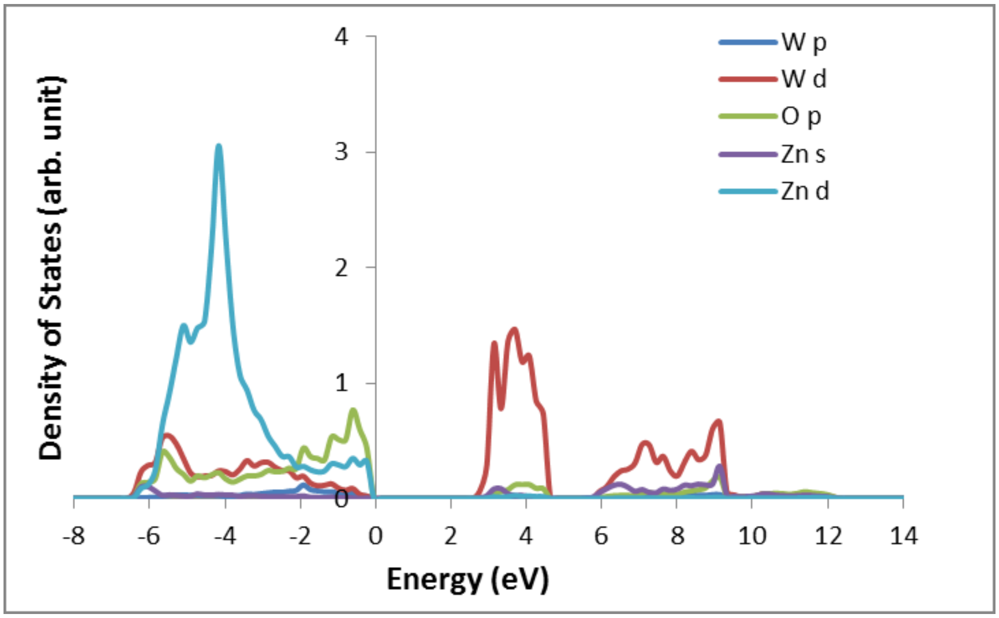

Figure B.4 Partial density of states (p-DOS) of DFT optimized $ZnWO_4$.

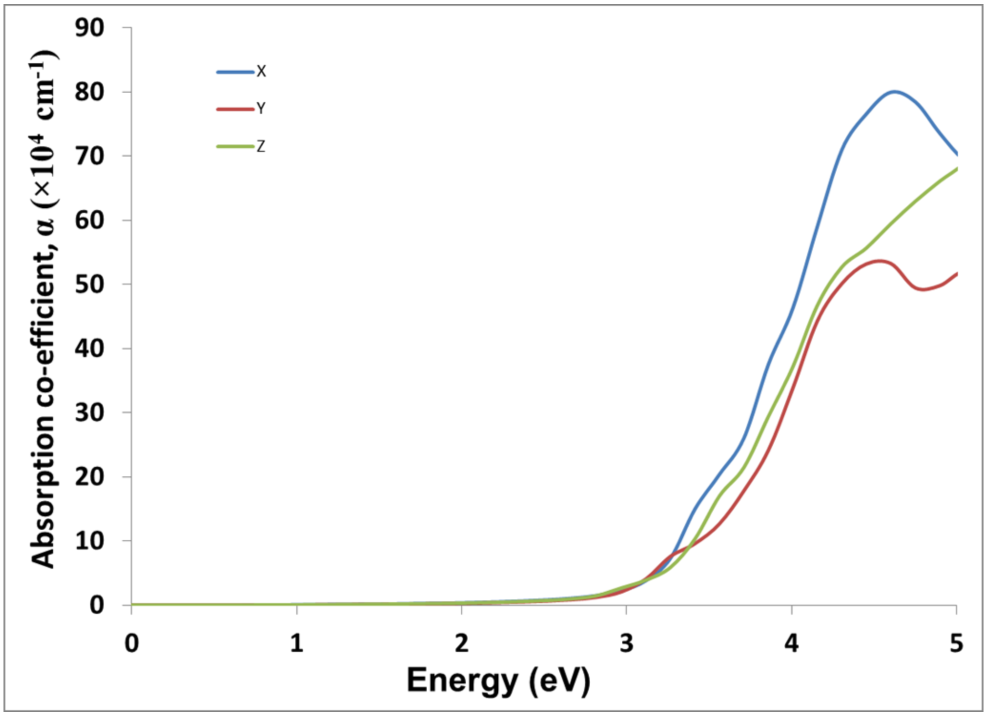

Figure B.5 Absorption spectrum for DFT optimized $ZnWO_4$.

References

[1] K. Rajeshwar, R. McConnell, and S. Licht, *Solar Hydrogen Generation: Toward a Renewable Energy Future*, 1st ed. (Springer, New York, 2008).

[2] Eric L. Miller, in *On Solar Hydrogen and Nanotechnology*, edited by Lionel Vayssieres, 1st ed. (John Wiley & Sons (Asia), Singapore, 2009).

[3] A. Currao, CHIMIA International Journal for Chemistry **61**, 815 (2007).

[4] O. Khaselev and J. A. Turner, Science **280**, 425 (1998).

[5] B. D. Alexander, P. J. Kulesza, I. Rutkowska, R. Solarska, and J. Augustynski, Journal of Materials Chemistry **18**, 2298 (2008).

[6] R. van de Krol, Y. Liang, and J. Schoonman, Journal of Materials Chemistry **18**, 2311 (2008).

[7] M. Woodhouse, G. S. Herman, and B. A. Parkinson, Chemistry of Materials **36**, 4318 (2005).

[8] M. Woodhouse and B. A. Parkinson, Chemistry of Materials **20**, 2495 (2008).

[9] A. Walsh, Y. Yan, M. M. Al-Jassim, and S.-H. Wei, Journal of Physical Chemistry C **112**, 12044 (2008).

[10] F. E. Osterloh, Chemistry of Materials **20**, 35 (2008).

[11] A. Walsh, Y. Yan, M. N. Huda, M. M. Al-Jassim, and S.-H. Wei, Chemistry of Materials **21**, 547 (2009).

[12] U. S. Rochelle M. Cornell, *The Iron Oxides: Structure, Properties, Reactions, Occurrences and Uses*, 1st ed. (WILEY-VCH Verlag GmbH & Co. KGaA, Weinheim, 1996).

[13] G. W. Watson and S. C. Parker, Physical Review B **59**, 8481 (1999).

[14] G. Hautier, C. Fischer, V. Ehrlacher, A. Jain, and G. Ceder, Inorganic Chemistry **50**, 656 (2011).

[15] Y. Zhu, G. Chen, H. Ye, A. Walsh, C. Moon, and S.-H. Wei, Physical Review B **77**, 1 (2008).

[16] J. Da Silva, Y. Yan, and S.-H. Wei, Physical Review Letters **100**, 25 (2008).

[17] K. Sayama, A. Nomura, T. Arai, T. Sugita, R. Abe, M. Yanagida, T. Oi, Y. Iwasaki, Y. Abe, and H. Sugihara, The Journal of Physical Chemistry. B **110**, 11352 (2006).

[18] H. Luo, a. H. Mueller, T. M. McCleskey, a. K. Burrell, E. Bauer, and Q. X. Jia, Journal of Physical Chemistry C **112**, 6099 (2008).

[19] A. Kudo, K. Omori, and H. Kato, Journal of the American Chemical Society **121**, 11459 (1999).

[20] J. Tang and J. Ye, Journal of Materials Chemistry **15**, 4246 (2005).

[21] N. R. de Tacconi, H. K. Timmaji, W. Chanmanee, M. N. Huda, P. Sarker, C. Janáky, and K. Rajeshwar, Chemphyschem : a European Journal of Chemical Physics and Physical Chemistry **76019**, 1 (2012).

[22] A. R. Oganov, editor, *Modern Methos of Crystal Structure Prediction*, 1st ed. (WILEY-VCH Verlag GmbH & Co. KGaA, Weinheim, 2011), p. xi.

[23] H. Katayama-Yoshida, K. Sato, and T. Yamamoto, JSAP International **6**, 20 (2002).

[24] M. S. Dresselhaus, *Solid State Physics (Part II): Optical Properties of Solids* (n.d.), p. 36.

[25] J. P. Perdew, K. A. Jackson, M. R. Pederson, D. J. Singh, and C. Fiolhais, Physical Review B **46**, 6671 (1992).

[26] D. Langreth and M. Mehl, Physical Review B **28**, 1809 (1983).

[27] T. Bak, J. Nowotny, M. Rekas, and C. C. Sorrell, International Journal of Hydrogen Energy **27**, 991 (2002).

[28] W. Kohn and L. J. Sham, Physical Review **140**, A1133 (1965).

[29] F. Wang, C. Di Valentin, G. Pacchioni, and V. R. Cozzi, The Journal of Physical Chemistry C **115**, 8345 (2011).

[30] L. H. Thomas, Mathematical Proceedings of the Cambridge Philosophical Society **23**, 542 (1926).

[31] E. Fermi, Zeitschrift Für Physik A Hadrons and Nuclei **48**, 73 (1928).

[32] http://cmt.dur.ac.uk/sjc/thesis_ppr/node6.html.

[33] R. Jones and O. Gunnarsson, Reviews of Modern Physics **61**, 689 (1989).

[34] G. D. Mahan, *Many-Particle Physics* (Plenum Press, New York and London, 1990).

[35] M. P. Marder, *Condensed Matter Physics* (John Wiley & Sons, 2000), p. 218.

[36] P. Hohenberg, Physical Review **136**, B864 (1964).

[37] E. Engel and R. M. Dreizler, *Density Functional Theory*, 1st ed. (Springer Berlin Heidelberg, Berlin, Heidelberg, 2011), p. 19.

[38] W. Khohn and L. J. Sham, Physical Review **140**, A 1133 (1965).

[39] A. D. Becke, The Journal of Chemical Physics **98**, 5648 (1993).

[40] B. Hammer and M. Scheffler, Physical Review Letters **74**, 3487 (1995).

[41] E. I. Proynov, E. Ruiz, A. Vela, and D. R. Salahub, International Journal of Quantum Chemistry **56**, 61 (1995).

[42] A. C. Scheiner, J. O. N. Baker, and J. A. N. W. Andzelm, Journal of Computational Chemistry **18**, 775 (1996).

[43] D. Hamann, Physical Review Letters **76**, 660 (1996).

[44] V. Ozoliņš and M. Körling, Physical Review B **48**, 18304 (1993).

[45] C. Filippi, D. Singh, and C. Umrigar, Physical Review B **50**, 947 (1994).

[46] P. W. Anderson, Physical Review **124**, 41 (1961).

[47] V. I. Anisimov, J. Zaanen, and O. K. Andersen, Physical Review B **44**, 943 (1991).

[48] V. I. Anisimov, I. Solovyev, M. Korotin, M. Czyzyk, and G. Sawatzky, Physical Review B **48**, 16929 (1993).

[49] A. I. Liechtenstein, V. I. Anisimov, and J. Zaanen, Physical Review B **52**, R5467 (1995).

[50] V. I. Anisimov, F. Aryasetiawan, and A. I. Lichtenstein, Journal of Physics: Condensed Matter **9**, 767 (1997).

[51] V. I. Anisimov, J. Zaanen, and O. K. Andersen, Physical Review B **44**, 943 (1991).

[52] I. V. Solovyev, P. H. Dederichs, and V. I. Anisimov, Physical Review B **50**, 16861 (1994).

[53] S. L. Dudarev, G. A. Botton, S. Y. Savrasov, C. J. Humphreys, and A. P. Sutton, Physical Review B **57**, 1505 (1998).

[54] M. Cococcioni and S. de Gironcoli, Physical Review B **71**, 1 (2005).

[55] J. C. Slater, Physical Review **51**, 846 (1937).

[56] P. M. Marcus, International Journal of Quantum Chemistry **1**, 567 (1967).

[57] P. E. Blöchl, Physical Review B **50**, 17953 (1994).

[58] J. Korringa, Physica **13**, 392 (1947).

[59] W. Kohn and N. Rostoker, Physical Review **94**, 1111 (1953).

[60] D. Hamann, M. Schlüter, and C. Chiang, Physical Review Letters **43**, 1494 (1979).

[61] O. K. Andersen, Solid State Communications **13**, 133 (1973).

[62] H. Skriver, *The LMTO Method: Muffin-Tin Orbitals and Electronic Structure,* (Springer- Verlag, Berlin., 1984).

[63] O. K. Andersen, Physical Review B **12**, 3060 (1975).

[64] G. Kresse and J. Furthmüller, Physical Review B **54**, 11169 (1996).

[65] G. Kresse and J. Furthmüller, Computational Materials Science **6**, 15 (1996).

[66] J. P. Perdew, K. Burke, and M. Ernzerhof, Physical Review Letters **77**, 3865 (1996).

[67] V. I. Anisimov, J. Zaanen, and O. K. Andersen, Physical Review B **44**, (1991).

[68] F. Zhou, C. A. Marianetti, M. Cococcioni, D. Morgan, and G. Ceder, Physical Review B **69**, 201101 (2004).

[69] M. V. Ganduglia-Pirovano, A. Hofmann, and J. Sauer, Surface Science Reports **62**, 219 (2007).

[70] M. Methfessel and A. T. Paxton, Physical Review B **40**, 3616 (1989).

[71] P. Blöchl, O. Jepsen, and O. Andersen, Physical Review. B, Condensed Matter **49**, 16223 (1994).

[72] H. Akkus and A. M. Mamedov, Journal of Physics: Condensed Matter **19**, 116207 (2007).

[73] M. Fox, *Optical Properties of Solids* (Oxford University Press, 2001), p. 6.

[74] S. Cabuk and S. Simsek, Central European Journal of Physics **6**, 730 (2008).

[75] M. Gajdoš, K. Hummer, G. Kresse, J. Furthmüller, and F. Bechstedt, Physical Review B **73**, 1 (2006).

[76] K. Momma and F. Izumi, Journal of Applied Crystallography **41**, 653 (2008).

[77] F. Izumi and K. Momma, Solid State Phenomena **130**, 15 (2007).

[78] Pradyot Patnaik, *Handbook of Inorganic Chemicals* (McGraw-Hill, 2003).

[79] James R. Darwent and Andrew Mills, Journal of the Chemical Society, Faraday Transactions 2 **78**, 359 (1982).

[80] H. Kato, H. Kobayashi, and A. Kudo, The Journal of Physical Chemistry B **106**, 12441 (2002).

[81] G. De Wijs, P. De Boer, R. De Groot, and G. Kresse, Phys. Rev. B **59**, 2684 (1999).

[82] E. Salje and K. Viswanathan, Acta Crystallographica **A31**, 356 (1975).

[83] C. N. R. Rao and B. V. S. Rao, Natl. Stand. Ref. Data Ser. Natl. Bur. Stand., **49**, 117 (1974).

[84] Richard J. D. Tilley, *Crystals and Crystal Structures*, 1st ed. (John Wiley & Sons Ltd, England, The Atrium, Southern Gate, Chichester, 2006), p. 170.

[85] K. R. Locherer, I. P. Swainson, and E. K. H. Salje, Journal of Physics: Condensed Matter **11**, 4143 (1999).

[86] W. L. Kehl, R. G. Hay, and D. Wahl, Journal of Applied Physics **23**, 212 (1952).

[87] A. Aird, M. C. Domeneghetti, F. Mazzi, V. Tazzoli, and E. K. H. Salje, Journal of Physics: Condensed Matter **10**, L569 (1998).

[88] E. Salje, Acta Crystallographica **B 33**, 574 (1977).

[89] S. Tanisaki, Journal of the Physical Society of Japan, **15**, 573 (1960).

[90] B. O. Loopstra and H. M. Rietveld, Acta Crystallographica Section B Structural Crystallography and Crystal Chemistry **25**, 1420 (1969).

[91] P. Woodward, A. Sleight, and T. Vogt, Journal of Physics and Chemistry of … **56**, 1305 (1995).

[92] E. Saljea, Ferroelectrics **12**, 215 (1976).

[93] Y. Xu, S. Carlson, and R. Norrestam, **130**, 123 (1997).

[94] H. J. Monkhorst and J. D. Pack, Physical Review B **13**, 5188 (1976).

[95] M. Huda, Y. Yan, C.-Y. Moon, S.-H. Wei, and M. Al-Jassim, Physical Review B **77**, 1 (2008).

[96] E. Cazzanelli, C. Vinegoni, G. Mariotto, A. Kuzmin, and J. Purans, Solid State Ionics **123**, 67 (1999).

[97] N. L. Heda and B. L. Ahuja, Computational Materials Science **72**, 49 (2013).

[98] P. F. Schofield, K. S. Knight, S. A. T. Redfern, and G. Cressey, Acta Crystallographica **B 53**, 102 (1997).

[99] J. Ruiz-Fuertes, D. Errandonea, a. Segura, F. J. Manjón, Z. Zhu, and C. Y. Tu, High Pressure Research **28**, 565 (2008).

[100] L. Kihlborg and E. Gebert, Acta Crystallographica Section B: Structural … **B 26**, 1020 (1970).

[101] J. E. Yourey and B. M. Bartlett, Journal of Materials Chemistry **21**, 7651 (2011).

[102] L. K. E. Gebert, Acta Chemica Scandinavica **21**, 2575 (1967).

[103] J. B. Forsyth, C. Wilkinson, and A. I. Zvyagin, Journal of Physics: Condensed Matter **3**, 8433 (1991).

[104] H.Weitzel, Solid State Communications **8**, 2071 (1970).

[105] J. Ruiz-Fuertes, D. Errandonea, R. Lacomba-Perales, a. Segura, J. González, F. Rodríguez, F. Manjón, S. Ray, P. Rodríguez-Hernández, a. Muñoz, Z. Zhu, and C. Tu, Physical Review B **81**, 1 (2010).

[106] M. V. Lalić, Z. S. Popović, and F. R. Vukajlović, Computational Materials Science **50**, 1179 (2011).

[107] O. Y. Khyzhun, V. L. Bekenev, and Y. M. Solonin, Journal of Alloys and Compounds **480**, 184 (2009).

[108] A. R. Lacomba-Perales, J. Ruiz-Fuertes, D. Errandonea, D. Martínez-García and Segura, Euro Physics Letter **83**, 37002 (2008).

[109] M. V. Lalić, Z. S. Popović, and F. R. Vukajlović, Computational Materials Science **63**, 163 (2012).

[110] J. Macavei and H. Schulz, Zeitschrift Für Kristallographie **207**, 193 (1993).

[111] J. Lima-de-Faria, *Structural Classification of Minerals: Volume 1: Minerals with A, AmBn, and ApBqCr General Chemical Formulas.* (n.d.), p. 109.

[112] J. R. Smyth and T. C. Mccormick, *Mineral Physics and Crystallography : A Handbook of Physical Constants* (1995).

[113] http://rruff.geo.arizona.edu/AMS/amcsd.php.

[114] F. J. Manjón, D. Errandonea, J. López-Solano, P. Rodríguez-Hernández, S. Radescu, a. Mujica, a. Muñoz, N. Garro, J. Pellicer-Porres, a. Segura, C. Ferrer-Roca, R. S. Kumar, O. Tschauner, and G. Aquilanti, Physica Status Solidi (B) **244**, 295 (2007).

[115] O. Fukunaga and S. Yamaoka, Phys. Chem. Minerals **5**, 167 (1979).

[116] A. Jain, G. Hautier, C. J. Moore, S. Ping Ong, C. C. Fischer, T. Mueller, K. a. Persson, and G. Ceder, Computational Materials Science **50**, 2295 (2011).

[117] C. Janáky, K. Rajeshwar, N. R. de Tacconi, W. Chanmanee, and M. N. Huda, Catalysis Today **199**, 53 (2013).

Biographical Information

Pranab Saker received his bachelor in physics from Department of Physics university of Dhaka, Bangladesh. Then he successfully completed his master's degree in theoretical physics with specialization on condensed matter physics from Department of Theoretical Physics, university of Dhaka, Bangladesh. The title of his master's thesis was "A Theoretical Study of Surface Tension of Crude Oil". After graduation he was involved in teaching physics at undergraduate level.for a short period of time. Then he started his PhD phase in physics department, University of Texas at Arlington (UTA) in the fall of 2010. He continued his passion to work in theoretical condensed matter physics joining the group led by Prof.. Muhammad N. Huda. He passed the PhD qualifying exam successfully in 2011 and intends to persue his PhD program after completion of his master's.